Fabrication of Surface Plasmon Biosensors in CYTOP

By
Hamoudi Asiri

A thesis submitted to the faculty of Graduate and Post-Doctoral Studies in partial fulfilment of the requirements for the degree of Masters of Applied Science in Chemical Engineering.

13/09/2012

Department of Chemical and Biological Engineering
University of Ottawa
Ottawa, Ontario, Canada

ACKNOWLEDGEMNETS

I would like to thank my parents and brother first and foremost for their support and guidance throughout the years and for their patience while I completed my studies. I would also like to thank all the contributors to my research, particularly my thesis supervisors, Dr. Pierre Berini and Dr. Niall Tait, for their direction and for giving me the opportunity to complete the works described herein. Furthermore, I would like to thank the technical support staff at the University of Ottawa, Ewa Lisicka and Michal Tensor, for their assistance and expertise in materials processing and device testing. I would like to thank my predecessors and colleagues, Charles Chiu, Raza Haniff, Norman Fong, Alex Krupin and Asad Khan for their hard work and assistance with my assimilation into the project. Finally I would like to thank the Carleton University Micro-fabrication lab personnel, Rob Vandusen, Rick Adams and Angela Burns for their assistance in fabrication techniques and equipment usage as well as providing me with the necessary training to carry out my research.

ABSTRACT

This thesis describes work carried out on the research, development and implementation of new processes for the fabrication of surface plasmon waveguide biosensors. Fabrication of surface plasmon resonance (SPR) based waveguides embedded in a thick CYTOP cladding with the incorporation of fluidic channels was achieved with improved quality and operability compared to previous attempts. The fabrication flow was modified in key areas including lithography for feature definition, gold evaporation and the upper cladding deposition procedure. The combined result yielded devices with sharper resolution of waveguides, gold surfaces with minimal aberrations, reduced surface roughness and minimization of waveguide deformation due to reduction of solvent diffusion into the lower cladding. The fabricated waveguides consisted of a thin, 35 nm, patterned gold film, embedded in a thick, 18 μm, CYTOP fluoroploymer cladding. The gold devices were exposed by O_2 plasma etching through the upper cladding to form fluidic channels for the facilitation of flow of an index matched sensing medium. Optical and physical characterization of devices revealed structures of significantly improved quality over previous attempts, rendering the platform competitive for biosensing applications.

Table of Contents

Table of Figures

Table of Tables

1. Introduction

1.1. Optical Biosensors

A biosensor is defined as a self contained, integrated device consisting of a biological recognition element (i.e. enzyme or antibody) working in conjunction with a signal transducer, which together may respond in a concentration dependant manner to a chemical species of interest [1], [2]. A number of signal transduction technologies have been adapted for use in biosensing applications including optical, electrochemical and gravimetric techniques. The choice of signal transduction determines cost, instrumentation complexity, physical limitations such as size and portability, sensitivity and data acquisition/signal processing capability [2].

For these reasons, optical biosensors have become an integral tool in the detection and characterization of biochemical interactions. Most phenomena occurring at the sensor surface (adsorption/absorption, fluorescence, luminescence, scattering and refractive index changes) are viable methods for biochemical sensing. As such, optical immunosensors are rapidly replacing traditional immunoassay techniques for clinical and environmental analysis. Furthermore, optical techniques offer the benefit of non-destructive modes of operation as well as the capability of rapid signal generation and detection [3]. Sensors may be classified into two general categories (direct and indirect), the division of which depends on the use of the specific signalling molecules. Direct sensors produce a measurable output due simply to the presence of the target molecule (scattering and

refractive index changes) while indirect, or complex, sensors require a secondary reading of the sensed stimulus (fluorescence, luminescence, adsorption/absorption) [4].

Traditional optical sensors operate on the basis of fluorescent labelling of molecules such as proteins or nucleic acids. This is achieved by covalent bonding of fluorophores to molecules of interest. When fluorophores in their ground state absorb photons, they are raised to an excited state by a shift of electrons to elevated energy levels. As the electrons return to their original energy levels, the excess energy is dissipated in the form of a quantum of light deemed as fluorescence [5].

The indirect approach requires the tagging of target molecules with probes in order for detection to take place; drawbacks of this method include a time consuming labelling process as well as photobleaching (photochemical destruction of the fluorophores) [6]. More recent techniques have enabled direct sensing of targets using a label-free method; this involves the immobilization of analytes on a sensing surface by means of an interaction with target specific receptors interfaced with a signal transduction device. The sensing surface is functionalized such that a specific molecule will bind to it, causing a change in its refractive index which can then be optically measured to indicate the presence of a target analyte.

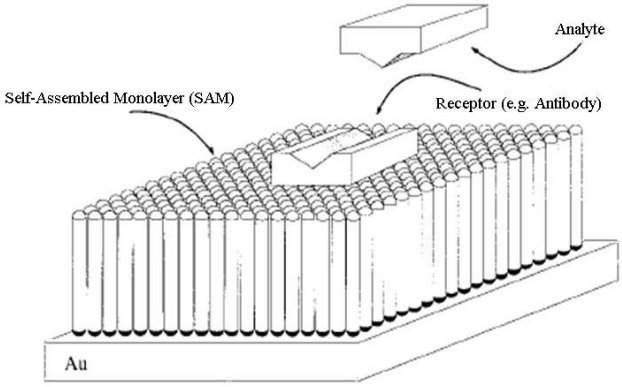

Figure 1: Schematic of functionalized gold structure showing analyte immobilization for optical sensing applications. Adapted from [7].

Figure 1 illustrates a functionalized waveguide surface capable of analyte immobilization. As light travels along the metal surface (as a surface plasmon wave), the power of the guided wave and its concentration dependant response to changes in the sensing medium are measured. In the absence of interference, a shift in power output can be attributed to interactions between the analyte and receptor at the sensor surface. In order for the devices to perform their desired function, the sensing surface must first be coated with a self-assembled monolayer (SAM), this is a compound which will bind to the waveguide surface and act as a facilitator for functionalization with a target specific receptor molecules (e.g. antibodies for protein detection). Gold surfaces are generally regarded as the preferred material of construction for SAM substrates due to 5 main reasons [8]:

- Gold is easily obtained as a thin film by means of physical vapour deposition, sputtering or electro-deposition
- Gold is easily patterned by a combination of lithographic techniques (photolithography, micromachining)

- Gold is relatively inert, it does not oxidize below its melting point and does not react with most chemical compounds
- Thin gold films are commonly used substrates for many spectroscopy techniques such as surface plasmon resonance (SPR), quartz crystal microbalances (QCM), Raman infrared spectroscopy (RAIRS) and ellipsometry.
- Gold is compatible with cells, allowing them to adhere to its surface and function properly without evidence of toxicity.

In addition to the reasons listed above, gold is also the most studied substrate material for the formation of SAM's, followed closely by silver, however, silver tarnishes easily due to reactions with sulfur in air or fluids and also exhibits signs of cell toxicity. Moreover, gold readily binds to SAM's formed from thiols with high affinity, and can maintain stable bonds when exposed to complex media for periods of days or weeks [8]. The SAM is formed from a covalent bond between the gold surface and the thiol group of an alkanethiol according to the following chemical reaction [7]:

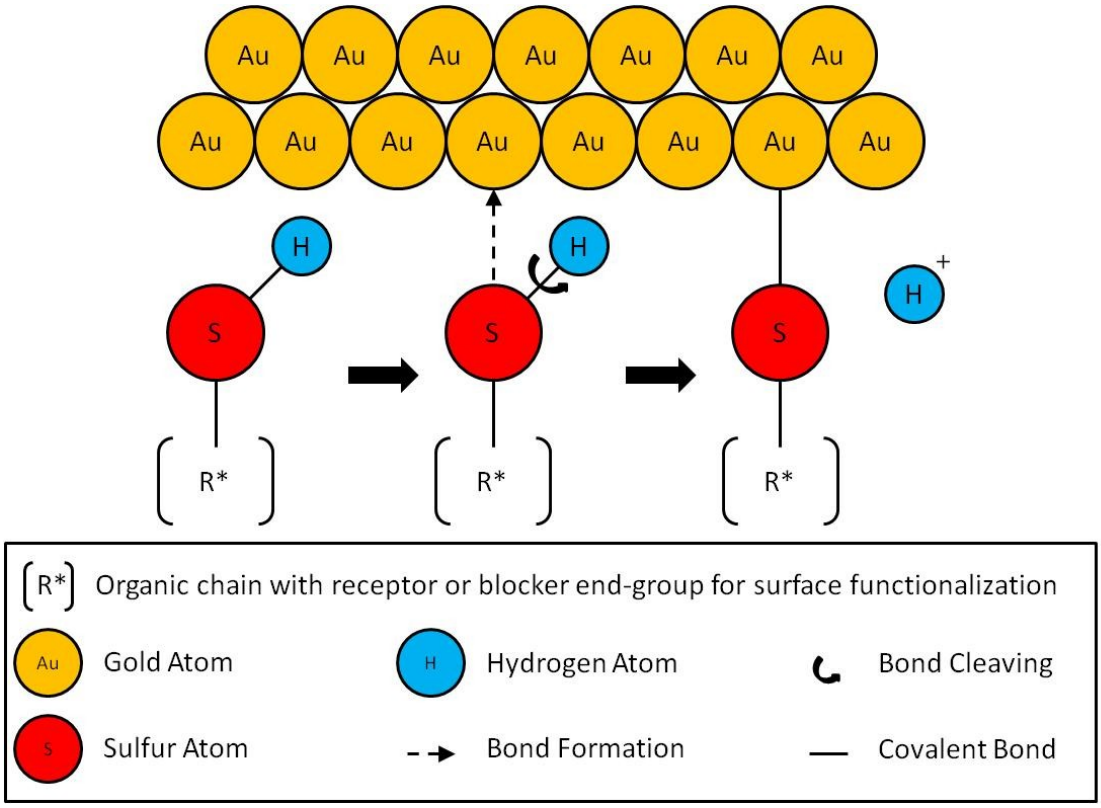

Figure 2: Self assembled mono-layer formation on gold surface through covalent bonding of sulfur end-group.

The specific alkanethiol selected is dependent on the type of receptor (or blocker) the SAM is to be functionalized with. The devices described in the following text use 16-MHA (16-mercaptohexedecanoic acid), having the structure shown in Figure 3, as the SAM forming molecule. This is a carboxyl-terminated SAM, which is well-suited for promoting protein adsorption [7]. It should be noted that the R* group shown in Figure 2 for this specific molecule is $(CH_2)_{15}COOH^+$.

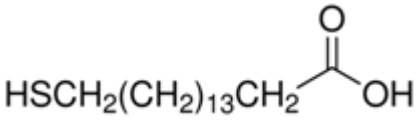

Figure 3: Chemical structure of 16-MHA.

A thin gold film is incubated in a solution containing 16-MHA followed by secondary incubation with a target specific receptor molecule in order to prepare the devices for biosensing application. A detailed discussion of the functionalization procedure can be found in [7] and is described briefly in section 5.4 of this thesis. It should be noted that all biosensing and optical characterization testing discussed in this thesis was performed by other students and technical support staff at the University of Ottawa Optics Laboratory, and that their inclusion is purely illustrative for the purpose of device characterization and verification of operability.

1.2. LRSPP Biosensors

Free electrons within a metal structure, when excited at optical frequencies, can be characterized in a similar manner to that of a gas of free charge carriers (plasma) and are capable of supporting sustained plasma waves [9]. These plasma waves can propagate either within the bulk volume of the metal, referred to as volume plasmons, or bound to a metal-dielectric interface, referred to as surface plasmons. The operating principle of the devices described within this text finds its basis in the exploitation of surface plasmons and their properties.

Surface plasmons are charge-density oscillations existing at the interface of two media with dielectric constants of opposite signs (*i.e., a metal and a dielectric*). The charge density waves are coupled with incident light via a coupling structure (prism, grating) or via

modal overlap in an end-fire arrangement, resulting in the formation of surface plasmon polaritons (SPP's). SPP's are transverse-magnetic polarized optical waves bound to a metal-dielectric interface [10]. The simplest structure which can support SPP's, shown in Figure 4, is a single interface between a metal slab and a semi-infinite dielectric.

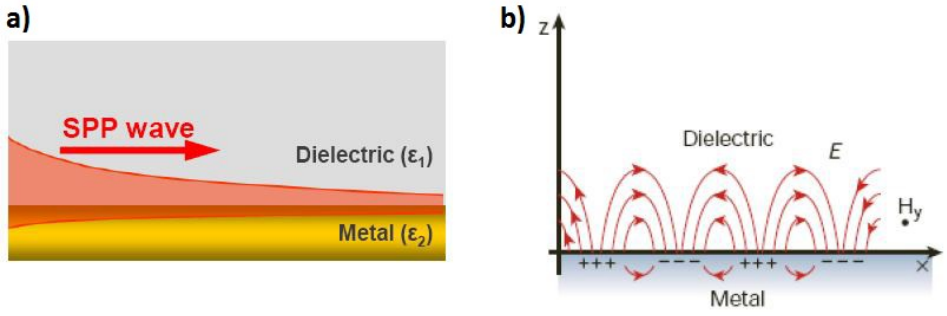

Figure 4: a) attenuation of SPP propagating along metal-dielectric interface, b) surface charge density oscillations and electric field lines. Adapted from [11]

A commonly used arrangement for SPP sensors is the Kretschmann configuration shown below in Figure 5. In this configuration, excitation of surface plasmons is based on total internal reflection of a monochromatic light source. They consist of either an equilateral or right angle quartz prism coated with a noble metal, typically gold, on one of its faces [12]. The metallic surface is functionalized with a target specific receptor and brought into contact with a dielectric fluid. At a given angle, θ, excitation of surface plasmons occurs resulting in a reduction of reflected light intensity. The dependency of the angle θ on the properties of the dielectric medium in contact with the metallic surface has led to significant advancements in instrumentation capable of detecting surface interactions such as protein binding and gas adsorption [13]. Slight changes at the gold-

external medium interface, such as changes in refractive index due to analyte-receptor interactions , lead to a change in the SPR signal allowing for precise measurement of thin film properties and molecular interactions in real time.

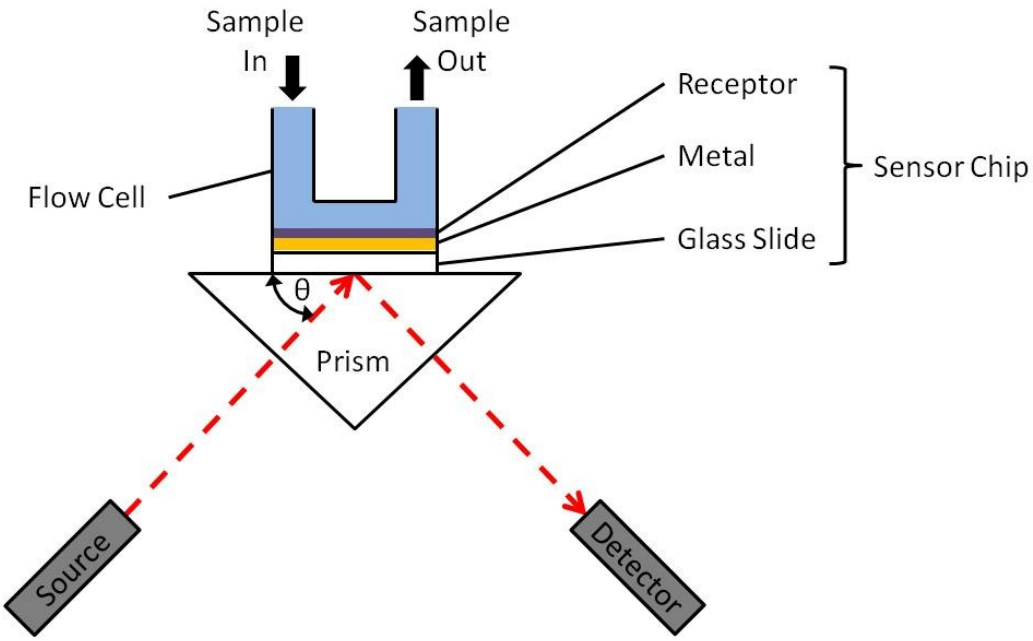

Figure 5: Kretschmann Prism schematic

The structure of particular interest for the devices described in this thesis is the ideal insulator-metal-insulator structure, shown in Figure 6 a). In this mode of operation, a thin metal film of thickness $\boldsymbol{t}$ is bound at both surfaces by a dielectric medium of identical refractive index ($n_1 = n_2$). This results in coupling of two single interface SPP's forming symmetric and asymmetric supermodes. Based on theory ([14], [15]), the symmetric supermode is capable of much longer propagation distances, as much as 1 or 2 orders of

magnitude larger than single interface SPP's, and as such is deemed a long range SPP or LRSPP.

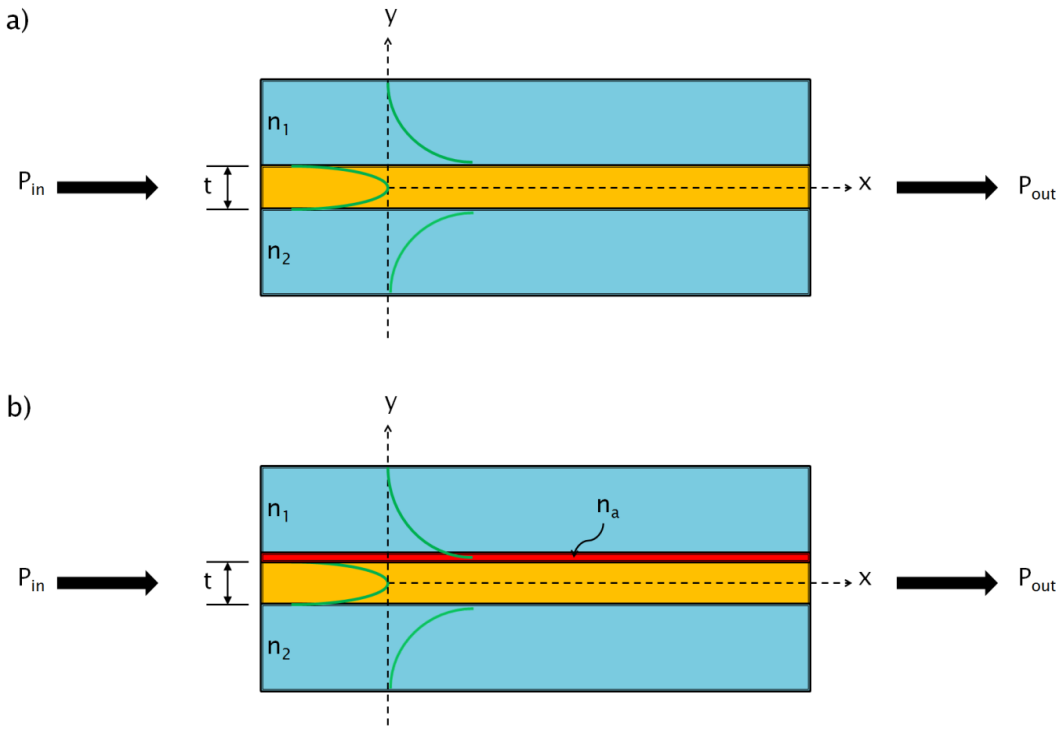

Figure 6: 2D Insulator-Metal-Insulator model showing a) fully cladded waveguide in dielectric medium, b) fully cladded waveguide in dielectric medium with presence of ad-layer of different refractive index.

When a thin ad-layer of different refractive index ($n_a \neq n_1, n_2$) is present on one of the gold surfaces, shown in Figure 6 b), this results in a shift in the propagation distance due to changes in the attenuation constant as well as the wave velocity [6]. The former can be detected in a straight line waveguide by monitoring the output power, and the latter in an optical interferometer such as the Mach-Zehnder Interferometer (MZI) which detects changes in wave velocity as shifts in the phase of the output beam.

Ideally, a structure is desired to have the lowest attenuation value possible since waveguide-based sensor sensitivity is proportional to sensor length [6],[15]. This concept applies to straight waveguides as well as MZI's, shown in Figure 7 a) and b) respectively. The longer the sensing arms of an MZI, the higher the sensor sensitivity. In a scenario free of losses, the sensitivity will increase indefinitely with sensor length for both types of structures [6].

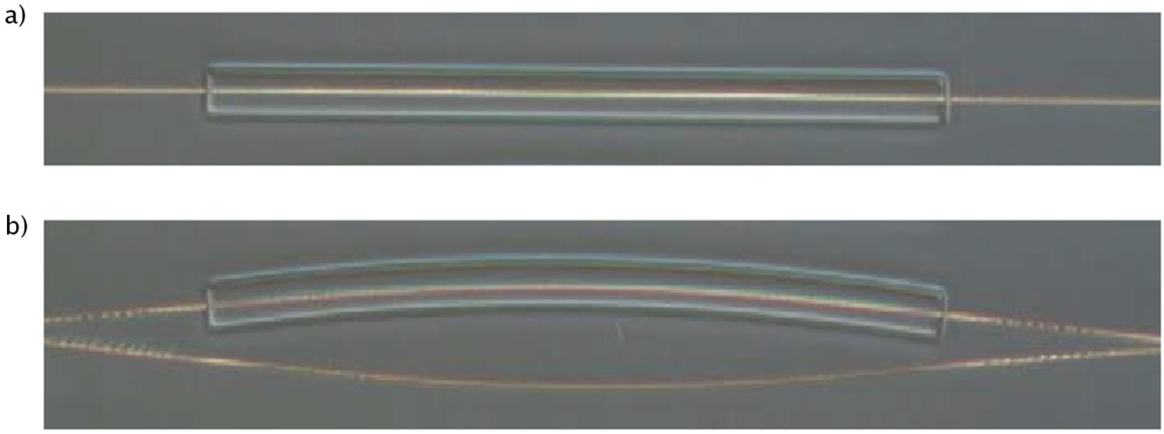

Figure 7: Waveguide based sensor structures with etched fluidic channels: a) Straight waveguide, b) Mach-Zehnder interferometer (MZI). Adapted from [6].

The purpose of the fluidic channels shown in Figure 7 is to be able to expose the gold waveguide surface to a sensing medium. In the case of MZI sensors, one arm is exposed to the sensing medium while the other arm is left fully cladded in the dielectric. The exposed, or sensing, arm is functionalized with target specific receptor molecules such that it is able to immobilize the desired analyte, shown in Figure 8. As the sensor surface

begins to immobilize the analyte, perturbations in the SPP occur, due to the presence of a thin ad-layer on one of the sensor surfaces, Figure 6 b).

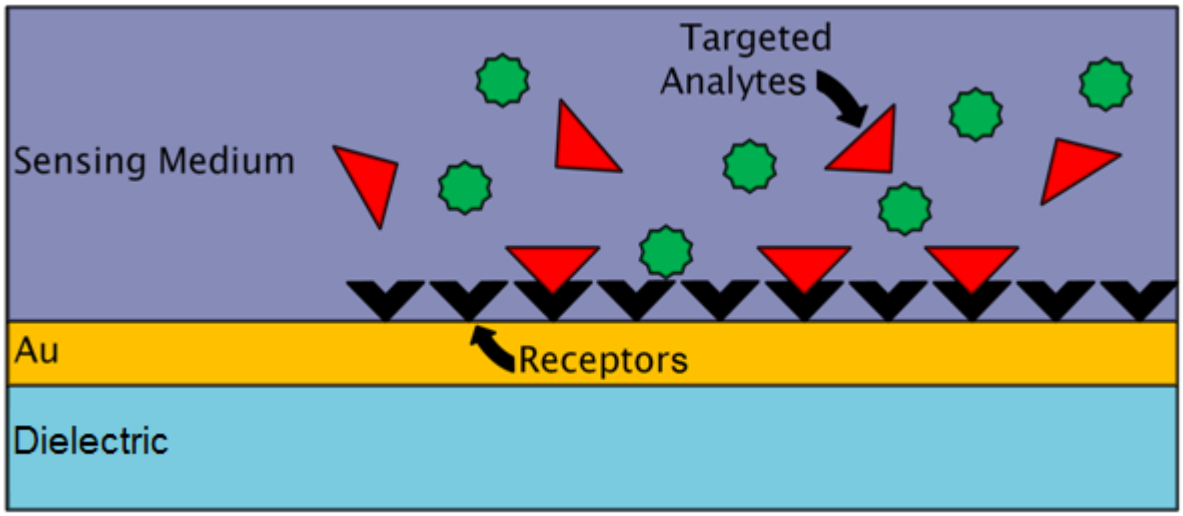

Figure 8: Schematic of analyte immobilization on functionalized waveguide surface.

The degree to which this ad-layer affects the attenuation constant is dependent on its thickness and refractive index. In a straight waveguide, the increase in attenuation is used to verify successful analyte immobilization. The waveguide is excited optically from one end and a detector is used to measure the output at the other (through optical facets), a schematic of the interrogation setup is shown in Figure 9 below. As the surface becomes saturated, the measured output changes from the baseline signal. A plot of the measured output as a function of time, called a binding curve, yields important information about receptor-analyte kinetics due to the ability to observe the sensor signal in real-time.

This ad-layer will also produce a phase shift in the wave, forming the basis of operation in an MZI sensor. The waveguide is excited in an identical fashion to that of a

straight waveguide, the wave travels along the straight portion and its power is split equally amongst each of the MZI arms as the wave leaves the Y-junction. The sensing arm experiences the phase shift due to analyte immobilization, while the cladded, or reference, arm maintains the same phase as the power source. As both waves approach the Y-junction on the opposite end of the structure, they are coupled together and the phase shift in the coupled wave can be detected indicating the presence of an analyte.

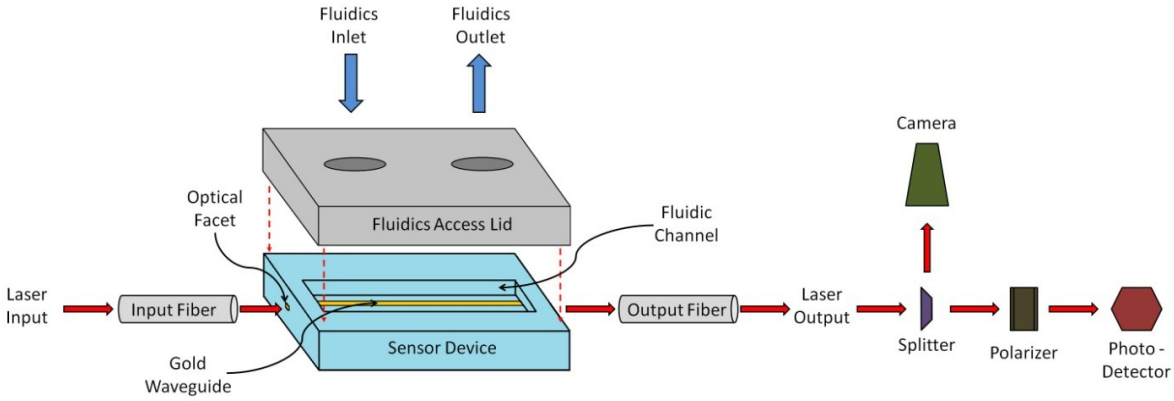

Figure 9: Optical interrogation setup schematic.

1.3. Device Structure & Operation

The procedure outlined in this paper is for the fabrication of long range surface plasmon polariton waveguides with the incorporation of micro-fluidic channels for biosensing applications. The waveguides are thin stripe gold waveguides with dimensions measuring 5 µm in width and 35 nm in thickness. These devices are bound between two thick layers of CYTOP (registered trademark of Asahi Glass Corporation, Tokyo, Japan) with a minimum dimension of 8 µm in thickness, top and bottom. CYTOP is selected as the

dielectric material in these devices for several reasons. It is impervious to water, oil and most chemical substances with exception to a specific fluorocarbon solvent provided by the manufacturer (Asahi Glass Corporation). CYTOP can be easily applied by means of spin coating, dip coating and potting. Furthermore, of most interest is its refractive index. CYTOP has a refractive index slightly above that of water. This allows for the fluidic channels to be filled with dilute aqueous solutions and still allow for the waveguides to maintain a symmetric mode of operation, and for the fluidic channels to disappear optically. The chemical structure of CYTOP is shown below in Figure 10.

Figure 10: Chemical structure of CYTOP [16].

Fluidic channels are etched into the upper CYTOP surface to expose the gold waveguides and to facilitate flow of the sensing medium while a portion of the devices are left fully cladded for device characterization purposes. The channels are 80 µm wide and 8 µm deep with a slight over etch beyond the waveguide level to ensure that the gold waveguides are fully exposed, as illustrated in Figure 11. The wafers are subsequently diced forming waveguides of lengths at 3 mm, 3.8 mm and 4.8 mm. The purpose of dicing the

waveguides at various lengths is to generate a cutback curve (graph illustrating power loss as a function of waveguide length) in order to determine the wave attenuation as it propagates along the waveguide. The graph may also be extrapolated to a device length of zero in order to determine the coupling loss (power loss due to coupling of fiber optic cables to optical facets, shown above in Figure 9, at the waveguide input and output), the value determined from the graph is then divided by two assuming that the losses are equally shared between each end of the device.

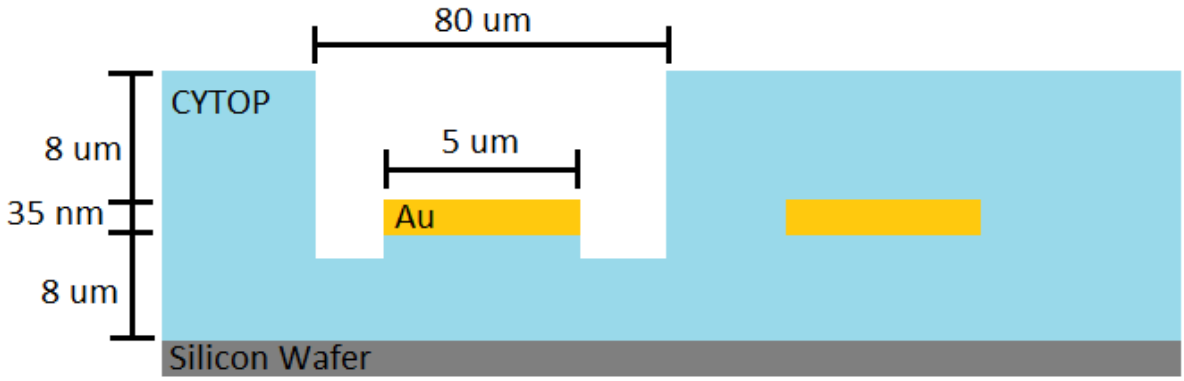

Figure 11: Device structure cross-section showing dimensions of channels and waveguides.

A generalized process flow is outlined in Table 1 describing, in brief, major fabrication levels and device testing for verification of functionality. The first level involves wafer preparation and application of the CYTOP bottom cladding using a spin-coating process, followed by a bi-layer lithography procedure in the second level to define the gold features. In the third level, gold is deposited and a wet solvent stripping process is employed, leaving behind only the patterned gold waveguides on the CYTOP substrate.

Level four is a repetition of level one with modifications to the spin-coating procedure in order to minimize the CYTOP surface roughness and device deformation. The fifth level of fabrication involves definition of the fluidic channels through a lithography process, followed by a reactive ion etch in order to open up the flow channels and expose the gold waveguides in the sixth level. Once the fabrication levels are completed the wafers are diced and sent for optical characterization in level 7. Figure 12 outlines the generalized procedure showing all device components and materials used at all major fabrication steps.

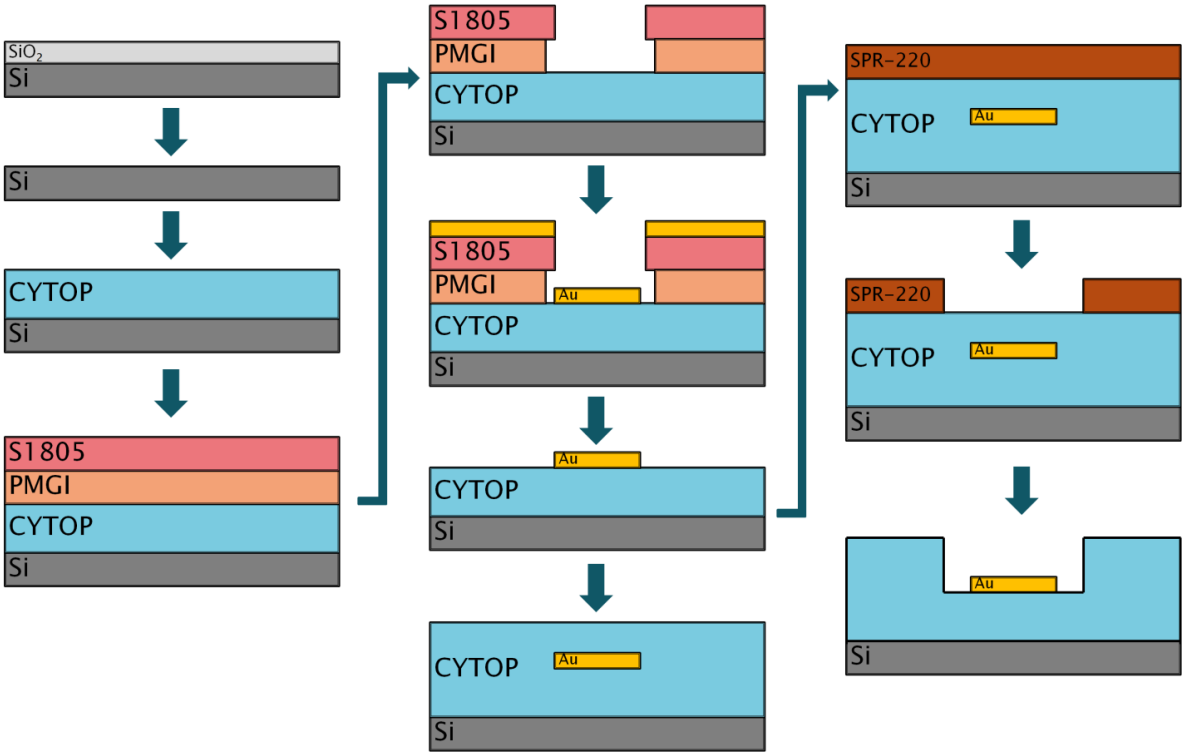

Figure 12: Simplified fabrication flow for LRSPP waveguides in CYTOP with fluidic channels

Table 1: Generalized fabrication procedure. Adapted from [6].

Step	Description	Details
Device Level		
1	Bottom cladding of *CYTOP* on Si substrate wafers	Cladded through the process of spin-coating
2	Lithography of stripe devices	Bi-layer lithography used for proper realization of gold devices
3	Gold deposition and resist strip	E-beam metal deposition and wet solvent strip
Channel Level		
4	Top cladding of *CYTOP* on stripe devices	Embeds devices in *CYTOP* through spin-coating
5	Lithography of microfludic channels on *CYTOP* claddings	Aligned to device level lithography for proper placement of channels
6	Patterned etch of stripe devices	Top *CYTOP* claddings are dry etched with plasma
Device Characterization		
7	Optical characterization	Testing attenuation and insertion losses

1.4. Thesis Structure & Objectives

The primary objective of this thesis is to expand upon the works carried out by ***Chiu et. al. 2009*** [6], in which a fabrication procedure for similar devices was developed. Specifically, the goal is to improve upon the quality of the various device structures, as well as to improve the quality of the gold film of which the waveguides are comprised. The

desired purpose of these devices is to act as a low cost, high sensitivity replacement to conventional immunoassays used for medical and environmental monitoring.

The main issues surrounding the fabrication procedure outlined in [6] are poor definition of the Y-Junctions on the MZI's, over development of the lift-off resist resulting in premature lifting of narrow structures intended to define the waveguides, poor surface quality of the evaporated gold film due to deposition of large spits and finally deformation of the gold features due to solvent ingress into the lower cladding during application of the upper cladding.

It is hypothesized that the aforementioned issues may be resolved by the following process adjustments. Firstly, replacing the current lift-off resist with a polymer which has a reduced dissolution rate when exposed to the same developer solution will aid in improving resolution in the Y-Junctions as well as retarding over development and premature lifting of defining structures. Secondly, by altering the gold deposition procedure to allow for the power to be slowly ramped up to gradually reach the desire deposition rate as opposed to starting the procedure at an elevated power and rapidly reducing the power to reach the desired deposition rate to eliminate "spits" on the gold surface. Finally, reducing the solvent concentration in each layer of the upper cladding before addition of subsequent layers by using higher temperature bakes to anneal the CYTOP, serving to minimize the diffusion rate and thus reduce the level of deformation in the devices.

All process adjustments are monitored qualitatively through visual inspection under an optical microscope and coupled with quantitative measurements such as atomic force

microscopy (AFM) scans and optical intensity measurements to verify both physical and optical characteristics of the devices respectively.

For ease of understanding, this thesis will divide the fabrication of gold stripe waveguides in CYTOP into four main sections:

Chapter 2 - Wafer Preparation and Lower Cladding

- *Describing the surface preparation of the wafer and subsequent spin coating of the CYTOP lower cladding (unaltered from [6])*

Chapter 3 - Lithography and Metallization

- *Describing the procedure for definition and realization of gold stripe waveguides over CYTOP bottom cladding*
- *Outlining changes made in lift-off resist to reduce dissolution rate and changes made to metallization procedure to eliminate "spits" on gold surface*

Chapter 4 - Top Cladding

- *Describing the spin coating procedure of CYTOP for embedding of gold stripe waveguides*
- *Outlining modifications implemented in order to minimize rate of solvent ingress beneath the device layer to reduce deformation of waveguides*

Chapter 5 - Flow Channels

- *Describing the definition and subsequent etching of the flow channels to expose the sensing surface (unaltered from [6])*
- *Examining the physical and optical characteristics of the devices and briefly outlining testing procedures used to verify quality and operability of optical waveguides*

Each chapter will provide a detailed description of the steps necessary for realization of the desired devices followed by a characterization of the features of interest. Furthermore, chapters 3, 4 and 5 will show comparative results of devices fabricated using

a previously developed procedure [6] and outline the improvements achieved in device quality and functionality.

2. Wafer Preparation and Bottom Cladding

2.1. Objectives

The following chapter outlines the procedure for preparation of the wafers prior to beginning the actual fabrication procedure as well as the application process used for constructing the lower CYTOP cladding. The procedures described within this chapter are unchanged from those depicted in ***Chiu et. al. 2009*** and serve mainly for consistency purposes of the fabrication procedure.

2.2. Wafer Cleaning and Preparation

All devices are constructed on 4 inch silicon wafers with a <1,0,0> crystallographic structure. This is verified by inspecting the alignment of the flat edges on the wafer, specifically, by insuring that the large flat edge on the bottom of the wafer is either parallel to a short flat edge on the top of the wafer, Figure 13 a), or perpendicular to a short flat edge on the left side of the wafer, Figure 13 b).

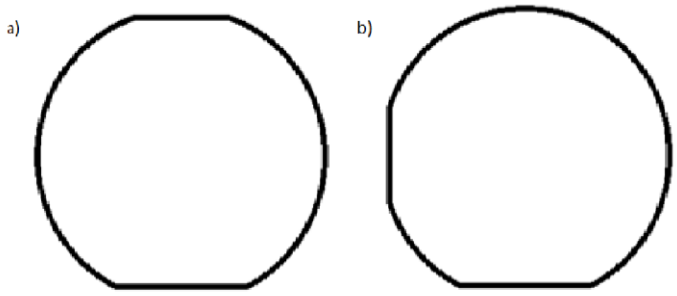

Figure 13: Flat alignment for wafer crystallographic orientation verification, a) showing parallel secondary flat, b) showing perpendicular secondary flat.

The wafers are prepared by first immersing them in 10 wt% aqueous hydrofluoric acid for 20 seconds in order to remove any SiO_2 from the surface. Afterwards they are rinsed in demineralised/deionised water and dried under a high purity nitrogen jet. The wafers are then etched in O_2 plasma to dehydrate the surface and remove any surface contaminants that may have survived the HF dip. The plasma etch conditions are given in Table 2 shown below.

Table 2: Wafer preparation O_2 plasma etch specifications

Machine make and model	Plasmatic Systems - Plasma-preen II 862
Power (W)	750
Oxygen flow rate (sccm)	300
Operating pressure (Torrg)	5
Exposure Time (min)	5

After the cleaning and dehydration in O_2 plasma, the wafer is again exposed to a high purity nitrogen jet to ensure that no dust particles are present on the polished surface.

2.3. Lower Cladding Fabrication

Once the wafer surface is clean and dry, the bottom cladding process may be applied (the lower cladding fabrication process described in [6] is adequate and was applied in this thesis without modification). This begins with a thin layer of M-grade CYTOP (CTL-809M) diluted down to 5 wt% solids using CT SOLV 180 as the diluent. M-grade CYTOP

incorporates a silanated end-group adhesion promoter to facilitate bonding to a silicon substrate, shown in Figure 14 below.

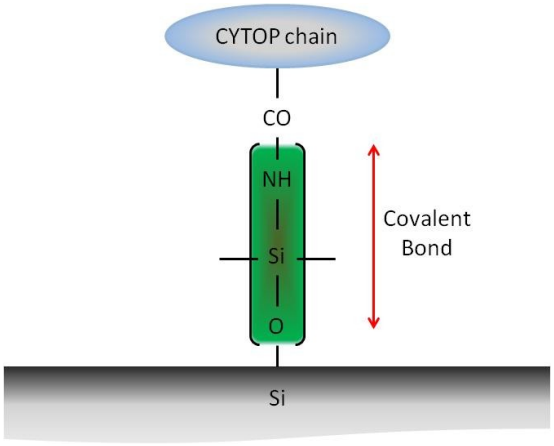

Figure 14: Schematic of silanated end-group of M-grade CYTOP for adhesion promotion to silicon substrates [16].

This layer is spin coated, initially at 500 rpm for 10 seconds to ensure proper coverage of the wafer, then 1000 rpm for an additional 20 seconds to achieve the desired thickness of approximately 400 nm [6]. After spinning, the wafer is "soft baked" on a direct contact hot plate at 50 °C for 30 minutes. This removes the majority of the solvent from the CYTOP layer allowing for easier handling during subsequent processing steps.

Once the initial M-grade adhesion layer is applied, the bulk of the bottom cladding is spun on using S-grade CYTOP (CTX-809SP2) at 9 wt% solids. S-grade CYTOP is spun at 1000 rpm for 10 seconds to ensure full wafer coverage then ramped up to 1500 rpm for an additional 20 seconds to achieve the desired layer thickness of 2.35 µm [6]. The wafer is then subjected to another 30 minute "soft bake" at 50 °C to partially anneal the film. The spinning and baking process is repeated two more times in order to obtain a total cladding

thickness of S-grade CYTOP of approximately 7 µm, this insures that the initial M-grade CYTOP layer and the polished silicon wafer surface are outside of the optical tail of the propagating waves. The need for multiple layers is to ensure that each layer is spun on smoothly and with little to no surface defects, this is difficult if spinning at low velocities and thus requires multiple coatings.

The final bottom cladding layer is applied using S-grade CYTOP diluted down to 5 wt% solids using CT SOLV 180 as the diluent. This is done to ensure that the CYTOP-metal interface maintains the desired optical properties of S-grade CYTOP while also minimizing surface variation in the bottom cladding due to the reduced viscosity of diluted CYTOP. The layer is spun at 1000 rpm for 20 seconds giving a film thickness of approximately 0.76 µm [6]. After spinning, the wafer is then placed on a direct contact hot plate at 50 °C for 30 minutes. Once the final layer is "soft baked", the hot plate is then ramped up from 50 °C to 200 °C at a rate of 150 °C/hr then maintained at 200 °C for an additional 2.5 hours. This fully anneals the CYTOP bottom cladding as well as helps planarization of the upper surface. The full bottom cladding process is illustrated in Figure 15 and described in Table 3.

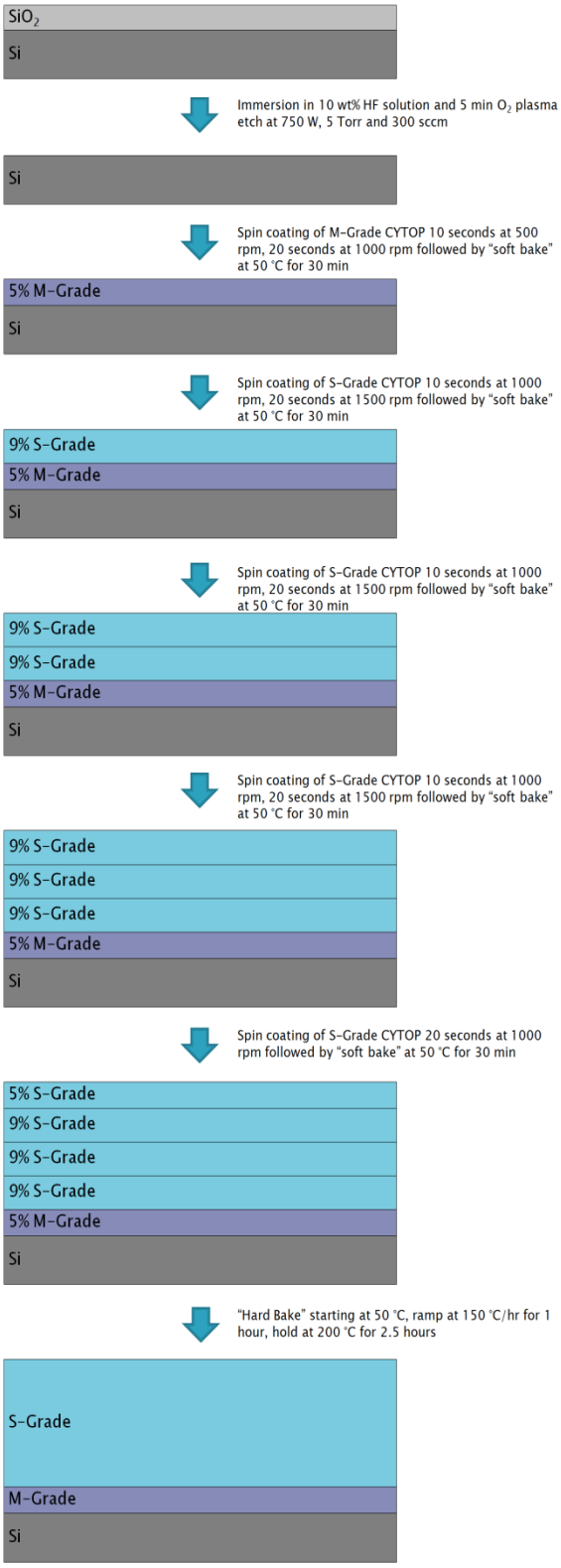

Figure 15: Wafer priming and bottom cladding fabrication process flow diagram

Table 3: Wafer priming and bottom cladding fabrication procedure

Processing Step	Description
HF Dip	Wafer dipped into 10 wt% HF to remove native SIO_2 layer from wafer surface
Plasma Preen Wafer Priming	Wafer dehydration and cleaning in microwave induced O_2 plasma
5 wt% solids CTL-809M spin coating	Spread-spin at 500 rpm for 10 seconds followed by planarizing-spin at 1000 rpm for 20 seconds (0.4 µm)
Soft bake	30 minute bake direct contact hot plate at 50°C
9 wt% solids CTX-809SP2 spin coating	Spread-spin at 1000 rpm for 10 seconds followed by planarizing-spin at 1500 rpm for 20 seconds (2.35 µm)
Soft Bake	30 minute bake direct contact hot plate at 50°C
9 wt% solids CTX-809SP2 spin coating	Spread-spin at 1000 rpm for 10 seconds followed by planarizing-spin at 1500 rpm for 20 seconds (2.35 µm)
Soft Bake	30 minute bake direct contact hot plate at 50°C
9 wt% solids CTX-809SP2 spin coating	Spread-spin at 1000 rpm for 10 seconds followed by planarizing-spin at 1500 rpm for 20 seconds (2.35 µm)
Soft Bake	30 minute bake direct contact hot plate at 50°C
5 wt% solids CTX-809SP2 spin coating	Planarizing-spin at 1000 rpm for 20 seconds (1.4 µm)
Soft Bake	30 minute bake direct contact hot plate at 50 °C
Hard Bake	Ramp from 50 °C to 200 °C at 150 °C/hr then hold for additional 2.5 hours at 200 °C (3.5 hr total)

In the aforementioned procedure, the most important control variables are the spin speeds and CYTOP concentrations. This will ensure that the deposited film is of sufficient thickness which is vital for proper operation of the waveguides [14]. Furthermore, the CYTOP concentration will determine the degree of planarization of the upper surface, since this is the supporting structure of the waveguides it is important to have a smooth, flat surface in order to minimize any deformation which may occur in the metal structure.

2.4. Surface Characterization

The surface roughness of the bottom cladding was verified using atomic force microscopy (AFM) [6]. A 3 μm × 3 μm patch is analyzed in order to check for root-mean-square (rms) and average surface roughness, shown in Figure 16. The CYTOP surface was shown to have a rms roughness of 0.81 nm and an average surface roughness of 0.6 nm. According to simulation studies performed in [14], a maximum surface roughness of 1 nm is required in order for proper functionality of waveguides.

Another important aspect to be measured is the refractive index of the bottom cladding. CYTOP is selected as the dielectric material in these devices due to the proximity of its refractive index to water. Since many biosensing applications are performed using dilute aqueous solutions, this property makes CYTOP an ideal choice. S-grade CYTOP is reported to have a refractive index of 1.3395 when tested at a wavelength of 633 nm [16]. Water tested at the same wavelength yields a refractive index of 1.3330. Measurements performed in [6] yielded an average refractive index of 1.3385 ± 0.0001 for the lower

cladding, since the lower cladding fabrication procedure used in the devices described in this thesis is identical to that used in [6], it is assumed that an average value of 1.3385 is an accurate representation of the refractive index of CYTOP.

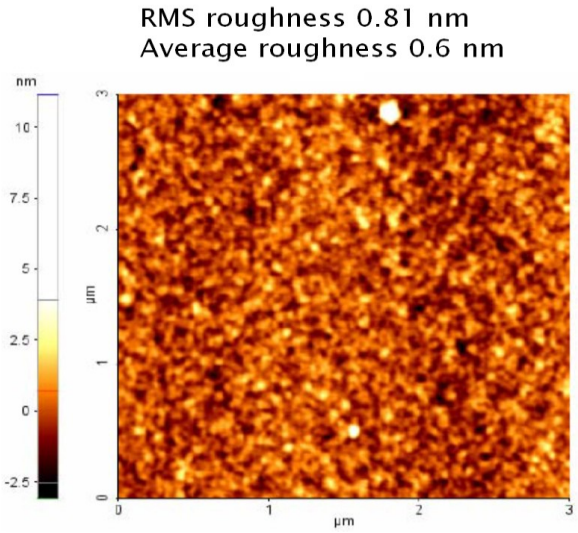

Figure 16: AFM surface amplitude scan for roughness verification. Adapted from [6]

3. Lithography and Metallization

3.1. Objectives

This chapter outlines the fabrication processes involved in definition and realization of the gold waveguides. Modifications were proposed to the original process outlined in ***Chiu et. al. 2009*** including substitution of the lift-off resist in order to reduce the dissolution rate to improve Y-Junction resolution and eliminate over-development of defining structures in double and triple output MZI's as well as reduction of the gold deposition rate in order to eliminate spits on the gold surface.

3.2. Materials and Method

Surface Priming

After the bottom cladding is fully annealed, the CYTOP surface must be primed in order to facilitate the application of the lift-off resist and the photoresist for waveguide definition. Since CYTOP is highly repellent to water and oil, it must be treated to allow spin coating of polar compounds such as solvents contained in PMGI (cyclopentanone and tetrahydrofurfuryl alcohol) [17].

The CYTOP surface is initially primed with O_2 plasma to “ash” the surface and allow for coating of hexamethyldisilazane (HMDS) which is spun at 1000 rpm for 10 seconds then baked on a direct contact hot plate at 105 °C for 1 minute. “Ashing” is performed in a March Systems Jupiter II bench-top etcher, this helps improve the surface wettability

allowing for the application of PMGI lift-off resist. The surface priming procedure is outlined in Table 4 below.

Table 4: CYTOP surface priming procedure for photolithography processing

Processing Step	Description
Ashing	O_2 plasma etch at 100 W, 300 mTorr and 220 sccm for 30 seconds
HMDS Spinning	Spin coating of HMDS (1000 rpm for 10 seconds)
Soft Bake	Bake on direct contact hot plate for 1 minute at 105 °C

Bi-Layer Lithography

After baking, the surface is cleaned off with high purity nitrogen then PMGI SF 2G is spun on, initially at 500 rpm to ensure total wafer coverage, followed by 1000 rpm to achieve the desired thickness of approximately 75 nm [17]. The wafer is then baked on a direct contact hot plate for 3 minutes at 180 °C to dry the solvent. Following the PMGI lift-off resist, S1805 positive tone photoresist is spun on, initially at 1000 rpm for 10 seconds, then at 4000 rpm for an additional 30 seconds to bring the film down to a desired thickness of approximately 600 nm. The wafer is then baked on a direct contact hot plate at 115 °C for 3 minutes. The bi-layer lithography procedure is shown Table 5 below and in the process drawing shown in Figure 17.

This is a revision to a previously developed procedure outlined in [6], in which a similar approach is taken towards the spin coating of the photoresist with the exception of a

substitution in the lift-off resist. The previous process called for Microchem's LOR-1A lift-off resist, spun initially at 1000 rpm for 10 seconds, then at 4000 rpm for an additional 30 seconds. The spin coating procedure is followed by baking on a direct contact hot plate at 180 °C for 3 minutes to fully cure the resist layer.

The decision to use PMGI SF 2G was primarily based on its relatively low dissolution rate in MF 321 developer solution. This allows for good control of the undercut and yields cleaner lift-off, giving better overall device definition. A detailed description of the improvements achieved through the use of PMGI SF 2G as the lift-off resist is given in section 3.3.

Table 5: Lift-off resist and photoresist application procedure

Processing Step	Description
Nitrogen clean	Wafer is sprayed with high purity nitrogen stream to partially dry surface as well as removing dust and other particulates.
PMGI SF 2G Spinning	PMGI lift-off resist is spun at 500 rpm for 10 seconds followed by 1000 rpm for 30 seconds (~ 75 nm)
Soft Bake	PMGI is baked at 180 °C for 3 minutes
S1805 Spinning	S1805 positive photoresist is spun on at 1000 rpm for 10 seconds followed by 4000 rpm for 30 seconds (600 nm)
Soft Bake	S1805 is baked at 115 °C for 3 minutes

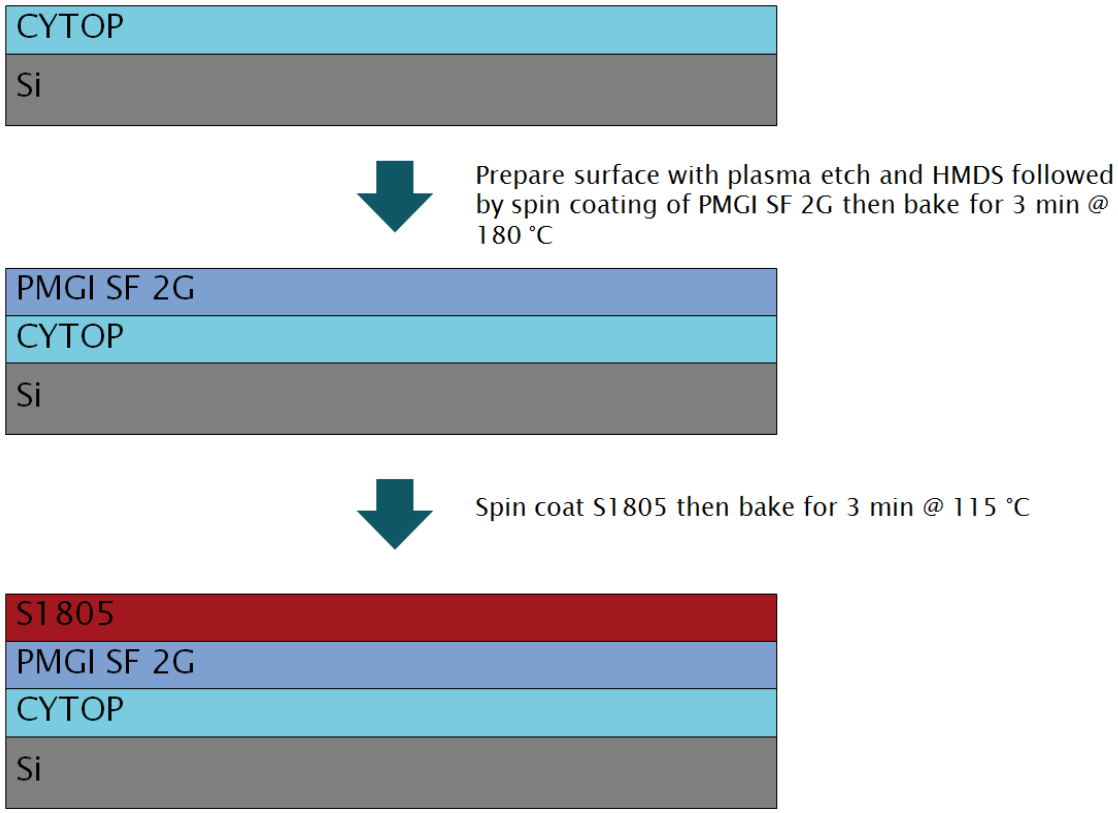

Figure 17: Bi-layer lithography process drawing

Exposure and Development

Definition of the waveguide structures is achieved through UV exposure of the S1805 photoresist. This is a positive tone photoresist, such that the portions of the film exposed to UV light become susceptible to the developer solution and as such is washed away leaving behind openings for subsequent deposition and lift-off of gold for realization of waveguide features. Exposure is achieved with the use of a Karl-Suss mask aligner, the specifications and prescribed exposure conditions are outlined in Table 6 below. The required exposure for a 600 nm layer of S1805 is known to be within the range of 7 to 8

seconds [6], this places the exposure energy density in the range of 80 to 180 mJ/cm^2 for the given lamp intensity.

Table 6: Mask aligner specifications and exposure conditions

Mask Aligner Specifications	
Make and Model	Karl Suss MA6 Mask Aligner
Lamp	350 W Mercury vapour
Measured Intensity Peaks	
@ 365 nm	8.4 mW/cm^2
@ 405 nm	14 mW/cm^2
Exposure Conditions	
Exposure energy	80 - 180 mJ/cm^2
Exposure time	7 - 8 seconds

The key components of the mask aligner and their orientation in relation to the wafer surface are illustrated in Figure 18. The wafer is held horizontally, by vacuum, in a chuck with the photoresist surface facing upwards. The device mask, portions of which are shown in Figure 19 , is placed in direct contact with the photoresist surface having the patterned side facing downwards. Pressure is applied mechanically by the chuck forcing the wafer upwards in order to eliminate any air gaps which may exist at the mask-wafer interface. Once exposure is desired, the shutter is opened allowing UV light to be guided by the mirrors and through the condenser lens towards the device mask. The mask itself is made of UV transparent glass, with a standard, patterned chromium film applied to the side

contacting the wafer. The patterning is done in such a manner allowing light to pass through the portions where removal of photoresist is desired. In other words, openings in the chromium mask correspond to the locations of the waveguides on the wafer surface once exposure, development, metallization and lift-off are complete.

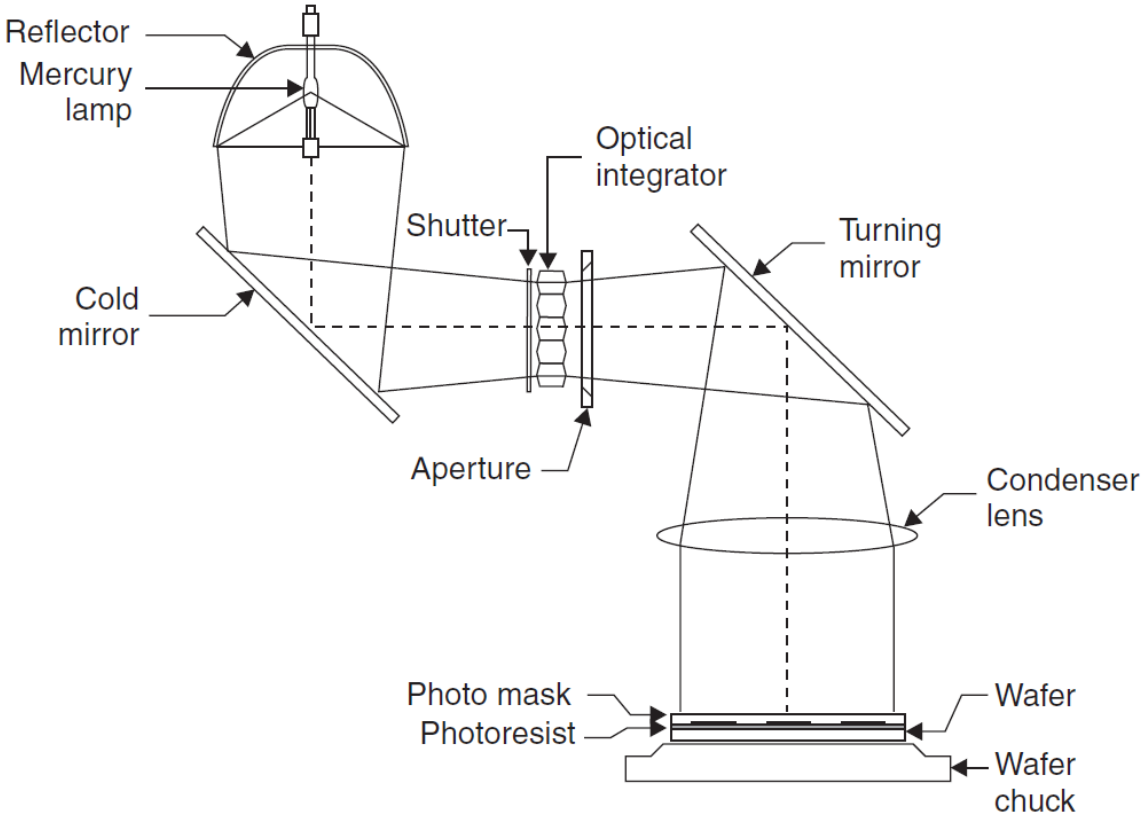

Figure 18: General mask aligner schematic showing component orientation in relation to wafer surface. Adapted from [18]

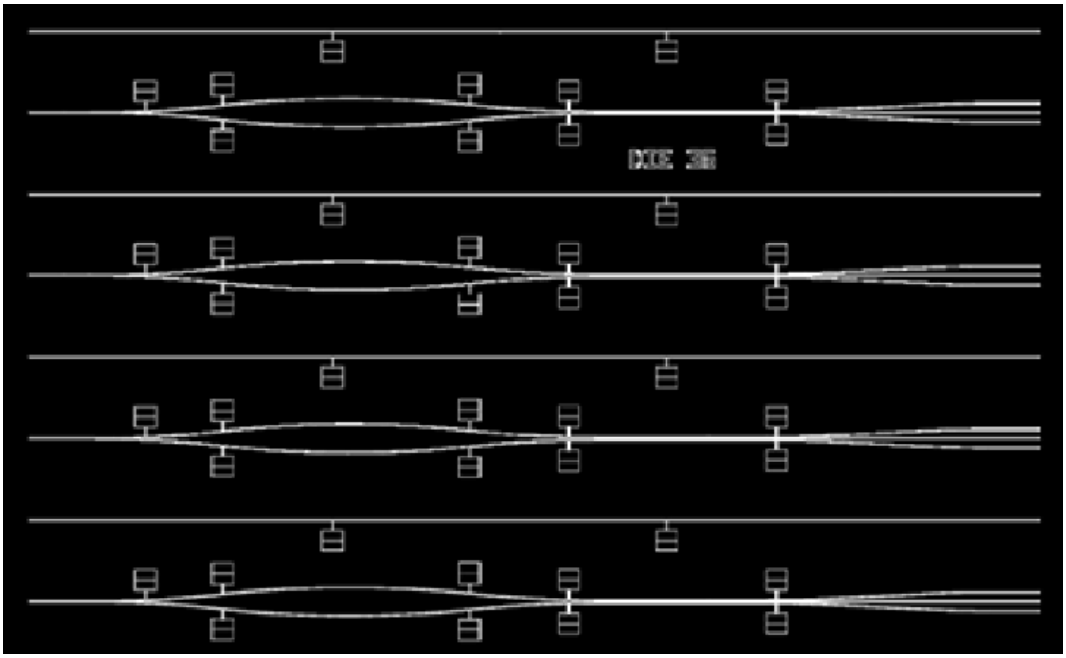

Figure 19: Sample device structure layout including MZI's, straight line waveguides and triple waveguides with contact pads. Adapted from [6]

The device layout shown in Figure 19 shows MZI's coupled to triple output waveguides and alternating straight line waveguides in between. After exposure the wafer is immersed in a room temperature bath of MF 321 developing solution, development time takes 2.5 minutes with a moderate level of agitation applied by hand. The developer bath removes the exposed portion of S1805 and the PMGI underneath. Since the lift-off resist is not photo-sensitive, the developer solution will continue to dissolve beyond the regions defined by the photoresist layer above. This is highly desirable and necessary in order for proper realization of the gold features. Care must be taken not to over-develop the wafers as washing out of the lift-off resist may occur; this phenomenon will be discussed in detail in section 3.3. Figure 20 shows a S1805 layer thickness of approximately 600 nm over a

PMGI layer thickness of approximately 75 nm and an undercut depth of roughly similar magnitude.

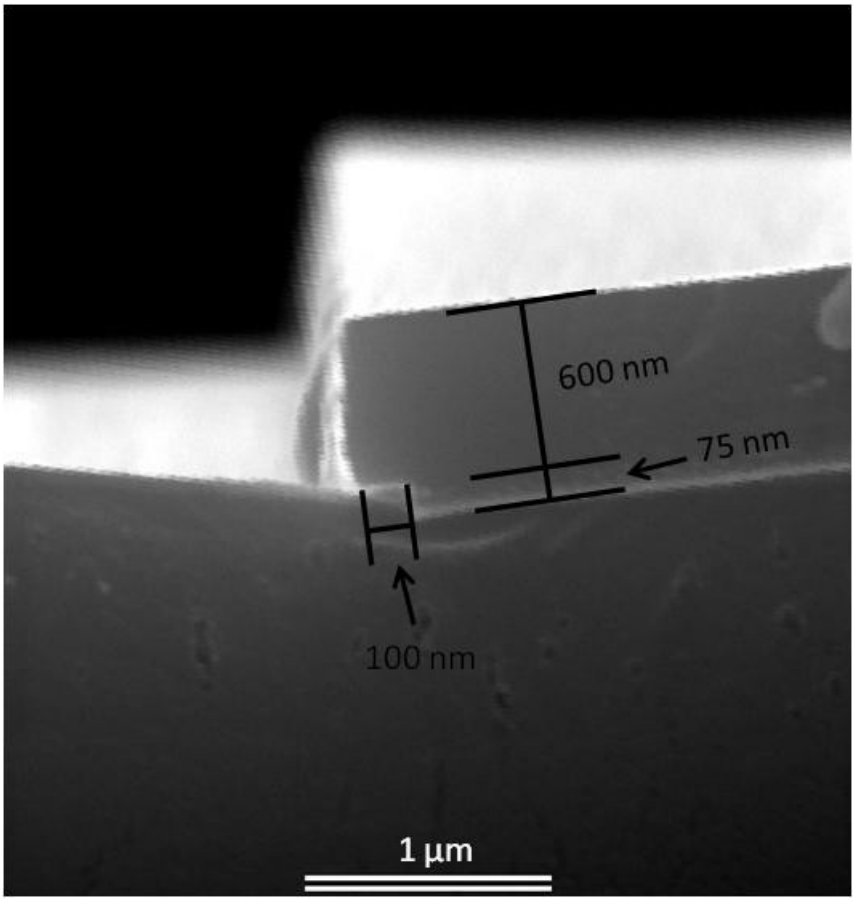

Figure 20: SEM image of developed bi-layer resist stack

During the alignment step, it is important to ensure that the waveguides are oriented perpendicularly to the long flat edge at the bottom of the wafer, shown in Figure 13. This is to avoid any issues that may arise during dicing, by aligning the waveguides such that the direction of propagation of the waves is at a 90 ° angle to the flat at the bottom of the wafer, the dies can then be cut along the crystallographic planes of the wafer, thus

avoiding any undesirable fracturing of the wafer which may cause damage to the devices and reduce the overall yield of the wafer. A procedural outline for exposure and development of the wafers is given in Table 7 and shown graphically in Figure 21.

Table 7: Processing steps for exposure and development of wafer for device feature definition.

Process Step	Description
Wafer Alignment	The flat at the bottom of the wafer is aligned such that the waveguides run in a perpendicular direction to it
Exposure	Wafer is exposed for 7 - 8 seconds under a 350 W mercury vapour bulb (80 - 180 mJ/cm^2)
Development	Wafer immersed in room temperature bath of MF 321 for 2.5 minutes (with medium to strong agitation approximately 75 nm of undercut is achieved, Figure 20)

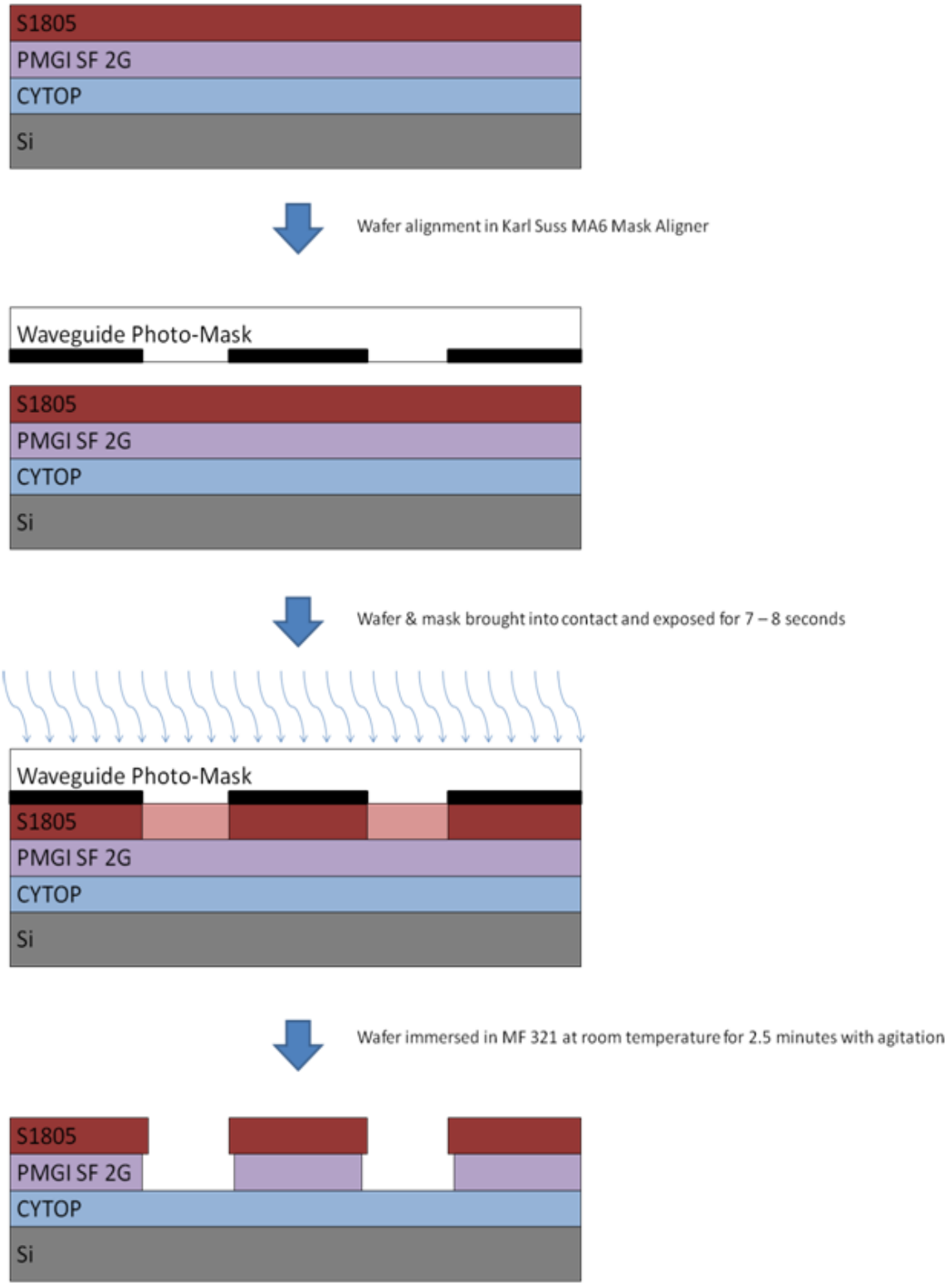

Figure 21: Wafer exposure and development process flow diagram

Metallization and Lift-off

Gold deposition is performed in a Balzer BA510 system retrofitted with the following pieces of equipment [19]:

- *CTI CryoTorr 8 Cryopump - used to achieve high vacuum in deposition chamber*
- *Sloan Planetary Fixture - holds wafers during deposition and is capable of rotation as well in order to reduce variations in film thickness*
- *Airco Temescal FDC 8000 automated deposition rate and film thickness controller - used to vary power available to e-beam in order to control deposition rate and film thickness*
- *Airco Temescal CV-8 e-beam system - power source for heating of deposition material*

These retrofits allow for accurate deposition of gold onto the wafer surface with a high degree of control and relatively low variability. Before deposition can occur, the exposed CYTOP surface must be primed in order to provide a suitable contact area for gold adhesion. This is done with a short, 30 second, exposure to O_2 plasma. This procedure is identical to the first step shown in Table 4, "Ashing", and serves to roughen the CYTOP surface slightly, giving the gold more surface area to bond to. The roughening effects of O_2 plasma on CYTOP are explained in further detail in section 5.3.

The short exposure time to the O_2 plasma is sufficient to properly prime the CYTOP surface for gold deposition while still leaving the patterned photoresist, and underlying lift-off resist, unaltered.

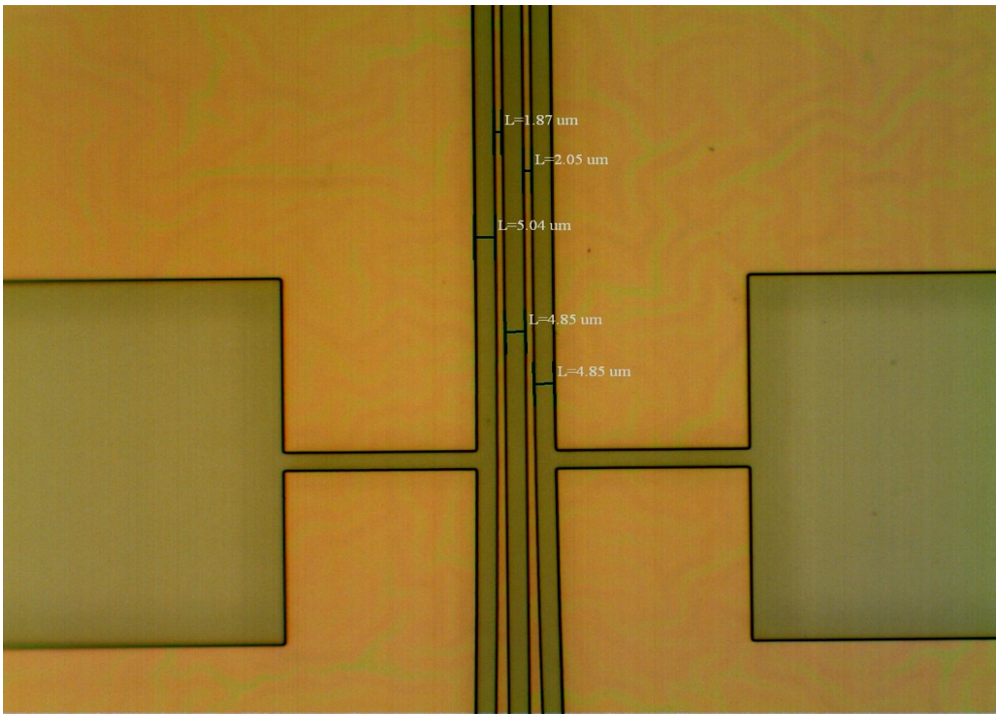

Figure 22: Pre-metallization microscope image of triple waveguide structure with contact pads (dimensions shown).

Figure 22, above, shows a close-up image of a triple waveguide structure prior to metallization; these are among the most challenging structures to fabricate on the layout given the need for accurate dimensions in waveguide line-width and spacing. As can be seen, the pattern remains fully intact with good resolution and proper dimensions after "ashing" is performed. The darker, greyer portions indicate areas where the photoresist/lift-

off resist stack has been washed away, while the lighter, yellower portions indicate areas that were blocked by the photo-mask and thus not susceptible to the developer solution.

Gold deposition is performed at a rate of 1 Å/s to achieve a total film thickness of 35 nm. The wafers are suspended upside down on the Sloan planetary fixture and held in place with magnets. The chamber is then brought under vacuum to a maximum pressure of 2×10^{-6} Torr absolute. Once vacuum is achieved, the e-beam source is brought up to a power of 12% during the "soaking" stage at a rate of 6% per minute followed by a much slower "pre-deposit" stage in which the power is brought up to 14% at a rate of 1% per minute. During the deposition stage, the maximum power is initially limited to 15%, once this power level is reached, the gold is allowed to stabilize for 1 minute, after which time the shutter is opened and the maximum power level is raised to 17%. By raising the power after the shutter is opened, the deposition rate is allowed to increase slowly, avoiding the formation of gold "spits" on the surface and minimizing the amount of gold used during the deposition process. Once deposition is complete, the shutter is closed, the power source is shut off, the chamber is allowed to cool for a period of 10 minutes then vented with high purity nitrogen for an additional 10 minutes in order to return the chamber to atmospheric pressure before opening and removing the wafers.

A small opening in the centre of the Sloan planetary fixture allows for the evaporant to deposit on a quartz crystal microbalance, which makes use of the gold density and its acoustic impedance to determine the deposition rate and film thickness. A general

schematic of the evaporator system is shown in Figure 23, indicating all major components and their orientation. The process used for deposition is outlined in Table 8, shown below.

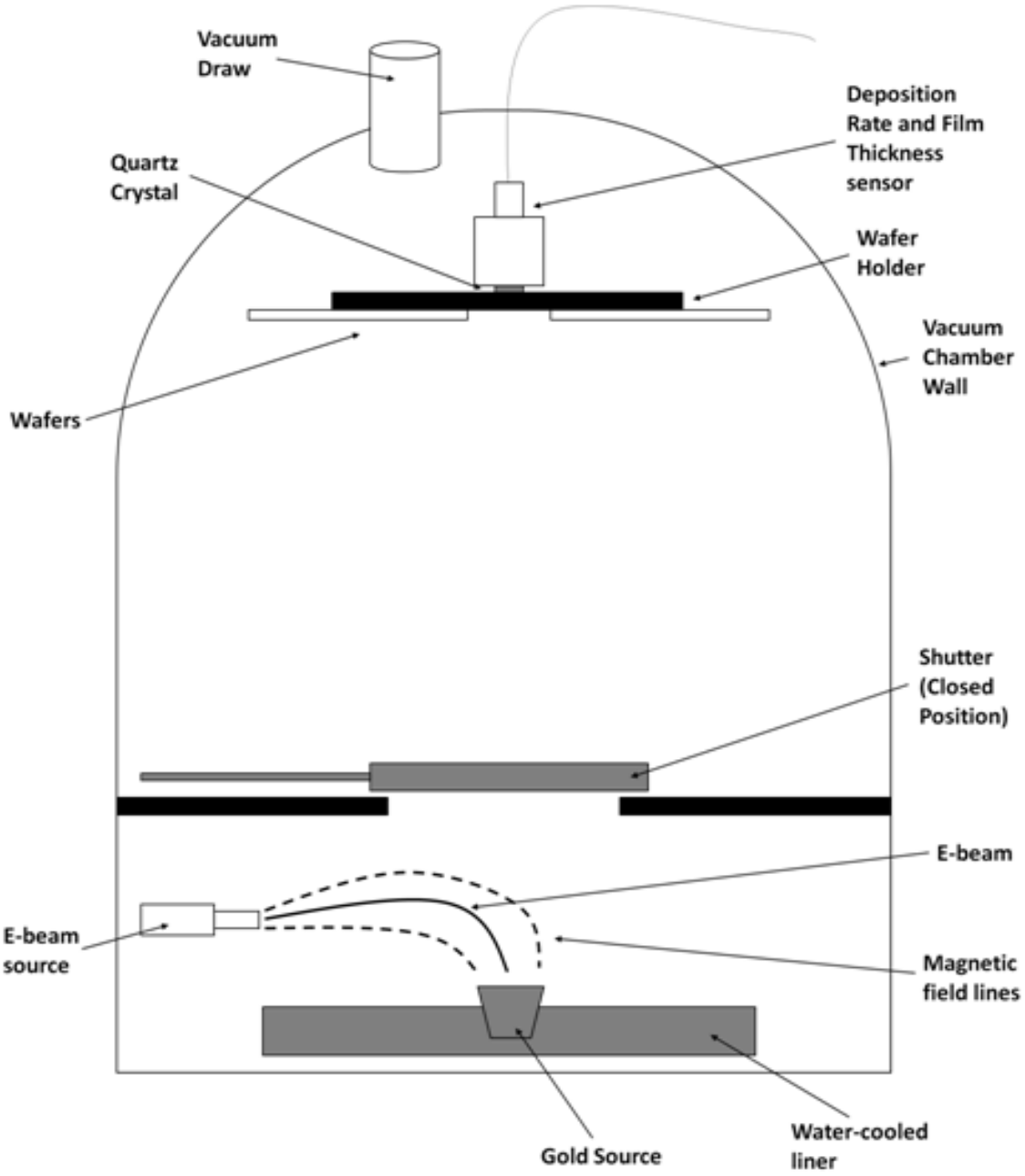

Figure 23: E-beam evaporator schematic

Table 8: Processing steps for gold deposition

Process Step	Description
Chamber Roughing	Vacuum chamber brought down from atmospheric pressure to 3×10^{-2} Torr abs. using roughing pump.
Cryogenic Pumping	Vacuum chamber further reduced in pressure to a maximum value of 2 × 10-6 Torr abs. using CTI CryoTorr 8 Cryopump.
Soaking	Airco Temescal CV-8 e-beam system brought up from 0 to 12% power in a span of 2 minutes at a rate of 6% per minute.
Pre-deposit	Airco Temescal CV-8 e-beam system brought up to 14% power in a span of 2 minutes at a rate of 1% per minute.
Deposition	Maximum power level set to 15% and allowed to stabilize for a minimum of 1 minute once power level is reached. Shutter is opened with power still at 15%, then maximum power level set to 17% and allowed to stabilize with use of Airco Temescal FDC 8000 automated deposition rate and film thickness controller in order to achieve deposition rate of 1 Å/s (at ~ 16.4%). Controller cuts power to e-beam once thickness reaches 35 nm. Shutter is closed at same time power is cut to avoid additional deposition of gold.
Cooling	Chamber is maintained under vacuum and allowed to cool for a period of 10 minutes.
Venting	Chamber is vented with nitrogen gas for 10 minutes to return to atmospheric pressure before opening.

Following deposition, the lift-off procedure is performed using two sequential heated baths of Microposit 1165 remover. This strips off the PMGI and S1805 while leaving

the waveguide structures and CYTOP fully intact. The wafer is immersed in the first bath, maintained between 70 - 80 °C, for a period of 10 minutes with no agitation. Following this the entire 1165 bath is placed in an ultrasonic bath for 10 seconds to strip away a majority of the gold. The wafers are then placed in a second 1165 bath, also between 70 - 80 °C, for an additional 10 minutes followed by another ultrasonic bath for 10 seconds. At this point, all that remains is the gold waveguides on top of the CYTOP bottom cladding (due to strong adhesion between CYTOP and gold [6]). The wafers are then immersed in isopropyl alcohol for 10 minutes to clean off any residue remaining after the lift-off procedure and finally rinsed with de-ionized water to finish cleaning the surface. The lift-off procedure is outlined in Table 9 as well as the entire deposition and lift-off procedure in Figure 24 shown below.

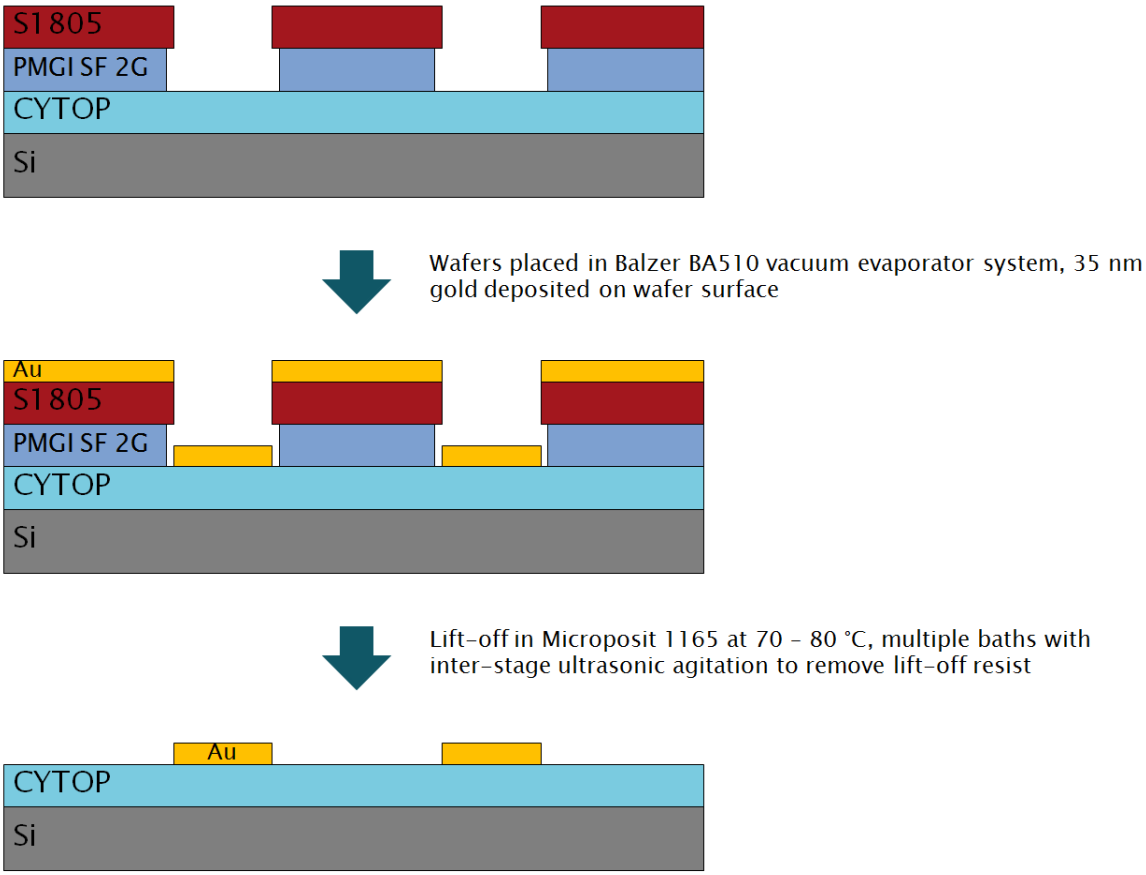

Figure 24: Gold deposition and lift-off process flow diagram

Table 9: Processing steps for gold lift-off

Process Step	Description
Microposit 1165 Bath 1	Bath temperature raised to 70 - 80 °C, wafers immersed for 10 minutes.
Ultrasonic Bath 1	Wafer and 1165 bath placed in larger water bath and exposed to ultrasonic vibration for 10 seconds to strip off majority of lift-off resist.
Microposit 1165 Bath 2	Bath temperature raised to 70 - 80 °C, wafers immersed for 10 minutes.
Ultrasonic Bath 2	Wafer and 1165 bath placed in larger water bath and exposed to ultrasonic vibration for 10 seconds to strip off remainder of lift-off resist.
IPA Bath	Wafers immersed in high purity isopropyl alcohol bath for 10 minutes.
DI Water Rinse	Wafers rinsed off with de-ionized water.
Nitrogen Spray	Wafers sprayed with high purity nitrogen jet to dry off water.

3.3. Results and Discussion

The deposition procedure explained above is a modification to the procedure outlined in [6]. The purpose of the modification was to slow down the deposition rate by performing a more gradual heating in the "deposition" stage discussed in Table 8. By opening the shutter at only 15% power as opposed to 17% power, the deposition rate is still at 0 Å/s. The power then slowly increases in order to achieve a rate of 1 Å/s at about 16.4% power. The previous process had the deposition rate set to 2 Å/s and called for the shutter to be opened after the power level had reached 17%. This resulted in a much higher initial

deposition rate and consequently yielded gold "spits" which were visible on the gold surface as small, randomly dispersed dots, illustrated in Figure 25 a).

Figure 25 b), shows the gold surface generated by the new process, in which a substantial reduction in "spits" on the gold surface is evident. AFM scans of small, 3 µm × 3 µm, patches of the gold surface for both the old and new deposition procedures are shown in Figure 26 a) and b) respectively. The scale on the left indicates the rms roughness of 23 nm and an average roughness of 18 nm due to the presence of "spits" on the gold surface in Figure 26 a). Comparatively, Figure 26 b) shows a gold surface generated by the modified procedure, in which the rms roughness has been reduced to 0.7 nm and the average roughness down to 0.5 nm. This is a drastic decrease in the waveguide roughness resulting in a substantial improvement in optical and biological performance, evident in the characterization of the devices in section 5.3. This is supported by claims made in [14], in which surface and edge roughness of the devices may lead to additional losses, reducing the wave propagation distance and consequently the device sensitivity [6], [15].

It should be noted that the contact pads shown in Figure 25, as well as in subsequent images, serve only to allow for electrochemistry (use of potential differences to drive chemical reactions on gold surface) and thermo-optic modulation (electrical resistance heating of gold and surrounding medium to alter refractive indices thus changing wave propagation characteristics). At this point the contact pads require additional deposition of metal in order to improve robustness (35 nm too thin to withstand continual probing with electrodes), the figures included in this thesis are used primarily due to the

fact that they provide a large metallic structure by which qualitative observations of the gold surface are easily obtained.

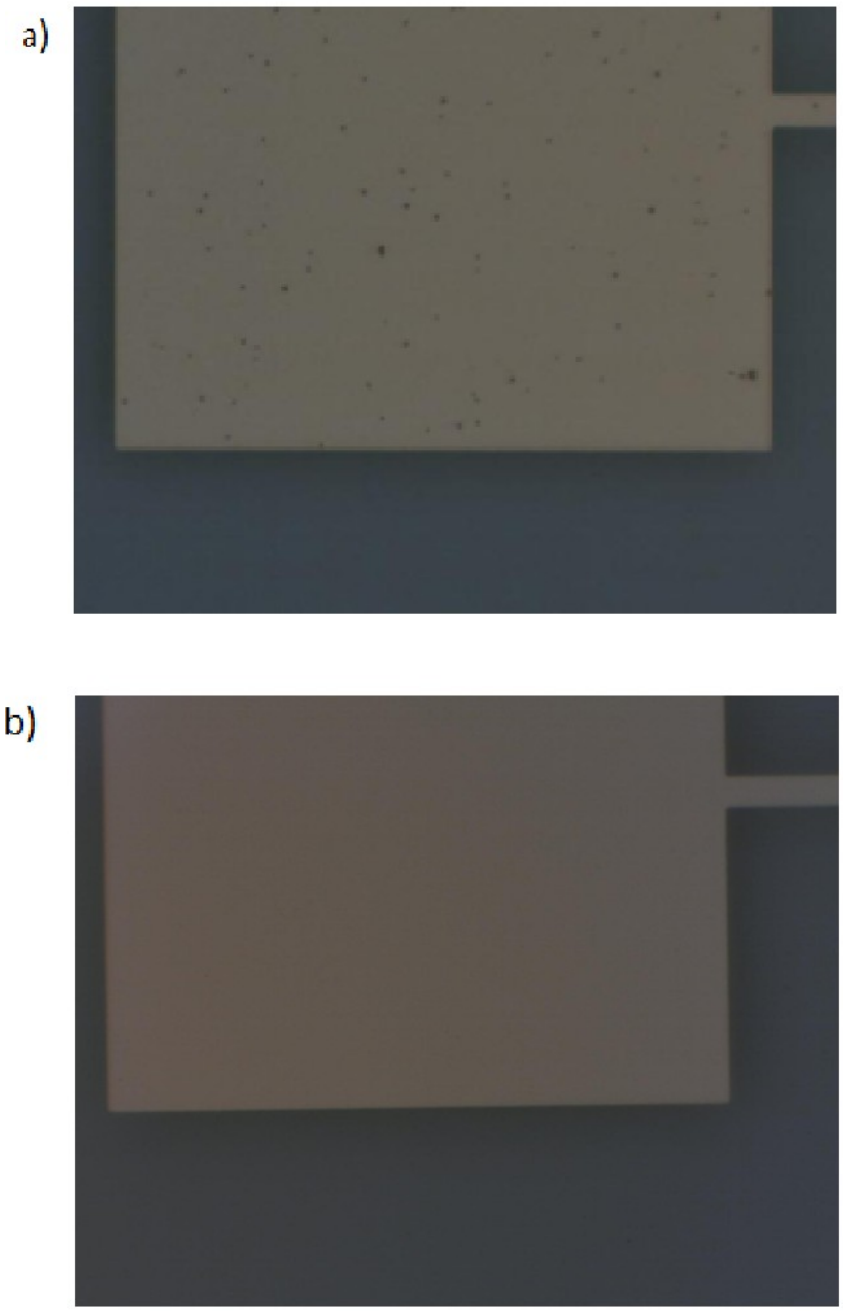

Figure 25: Gold contact pads after lift-off a)showing spits on surface using old deposition procedure [6], b) showing no spits on surface using modified deposition procedure.

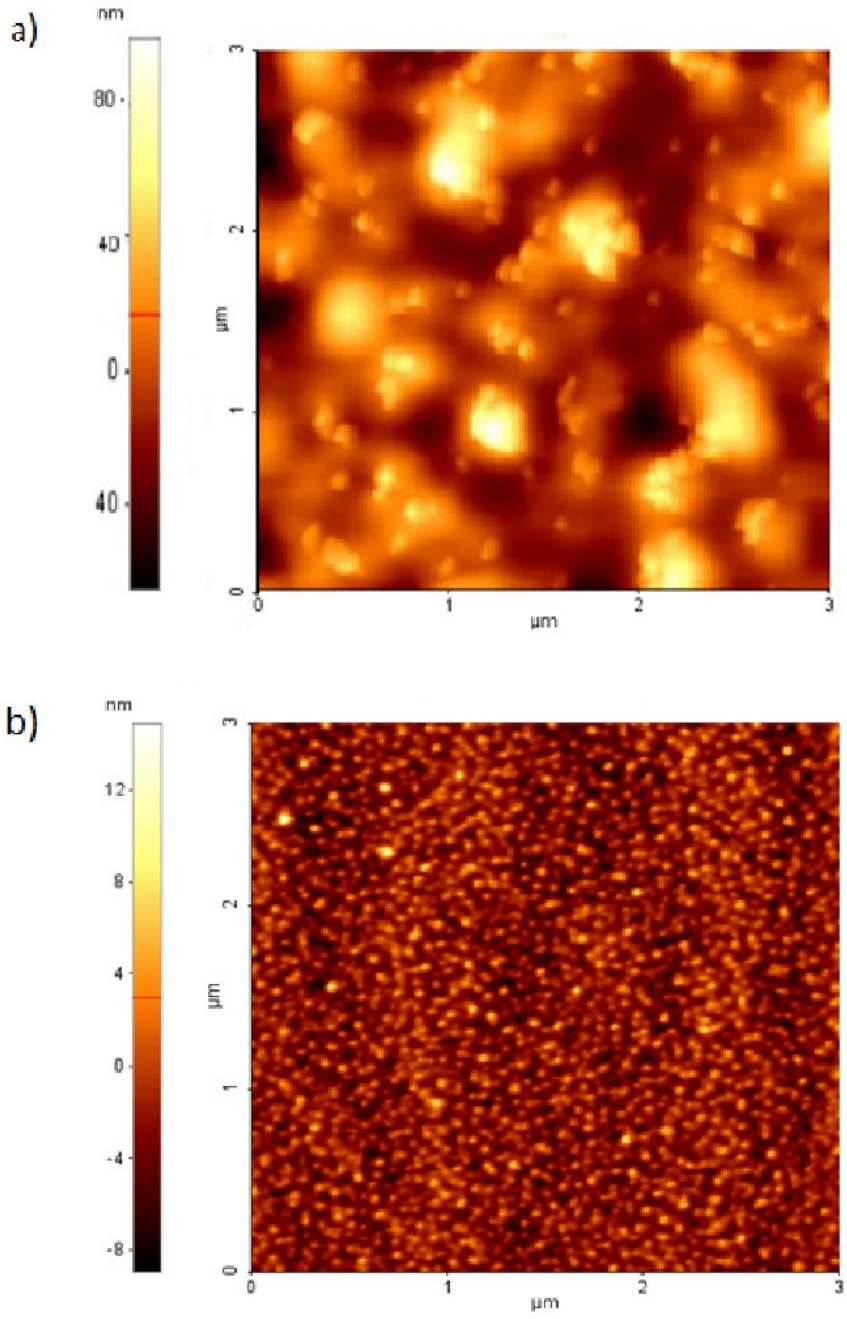

Figure 26: AFM images of gold surface a) showing surface with spits fabricated using old deposition procedure (rms roughness = 23 nm, avg. roughness = 18 nm). Adapted from [6]. b) showing no spits on gold surface using new deposition procedure (rms roughness = 0.7 nm, avg. roughness = 0.5).

After lithography, deposition and lift-off, the metal patterns may be viewed under high magnification. Upon close visual inspection, benefits of the changes made to the lithography procedure become evident. As mentioned in section **Error! Reference source ot found.**, improvement in feature resolution by substituting the lift-off resist is realized. By using PMGI SF 2G instead of the LOR-1A, device quality is greatly improved upon due to the slower dissolution of the lift-off layer. If the dissolution rate is too high, then the risk of over-development increases and feature definition is compromised. Over-development refers to the washing out of the lift-off resist layer beneath the photoresist layer causing a lack of structural support. This is most evident when inspecting the Y-Junctions shown in Figure 27 a) and b) below. When using LOR-1A, the Y-Junction has a rounded profile, Figure 27 a), which may lead to an uneven split in the wave power and render the MZI structures unusable. Reducing the dissolution rate of the lift-off resist by switching to PMGI SF 2G yields a sharper corner profile (Figure 27 b)), producing an even distribution of optical power between the two arms of the structure.

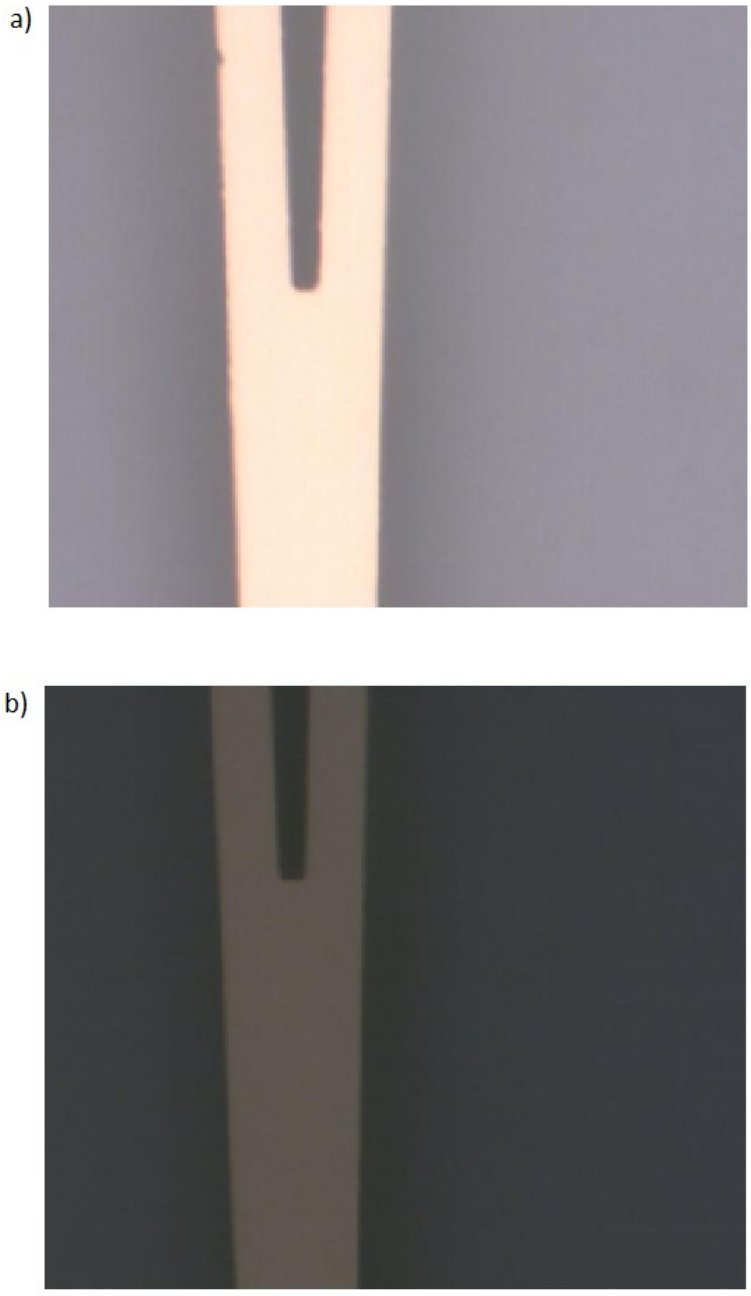

Figure 27: 2 micron Y-Junction of MZI, a) fabricated using LOR-1A lift-off resist, b) fabricated using PMGI SF 2G lift-off resist.

The cause of the rounded edge profile in Figure 27 a) was determined to be washing out, or over development of the lift-off resist near the split. This results in excessive loss of

structural support below the patterned photoresist, and as such, causes the photoresist to fall out of position, as shown below in Figure 28. A representative schematic of this phenomenon is also shown in Figure 29. Figure 28 also shows very poor edge roughness of defining structures when LOR-1A is used as the lift-off resist.

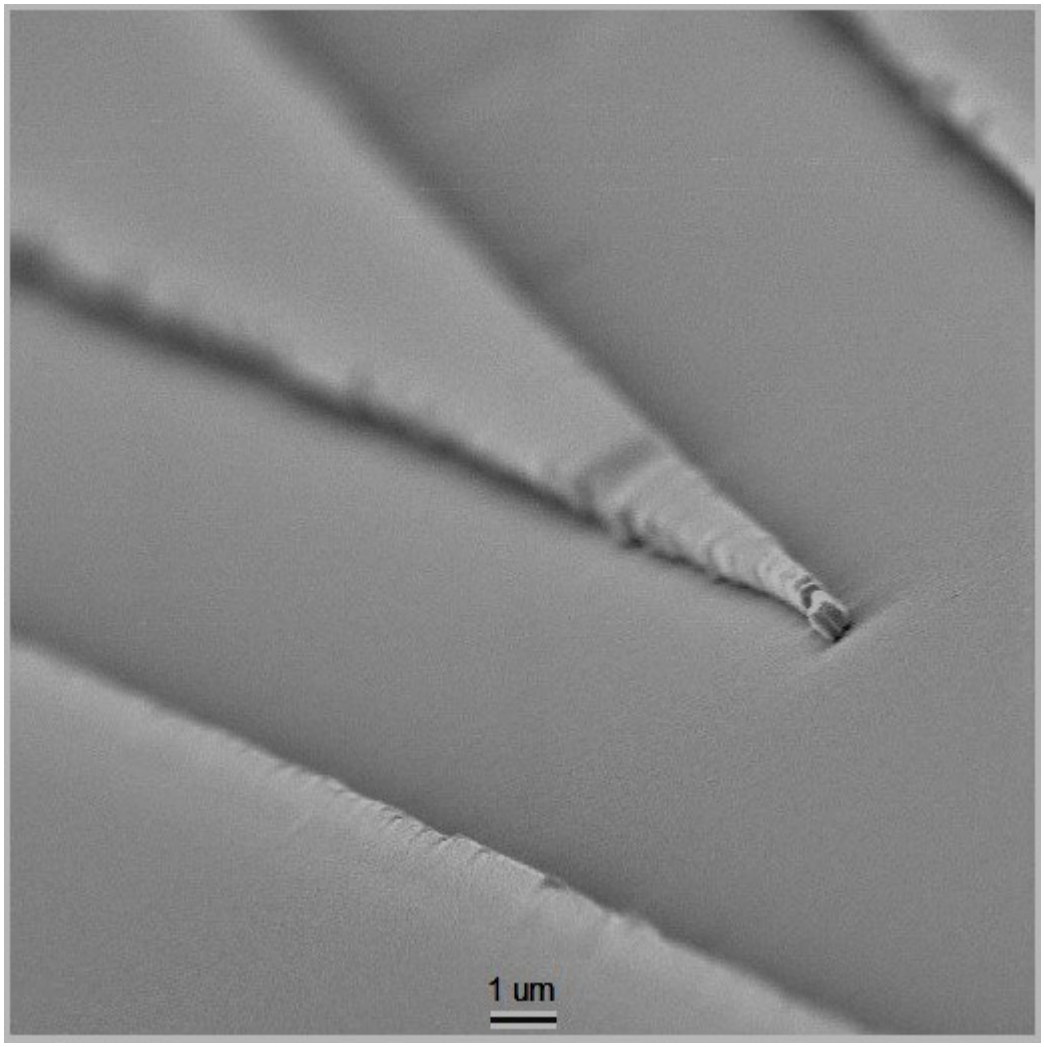

Figure 28: SEM image of Y-Junction produced using LOR-1A showing wilting of upper layer due to loss of support from overdevelopment of lift-off layer.

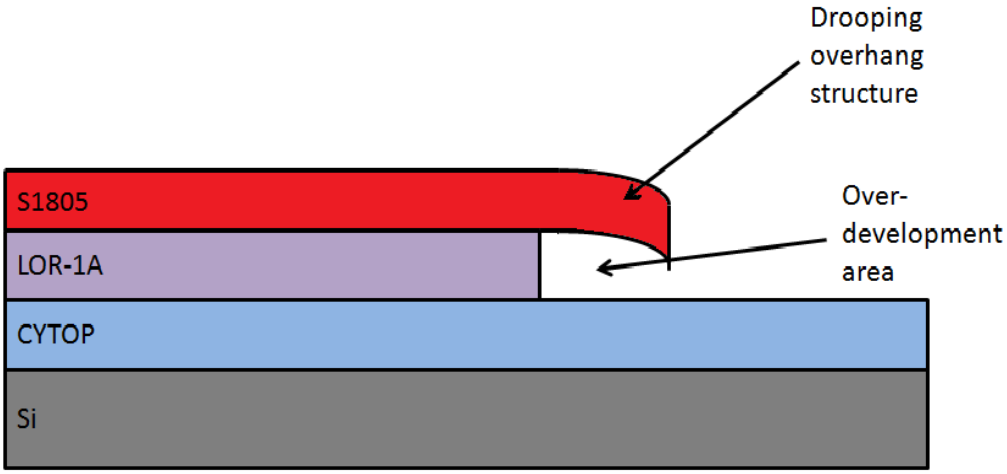

Figure 29: Representative schematic of patterning layer wilting due to washing out of LOR-1A

The differences between the dissolution rates of various lift-off resists offered by Microchem can be seen in below in Table 10. As the table indicates, the PMGI slow series polymer develops at a rate of approximately one fourth to that of the LOR A class polymer when baked at 190 °C.

Table 10: Relative dissolution rates and prebake temperature dependency of Microchem lift-off resists [20].

Prebake Temperature (°C)	Relative Dissolution Rate (Å/s)				
	LOR A	LOR B	PMGI Fast	PMGI Medium	PMGI Slow
150	111	333	83	56	21
170	67	222	42	28	14
190	42	167	28	17	10

*** Developer used contains 2.38% TMAH (tetramethylammonium hydroxide), MF 321 contains 1.91% TMAH. Dissolution rates assumed to be linearly proportional to TMAH content.**

Figures 30 a) and b) show triple and double output waveguides, respectively, after lift-off when using PMGI SF 2G as the lift-off resist. Figure 30 c) shows the effects of over development on a triple output waveguide when using LOR-1A. Clear migration of the photoresist layer is observed resulting in the need to rework the bi-layer lithography procedure. This results from two collaborating phenomena, over-development and insufficient baking temperatures.

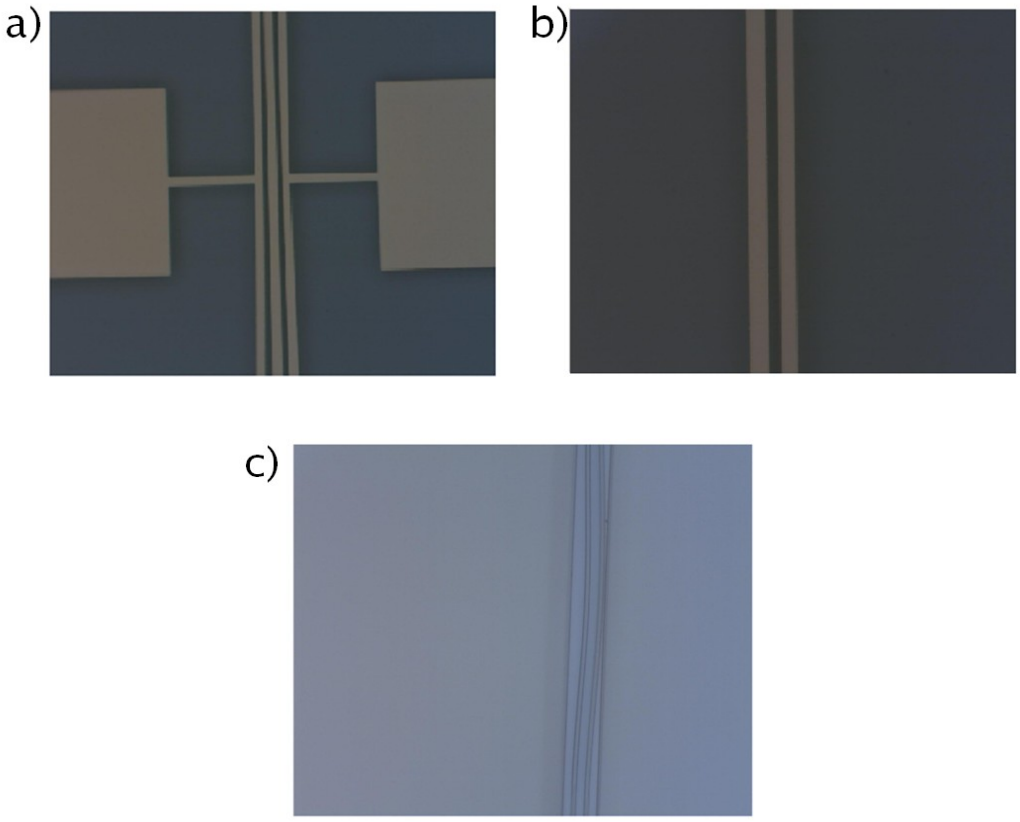

Figure 30: a) triple straight waveguides, b) double straight waveguide and c) photoresist layer migration in triple waveguides due to over-development of LOR-1A lift-off layer.

The dissolution rate of the lift-off resist is strongly affected by the baking temperature; by increasing the baking temperature, a larger amount of solvent may be driven from the film, aiding in the densification process. As the film density increases, so does its resistance to dissolution by the developer solution, as indicated by Table 10. In the procedure outlined in Table 5, the baking temperature of the lift-off resist is set to 180 °C, this is despite the manufacturer's recommendation to perform the baking step at a minimum temperature of 185 °C [21]. By baking below the recommended temperature, there may be a residual amount of solvent still trapped within the polymer matrix (LOR-1A or PMGI SF 2G films), resulting in a lower film density than intended. This will effectively reduce the lift-off layers resistance to the developer solution, leading to further complications with over-development and adding to the reasons for switching to a slower dissolving polymer.

4. Top Cladding

4.1. Objectives

This chapter outlines the application procedure for the upper CYTOP cladding, necessary for formation of the fluidic channels used to allow passage of the sensing medium over the gold waveguides previously discussed. The procedure outlined is based primarily on a similar procedure described in ***Chiu et. al 2009***, with modifications made to the baking temperature used in between the spin coating of each additional layer of CYTOP. The motivation behind the modifications was due to an excessive amount deformation in the thin gold film which may adversely affect the waveguide operation. By increasing the baking temperature of each CYTOP layer prior to application of the subsequent layer, the amount of solvent may be minimized effectively reducing the diffusion rate of solvent further beneath the device layer (see Appendix C for detailed diffusion characterization).

4.2. Materials and Methods

The upper CYTOP cladding is deposited in a similar fashion to that of the lower cladding described in section 2.3, with a few important modifications to improve the gold waveguide quality. Before spin coating, the surface must be prepared to facilitate adhesion of the new CYTOP layer to that below the devices. This is achieved with an O_2 plasma etch carried out at 100 W, 300 mTorr and 220 sccm of O_2. The wafer surface is exposed to the O_2 plasma for a period of 30 seconds, which is identical to the "ashing" procedure outlined in Table 4 and serves the same purpose.

Following the surface preparation, the first layer of the top cladding may be applied. This is done by spin coating a thin layer of CTX-809SP2 (S-grade CYTOP) using a 1000 rpm spread spin for 10 seconds followed by a planarizing spin at 4000 rpm for 20 seconds. This layer is then baked at 50 °C for 30 minutes on a direct contact hot plate. The hot plate is then ramped up from 50 °C to 100 °C at a rate of 25 °C/hr then maintained at 100 °C for an additional 4 hours. This yields an approximate layer thickness of 1.1 μm of CYTOP [16]. This process is repeated an additional 6 times with a 30 second O_2 plasma etch before each additional layer is spun on. It has been observed in some samples that small gas pockets form between hard baked layers of CYTOP when the wafer is placed under vacuum, specifically in the plasma etching chamber. This effect has been noted to be reduced significantly, if not eliminated entirely, when the substrate layer has gone through an "ashing" step prior to spin coating.

By the 7th layer, a total upper cladding thickness of 7.7 μm is achieved. The entire procedure, which is a modification of the upper cladding process described in [6], is outlined in Table 11 and illustrated in Figure 31. The main alteration is the addition of a high temperature bake following the spin coating of each layer. This serves to minimize the amount of solvent in the CYTOP prior to application of each additional coat.

CYTOP has a glass transition temperature of 108 °C, and since the baking temperature of the top cladding is limited to 100 °C, there is still a small amount of solvent trapped in the layer. In the previous process [6], the bake temperature between layers was limited to 50 °C followed by a single high temperature bake after the final layer was

deposited. By increasing the bake temperature between layers, a noticeable improvement in device quality was observed after the top cladding was applied. The original process showed significant waveguide deformation due to solvent seeping underneath the gold film (into the lower cladding); this problem will be discussed in detail in section 4.3.

Table 11: Upper cladding fabrication procedure.

Process Step	Description
Şurface Prep	30 sec O_2 plasma etch at 100 W, 300 mTorr and 220 sccm
1st Spin Coat	CTX-809SP2 spun at 1000 rpm for 10 sec then 4000 rpm for 20 sec
1st Bake	Bake at 50 °C for 30 min, ramp at 25 °C/hr for 2 hrs then hold at 100 °C for 4 hrs. Follow with 30 sec O_2 plasma etch at 100 W, 300 mTorr and 220 sccm
2nd Spin Coat	CTX-809SP2 spun at 1000 rpm for 10 sec then 4000 rpm for 20 sec
2nd Bake	Bake at 50 °C for 30 min, ramp at 25 °C/hr for 2 hrs then hold at 100 °C for 4 hrs. Follow with 30 sec O_2 plasma etch at 100 W, 300 mTorr and 220 sccm
3rd Spin Coat	CTX-809SP2 spun at 1000 rpm for 10 sec then 4000 rpm for 20 sec
3rd Bake	Bake at 50 °C for 30 min, ramp at 25 °C/hr for 2 hrs then hold at 100 °C for 4 hrs. Follow with 30 sec O_2 plasma etch at 100 W, 300 mTorr and 220 sccm
4th Spin Coat	CTX-809SP2 spun at 1000 rpm for 10 sec then 4000 rpm for 20 sec
4th Bake	Bake at 50 °C for 30 min, ramp at 25 °C/hr for 2 hrs then hold at 100 °C for 4 hrs. Follow with 30 sec O_2 plasma etch at 100 W, 300 mTorr and 220 sccm
5th Spin Coat	CTX-809SP2 spun at 1000 rpm for 10 sec then 4000 rpm for 20 sec
5th Bake	Bake at 50 °C for 30 min, ramp at 25 °C/hr for 2 hrs then hold at 100 °C for 4 hrs. Follow with 30 sec O_2 plasma etch at 100 W, 300 mTorr and 220 sccm
6th Spin Coat	CTX-809SP2 spun at 1000 rpm for 10 sec then 4000 rpm for 20 sec
6th Bake	Bake at 50 °C for 30 min, ramp at 25 °C/hr for 2 hrs then hold at 100 °C for 4 hrs. Follow with 30 sec O_2 plasma etch at 100 W, 300 mTorr and 220 sccm
7th Spin Coat	CTX-809SP2 spun at 1000 rpm for 10 sec then 4000 rpm for 20 sec

7^{th} Bake	Bake at 50 °C for 30 min, ramp at 25 °C/hr for 2 hrs then hold at 100 °C for 4 hrs. Follow with 30 sec O_2 plasma etch at 100 W, 300 mTorr and 220 sccm

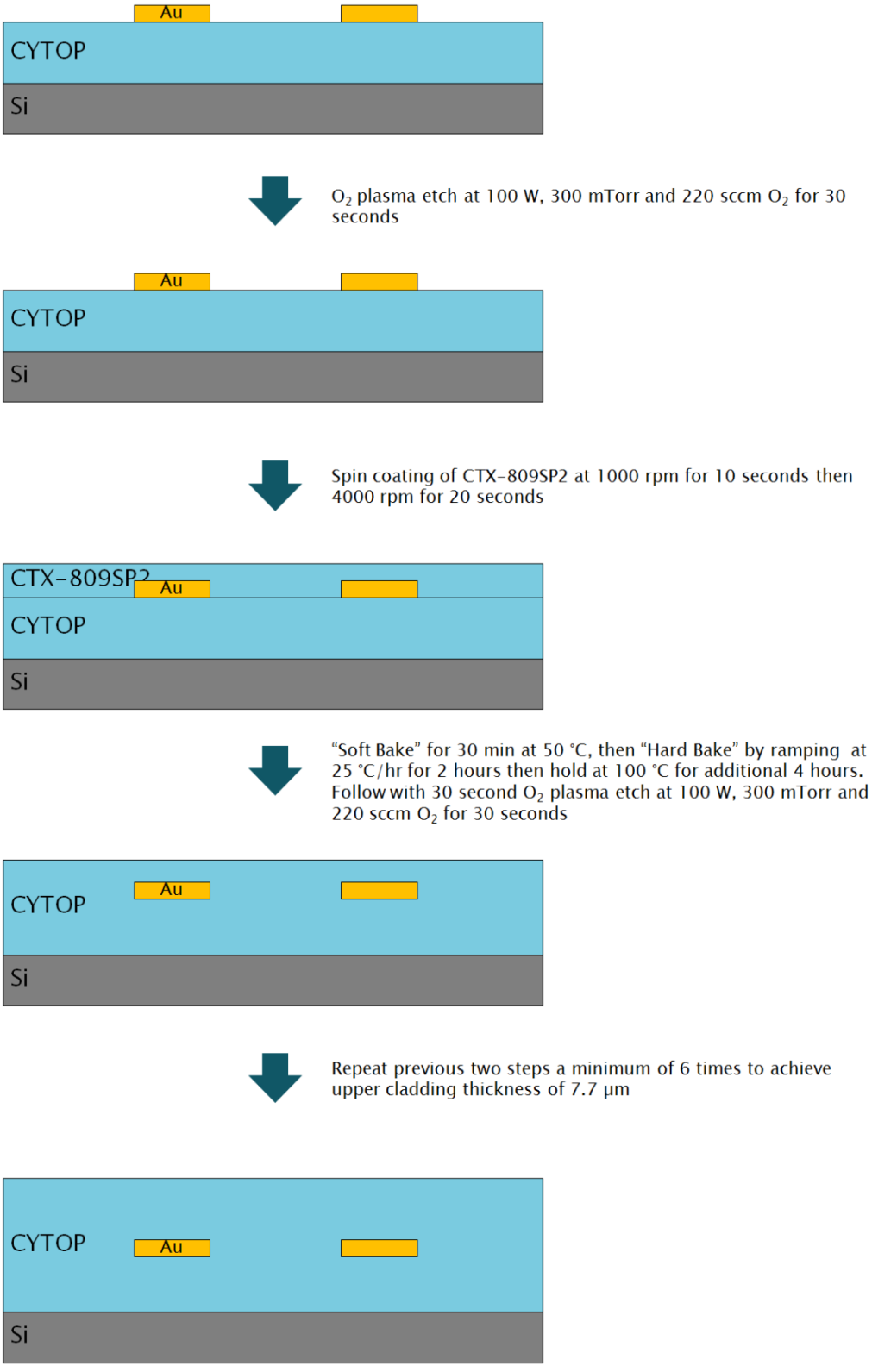

Figure 31: CYTOP upper cladding process flow diagram.

It should be noted that a total of 7 upper cladding layers are used in order to achieve a minimum thickness of 7.7 µm. Due to the substantial reduction of solvent trapped in the cladding, it is possible to deposit as many as 18 layers giving a total upper cladding thickness of approximately 20 µm. This will potentially allow for realization of deeper flow channels leading to the capability of sensing larger analytes such as white blood cells and bacteria.

4.3. Results and Discussion

In order for the devices to be able to support LRSPP's, they must be fully bound in a dielectric medium such that both upper and lower surfaces of the waveguides are in contact with media of identical refractive index. Furthermore, the material must be easily and selectively removable to allow for access to the gold surface via microfluidic channels. For these reasons, amongst others, CYTOP is used as the dielectric material in these devices. CYTOP is received as a 9 wt% solids solution and is applied to the wafer by means of spin coating. This process requires a high solvent content to allow for smooth, planar surfaces and sufficient polymer chain migration across CYTOP to CYTOP interfaces to prevent delamination.

The CYTOP solvent, CTSOLV 180, is removed from the film by baking on a hot plate. This process is slow and allows the solvent sufficient time to seep into previously deposited layers below. Throughout the bottom cladding fabrication procedure, this phenomenon is of little relevance, providing simply the means for entanglement of polymer chains between

the CYTOP layers, ultimately having no effect on the quality of the final structure. Conversely, once the gold waveguides have been patterned and deposited, solvent ingress becomes a much more relevant issue during formation of the upper cladding and may have significant effects on the waveguide structure.

The bottom cladding is baked at 200 °C, this temperature is well above the glass transition temperature of CYTOP resulting in complete removal of the solvent. This gives a slow initial rate of diffusion of solvent from the top cladding layers into the bottom cladding, as additional layers are spun on to build up the upper cladding thickness, the solvent begins to accumulate below the device level, deforming the gold structures.

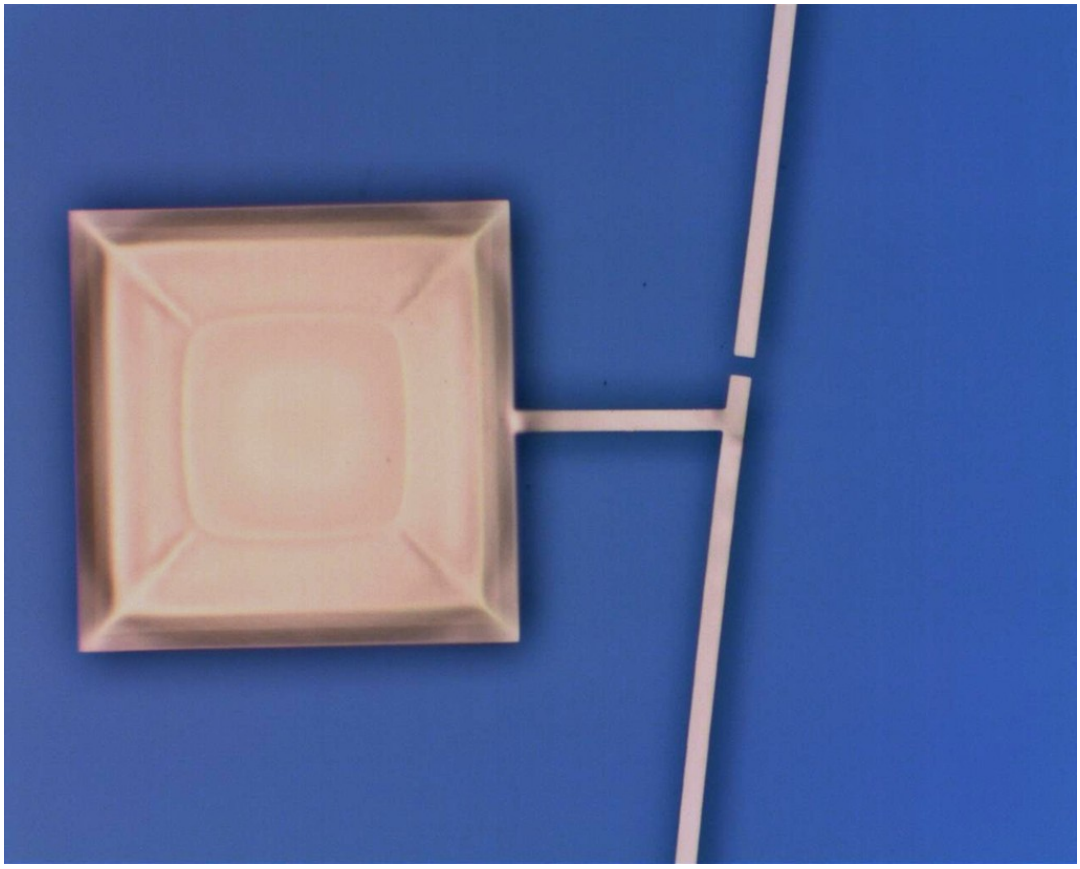

Figure 32: Typical deformation pattern of contact pad fabricated using top cladding procedure outlined in [6].

Figure 32, shown above, illustrates a typical deformation pattern of a contact pad fabricated using the top cladding process described in [6]. The above photo also shows deformation of the "Tee" connection from the contact pad to the waveguide and an increased separation in the gap. The separation in the gap is a result of the solvent penetrating beneath the waveguide and lifting the outermost edges, a schematic of this is shown in Figure 33 a) and b). Figure 33 c) and d) also illustrate a “bowing” effect that the straight waveguides exhibit due to solvent ingress, this will be explained further in Chapter 5.

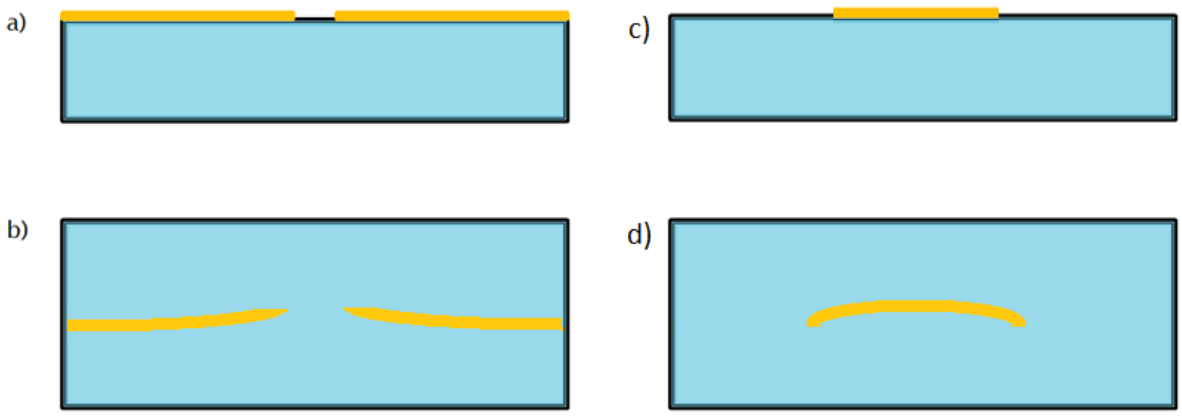

Figure 33: Schematic illustrating separation of 2 µm gap a) before top cladding application, b) after top cladding application, c) straight waveguide prior to upper cladding application, d) straight waveguide after upper cladding application.

After the first layer of the top cladding is applied, there is little to no apparent deformation of the devices when using either the old [6] or the new (described herein) procedure. This is likely due to the large difference between the molecular diffusion rate at the bottom surface and the convective diffusion rate at the upper surface. Once the second layer is applied, however, the impact of the solvent content within the first layer becomes apparent. Figure 34 illustrates the extent of deformation early in the top cladding fabrication process. The difference is a result of two collaborating conditions, the first being the residual solvent content within the previously deposited CYTOP layer and the second being the temporary reversal of the solvent concentration gradient. Of these two conditions, the only one that can be rectified by adjusting the processing conditions is the solvent concentration. By reducing the concentration in the layers closest to the devices,

the diffusion rate can be significantly reduced when the concentration gradient of solvent is temporarily reversed during application of the subsequent layers.

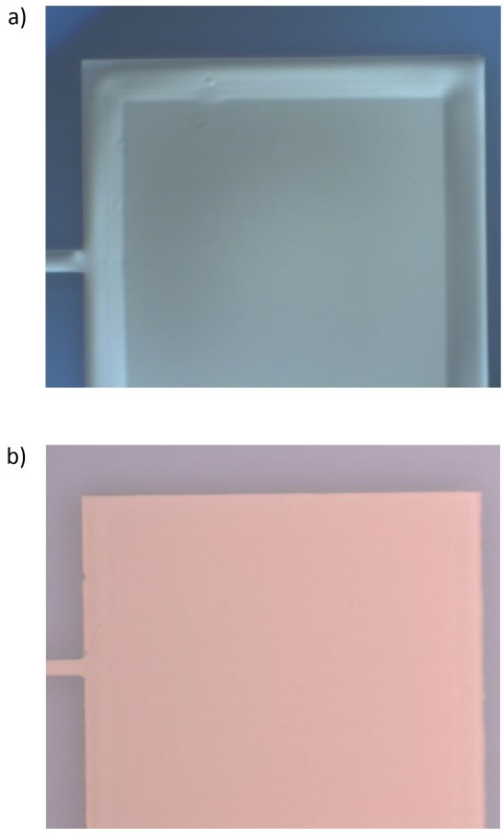

Figure 34: Difference in device deformation after 2nd layer of top cladding a) using old procedure [6], b) using new procedure.

The reversal of the concentration gradient is illustrated in the schematic diagrams shown below. Figure 35, using the old upper cladding fabrication procedure [6], compared to Figure 36, using the new upper cladding fabrication procedure, has a substantially higher residual solvent content in the first upper cladding layer. As the second layer is deposited, the solvent concentration at the upper surface of the first layer goes from being effectively

zero to 91% by weight. Until the solvent concentration in the second layer is reduced to an equivalent value of the solvent concentration in the first layer, solvent will be forced to diffuse inwards into the bottom cladding, resulting in swelling of the CYTOP and ultimately forcing the gold devices to deform and shift from their desired positions. This effect is compounded with the application of each additional layer and, while being unavoidable, can be reduced by minimizing the solvent content in the layers closest to the gold devices, thus reducing the rate of solvent ingress.

Baking each layer at 100 °C as opposed to 50 °C helps to reduce the solvent content without exceeding the glass transition temperature of CYTOP. Since the baking temperature is still below the glass transition temperature, there is still some solvent remaining within the upper cladding layers, albeit significantly lower than if only baked at 50 °C.

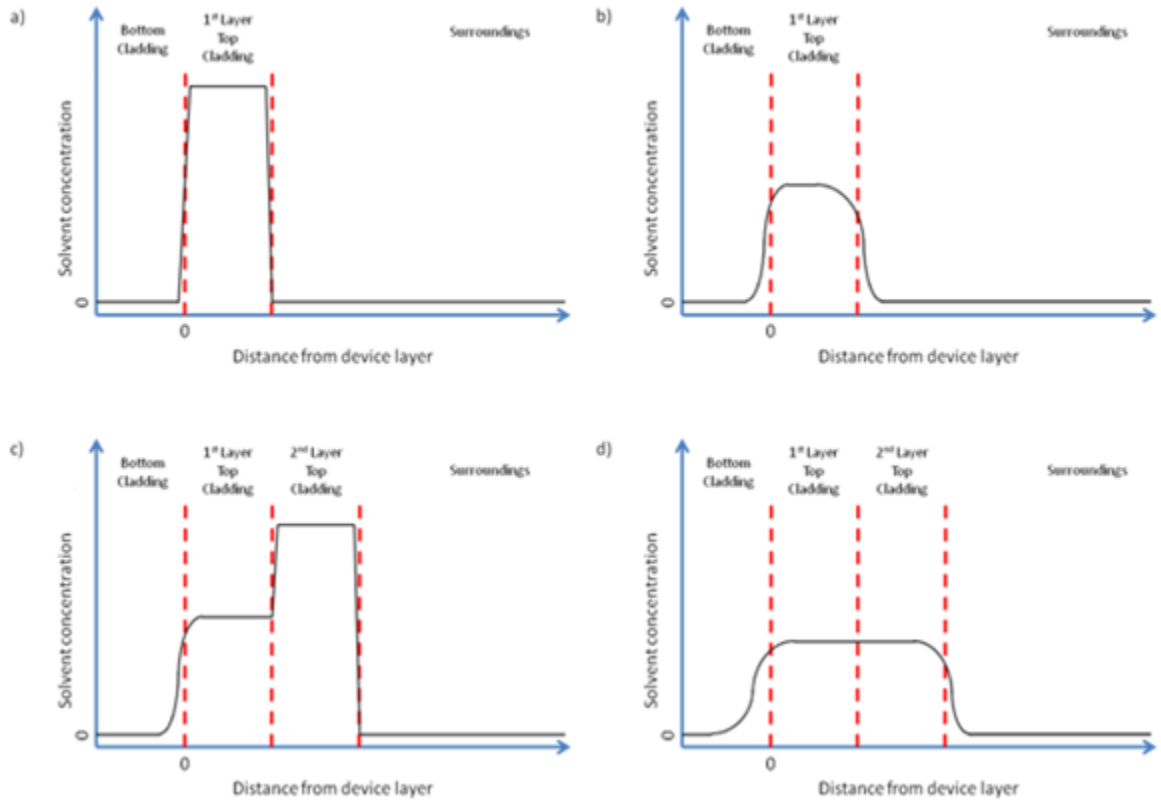

Figure 35: Solvent concentration profiles in CYTOP using old top cladding fabrication procedure [6]: a) Immediately after spin coating of 1st layer of upper cladding, b) after baking of 1st layer of upper cladding, c) immediately after spin coating of 2nd layer of upper cladding, d) after baking of 2nd layer of upper cladding.

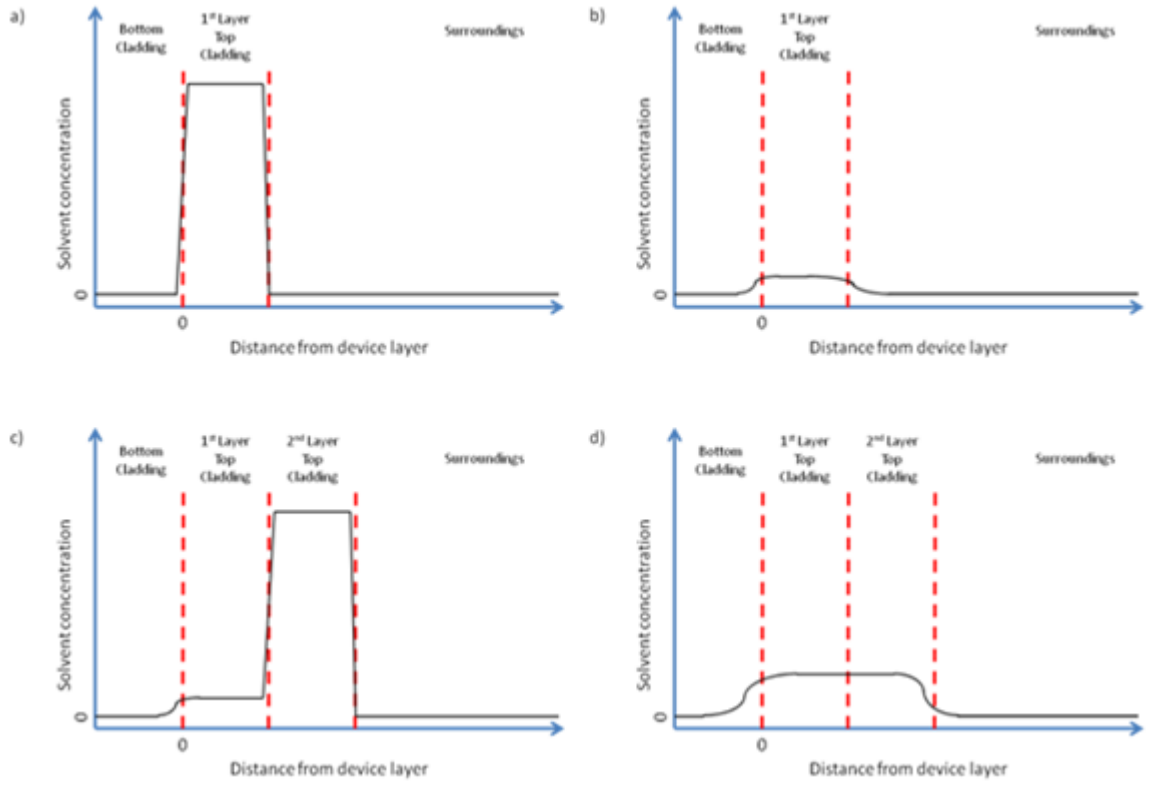

Figure 36: Solvent concentration profiles in CYTOP using new top cladding fabrication procedure: a) Immediately after spin coating of 1st layer of upper cladding, b) after baking of 1st layer of upper cladding, c) immediately after spin coating of 2nd layer of upper cladding, d) after baking of 2nd layer of upper cladding.

As subsequent layers are deposited, a progression of solvent into the lower cladding is observed resulting in a distinct deformation pattern. The difference in the extent of the deformation between the old [6] and new processes is outlined in Figure 37 a) through f). The contact pads shown in Figure 37 a), c) and e) are taken after baking of the 3rd, 4th and 5th upper cladding layers respectively using the old fabrication procedure [6]. The deformation is indicative of a high solvent content in the CYTOP layers, as would be expected when baked at low temperature. Figure 37 b), d) and f) are also taken after baking of the 3rd, 4th and 5th upper cladding layers, this time using the new fabrication procedure.

The noticeable lack of deformation is due to a significantly lower solvent concentration in the upper cladding, effectively reducing the diffusion rate of solvent into the CYTOP beneath the devices.

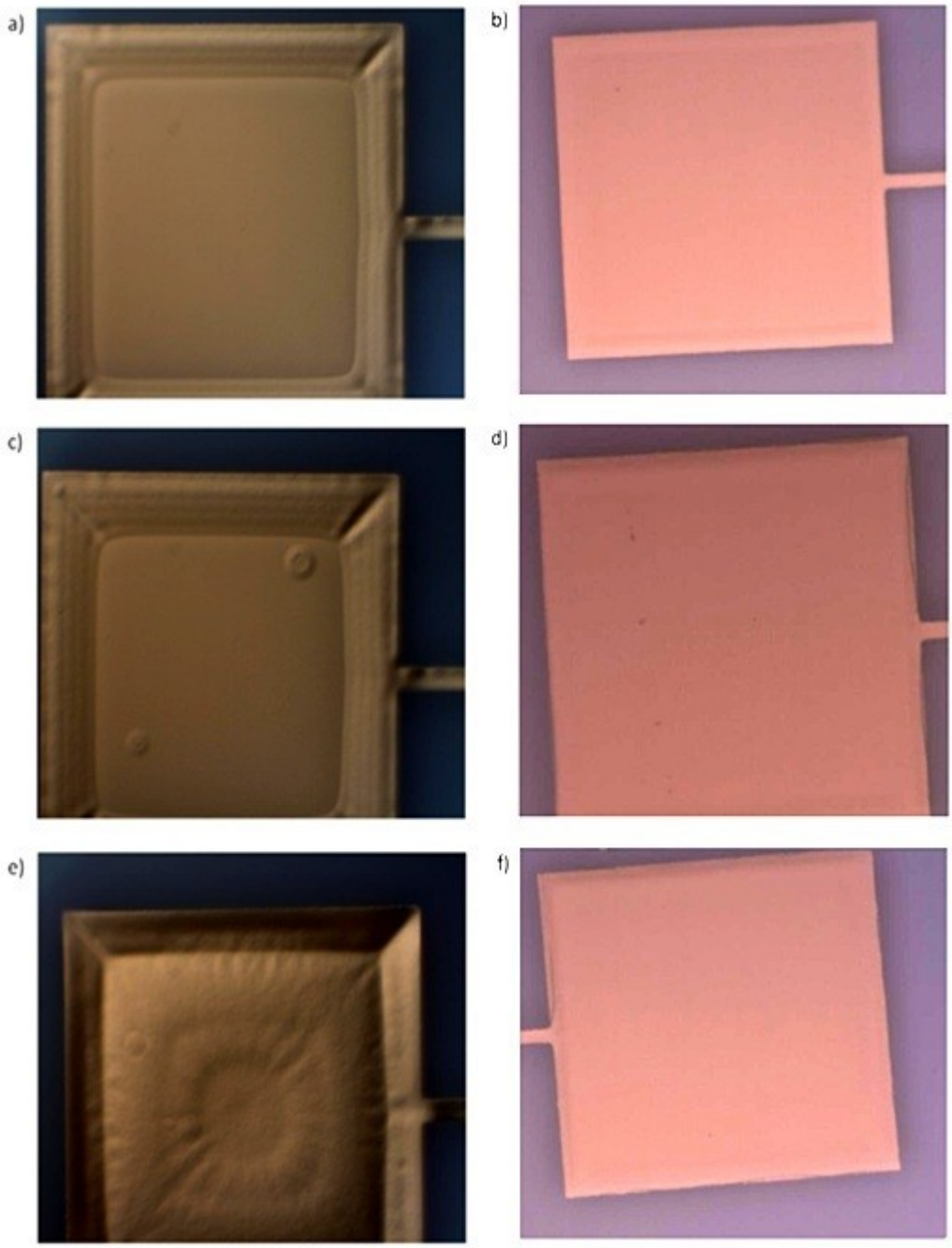

Figure 37: Waveguide deformation comparison: a), b) 3rd layer post-bake, c), d) 4th layer post-bake, e), f) 5th layer post-bake; (a), (c) and (e) old upper cladding process [6]; (b), (d) and (f) new upper-cladding process.

The modified upper cladding procedure does not begin to show signs of deformation until the fifth layer is applied, as shown in Figure 38 below. While it would be

ideal to maintain the devices in their original condition, it is necessary to have a dielectric thickness of approximately 8 µm (to fully contain the SPP waves) and, as a result, some deformation must be tolerated.

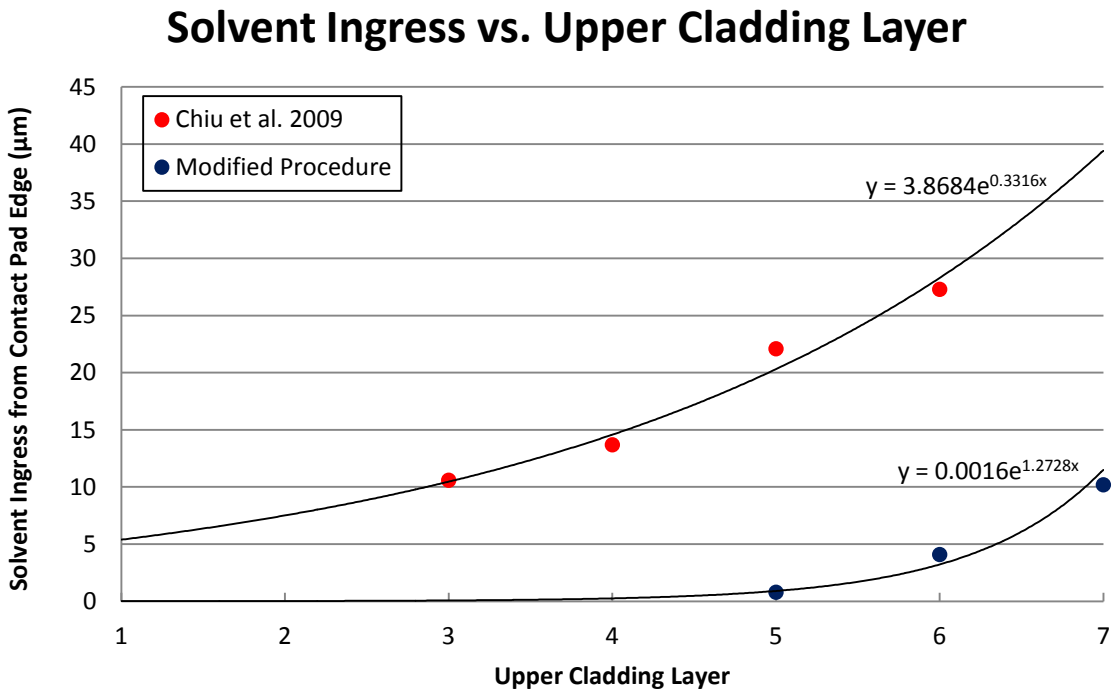

Figure 38: Solvent ingress beneath contact pads as a function of upper cladding layer.

While the contact pads provide a good indication as to the extent of solvent ingress, any deformation occurring in them is relatively harmless in terms of their functionality. More sensitive features such as the Y-Junctions and the thin stripe waveguides must be examined in order to gain insight as to the effect of solvent ingress on device operability.

5. Flow Channels

5.1. Objectives

This chapter outlines the procedure used to define and etch the fluidic channels used to expose the gold waveguide surface to allow for subsequent functionalization for biosensing applications as well as outlining various techniques used to verify the waveguide dimensions and operability. The channel etching process is identical to that described in ***Chiu et. al. 2009***, with a slight difference in the etching procedure to allow for closer monitoring of the timed etching process in order to reduce the degree of ever-etching beyond the waveguide level.

5.2. Channel Lithography

Once the wafers are fully cladded in CYTOP, the fluidic channels must be defined in preparation for etching. This is achieved through a lithographic technique substantially different from that used in defining the gold features. The first step, as in the procedure outlined in Table 4, is an O_2 plasma etch carried out at 100 W, 300 mTorr and 220 sccm of O_2. This is done for 30 seconds in order to "ash" the CYTOP surface and facilitate spin coating of the patterning resist.

The patterning resist used for channel definition is a "MEGAPOSIT SPR 220-7" positive tone photoresist supplied by Microchem. The photoresist is spin coated onto the wafer by first spinning at 500 rpm for 20 seconds to evenly distribute the material over the wafer surface, then by spinning at 2300 rpm for 30 seconds to achieve the desired thickness

of approximately 9 µm [21]. Following spinning, the wafer is baked on a direct contact hotplate in a three step process to avoid thermal shock or formation of bubbles in the photoresist surface. The wafer is first baked at 50 °C for 1 minute followed by 75 °C for 1 minute and finally at 100 °C for 3 minutes. Since it is not desired to cool the wafer between each baking step and the hotplates are not able to immediately change temperature, three hot plates are needed for the execution of this procedure. The wafer is then gradually cooled down by placing it back on the 75 °C hotplate for 1 minute, then on the 50 °C hotplate for an additional 1 minute. Once the photoresist layer is fully cured, it is placed in the Karl Suss MA6 mask aligner along with the desired fluidics photo-mask for alignment and exposure. The alignment at this level is far more critical than the alignment at the device level, because precise alignment of the flow channels over the devices is essential.

The exposure time required is 95 seconds (corresponding to 800 - 1350 mJ/cm^2 at the lamp intensity given in Table 6) followed by a minimum 2 hour delay before the post exposure bake to allow for rehydration of the film. Due to the 100 °C baking temperature, little or no water is left in the polymer layer after curing. Since water is necessary for the photoreaction to proceed, a sufficient amount of time must be allowed for diffusion back into the film. A minimum of two hours is prescribed in [6], although best results are obtained when the wafer is allowed to rehydrate over night.

Following the rehydration step, a post-exposure bake is required to complete the photoreaction. This is carried out using the same baking procedure explained above: 1 minute at 50 °C, 1 minute at 75 °C, 3 minutes at 100 °C, 1 minute at 75 °C and finally 1

minute at 50 °C. This is again to avoid thermal stress within the film which may lead to cracking. Once the photoresist has been deposited, exposed and fully cured, the exposed portions must be removed by immersion in MICROPOSIT MF 24A developer solution. Development takes approximately 2 minutes with high agitation, although this time can be extended indefinitely since no lift-off layer is used and over-development is of little concern. The full procedure is outlined below in Table 12 and in Figure 39.

Table 12: Fluidic channel photoresist spin coating and lithography procedure.

Process Step	Description
Ashing	Wafer surface is primed in O_2 plasma environment for 30 seconds at 100 W, 300 mTorr and 220 sccm of O_2
Spin Coating	Spin SPR 220-7 at 500 rpm for 20 seconds followed 2300 rpm for 30 seconds
1st Bake	Bake on direct contact hotplate for 1 minute at 50 °C
2nd Bake	Bake on direct contact hotplate for 1 minute at 75 °C
3rd Bake	Bake on direct contact hotplate for 3 minute at 100 °C
4th Bake	Bake on direct contact hotplate for 1 minute at 75 °C
5th Bake	Bake on direct contact hotplate for 1 minute at 50 °C
Exposure	95 seconds in Karl Suss MA6 Mask aligner (800 - 1350 mJ/cm^2)
Rehydration Delay	Wafer held at ambient conditions for minimum of 2 hours
Post-Exposure Bake	Repeat 1st - 5th Baking Steps
Development	Immerse in MF 24A for 2 minutes with high agitation then rinse with DI water

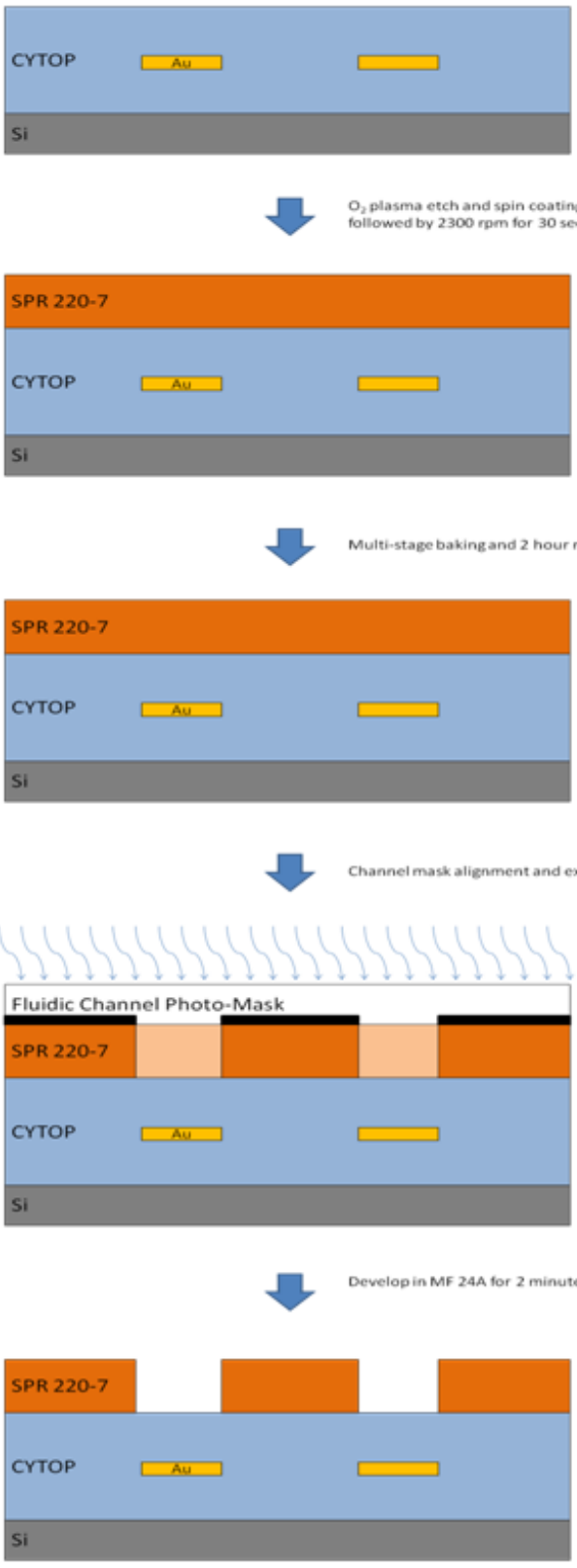
CYTOP
Au
Si
O_2 plasma etch and spin coating of SPR 220-7 at 1000 rpm for 20 seconds followed by 2300 rpm for 30 seconds (~ 9 µm)
SPR 220-7
CYTOP
Au
Si
Multi-stage baking and 2 hour rehydration time
SPR 220-7
CYTOP
Au
Si
Channel mask alignment and exposure with Karl Suss MA^ mask aligner
Fluidic Channel Photo-Mask
SPR 220-7
CYTOP
Au
Si
Develop in MF 24A for 2 minutes with vigorous agitation
SPR 220-7
CYTOP
Au
Si

Figure 39: Fluidic channel lithographic process flow diagram.

5.3. Channel Etching

The operability of these devices is reliant on surface interactions between a metallic (gold) structure and a semi-infinite dielectric (sensing solution). For biosensing to be possible, the gold surface must be exposed to allow for the sensing medium to come into contact with it. This is achieved through a high powered reactive ion etch, in this case, using an O_2 plasma. Channel etching is performed using a March Systems Jupiter II bench top plasma etching system. This is an anisotropic (directional) etch such that the channel side walls maintain a perpendicular profile to the wafer surface.

Table 13: Channel etching system specifications.

Make and Model	March Systems Jupiter II Plasma Etcher
Power (W)	200
Pressure (mTorr)	300
O_2 flow (sccm)	100
Avg. Total Etch Time (min)	9

An approximate etch rate for CYTOP in an O_2 plasma environment was determined in [6] at the conditions prescribed in Table 13. Etch rate tests were performed to determine average etch depth as a function of exposure time to O_2 plasma; this resulted in an etch rate of 0.918 ± 0.017 µm/min.

For an upper cladding thickness of approximately 8 μm and the etch rate given above, this yields an etch time of 8.5 to 9 minutes. As mentioned in section 1.3, a small over etch is required to ensure that the gold is fully exposed. For this reason, the required etch time tends towards the 9 minute mark. This will typically yield an over etch of approximately 500 nm below the device level, shown in the AFM scans of Figure 40 a) and b).

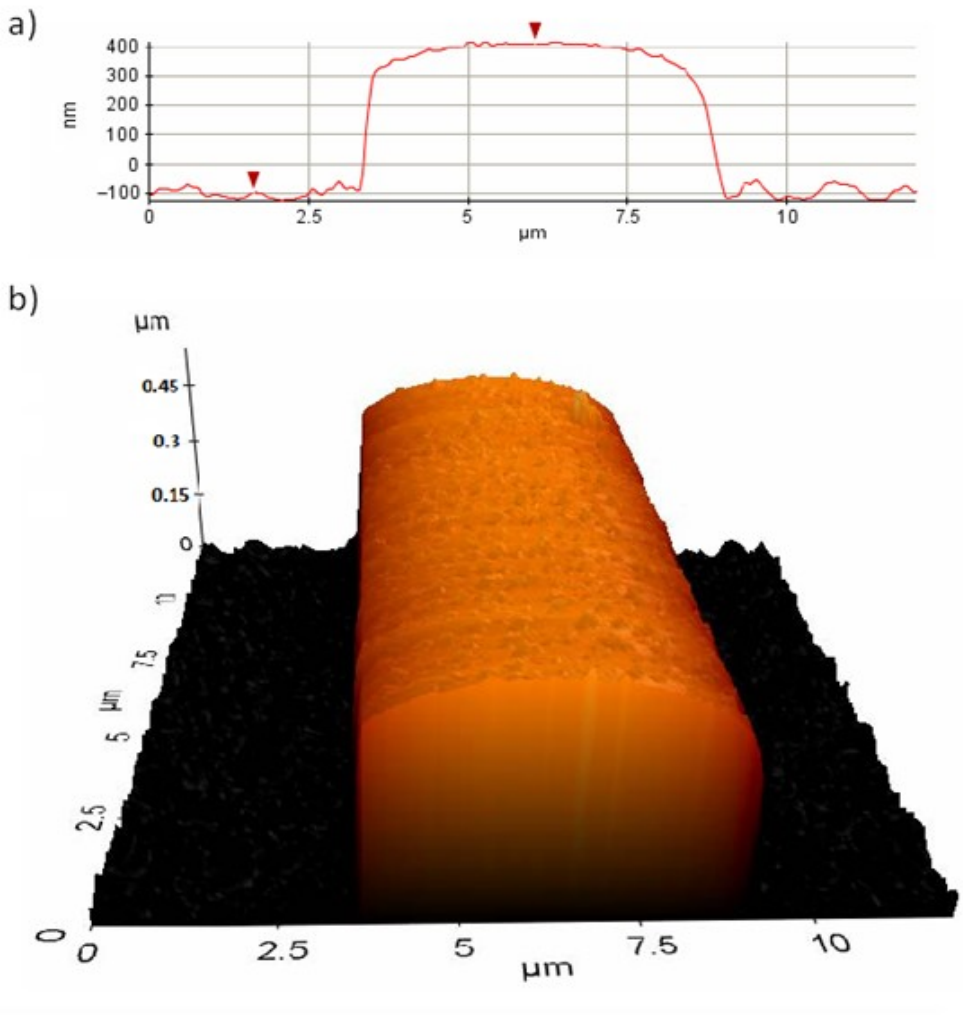

Figure 40: AFM scan of over-etch on straight waveguide in fluidic channel, a) line profile, b) 3D representation.

While the average total etch time is specified at 9 minutes in Table 13 resulting in an over-etch with a typical depth of 500 nm, with careful timing and periodic profile checks performed throughout the etching process, it is has been observed in some cases to be able to reduced as low as low as 120 nm. Based on the given etch rate of 0.918 µm per minute, this leaves a window of as little as 10 seconds of etching beyond the lower surface of the

gold structures. In order to minimize the over-etch, profile checks are performed after 5 minutes, 7 minutes, 8 minutes and every 30 seconds afterwards until all devices on the wafer are fully exposed. Typically, devices located near the outermost edge of the wafer have a slightly thinner upper cladding than devices near the centre of the wafer (approximately 300 to 400 nm difference), and as such will have a greater over-etch depth. Profilometry checks are performed at five points on each wafer to ensure that all devices have been fully exposed after etching of the fluidic channels: one in the centre and four, equally distributed, around the outer perimeter of the wafer. The profilometry verification pattern is shown, schematically, in Figure 41.

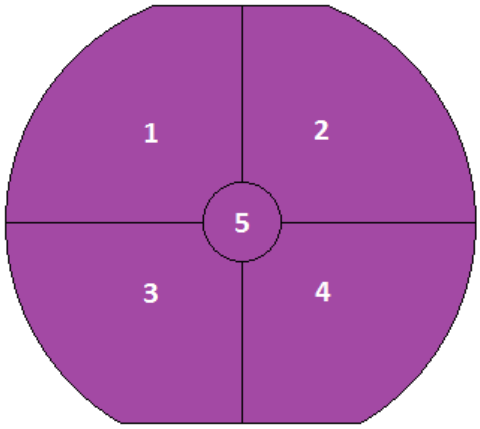

Figure 41: Profilometry verification pattern for over-etch and device exposure measurements.

Minimization of the over-etch depth improves the quality of the devices as noted in [6]. It has been observed in instances where the over-etch depth is excessively deep that air pockets would form in the corners between the bottom of the fluidic channel and the side

wall of the elevated devices, as shown in Figure 42. Due to the close proximity of the air bubbles to the waveguide structure and the large difference in refractive index from air to the sensing medium, very high attenuation may result.

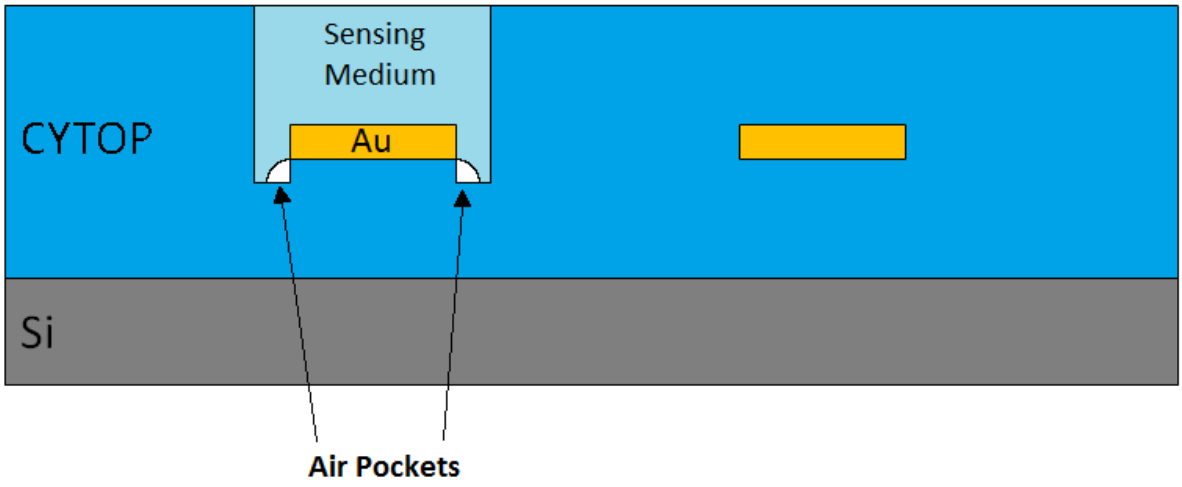

Figure 42: Potential formation of air pockets in fluidic channels. Adapted from [6].

After the etch depth is verified, and all devices fully exposed, the remaining photoresist is stripped away in a three stage washing process. First acetone is used to remove the photoresist, then isopropanol is used to remove the acetone residue and finally de-ionized water is used to remove the isopropanol. The full etching and verification procedure is described in Table 14 and shown schematically in Figure 43.

Table 14: Channel etching fabrication and verification procedure.

Process Step	Description
1st Etch	Etch wafer in O_2 plasma for 5 min at 200 W, 300 mTorr and 100

	sccm O_2
Profilometry Scan	Channel depth and waveguide exposure checked with Dektak IIA Profilometer
2nd Etch	Etch wafer in O_2 plasma for 2 min at 200 W, 300 mTorr and 100 sccm O_2
Profilometry Scan	Channel depth and waveguide exposure checked with Dektak IIA Profilometer
3rd Etch	Etch wafer in O_2 plasma for 1 min at 200 W, 300 mTorr and 100 sccm O_2
Profilometry Scan	Channel depth and waveguide exposure checked with Dektak IIA Profilometer
4th Etch	Etch wafer in O_2 plasma for 30 seconds at 200 W, 300 mTorr and 100 sccm O_2
Profilometry Scan	Channel depth and waveguide exposure checked with Dektak IIA Profilometer
5th Etch	Etch wafer in O_2 plasma for 30 seconds at 200 W, 300 mTorr and 100 sccm O_2
Repetition	Repeat previous 2 steps as needed until all devices on wafer are fully exposed
Cleaning	Wafer cleaned in Acetone/Isopropanol/De-ionized water to remove photoresist and clean channels of etchant residue

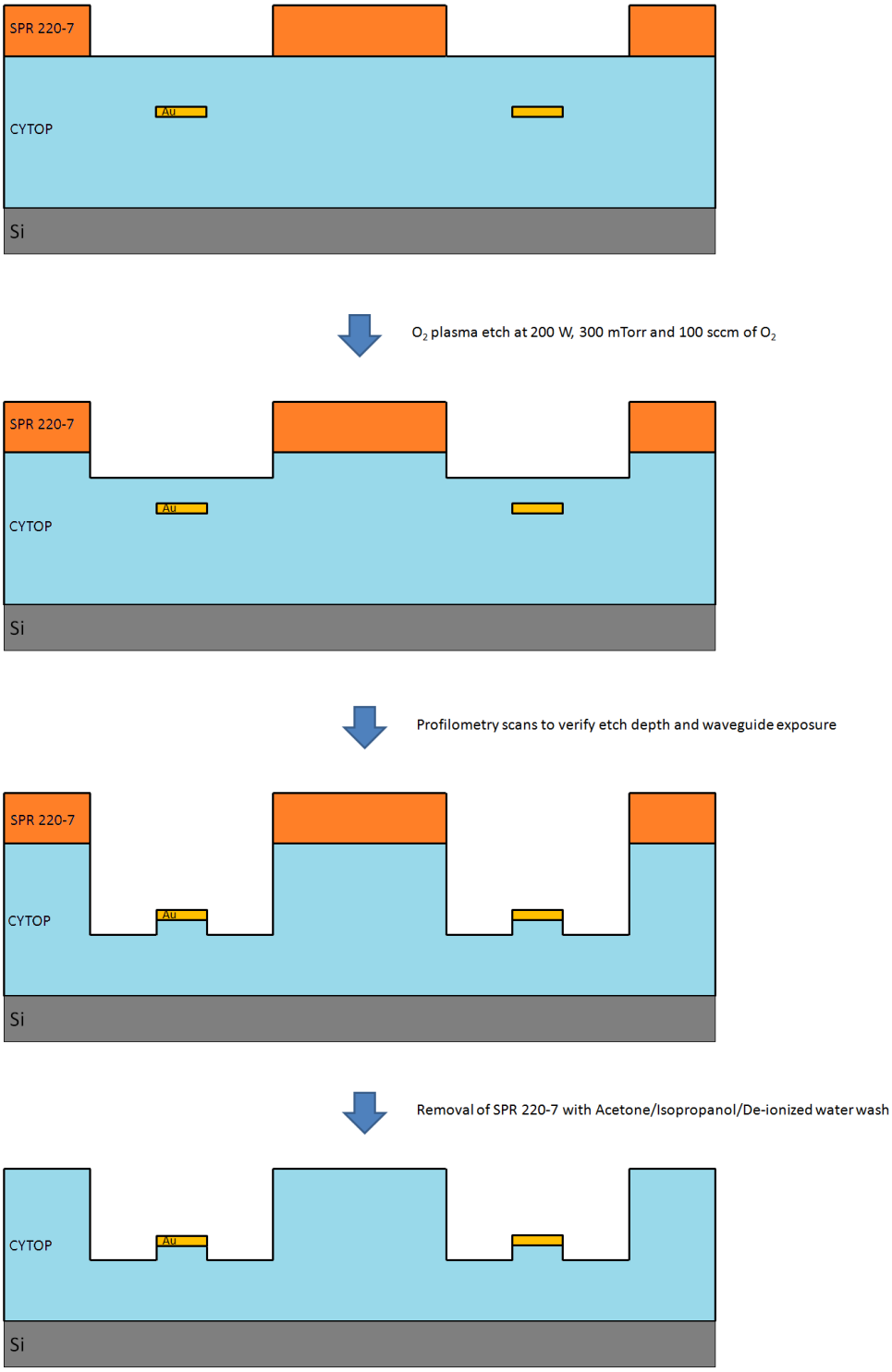

Figure 43: Process flow diagram for fluidic channel etching.

Another aspect of importance is the roughness of the etched CYTOP within the fluidic channels. Roughness is likely to produce a larger pressure drop as the sensing fluid is pumped through the channel and to introduce turbulence near the sensing surface which would influence measured binding kinetics. The former would create difficulties for bonded devices, discussed in Appendix B, since a higher inlet pressure would be required and may pose a risk of leakage at the bonded interface.

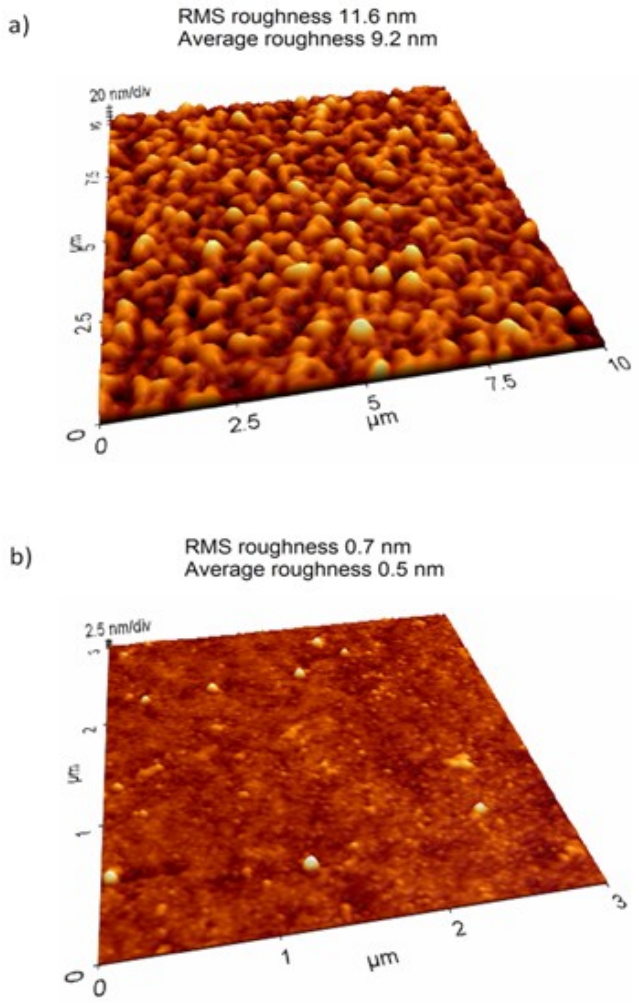

Figure 44: CYTOP surface roughness: a) etched CYTOP, b) un-etched CYTOP.

The degree to which the surface roughness inside the fluidic channels will impact the device operability will need to be investigated more closely. Furthermore, whether or not this is a variable which may be manipulated by modifying the etch process still needs to be determined. The difference in roughness between an etched CYTOP surface and an un-etched CYTOP surface is shown above in Figure 44 a) and b) respectively. A significant amount of variation has also been observed between different wafers processed under the same conditions. In some cases an average surface roughness of 32.2 nm, shown in Figure 45 , more than three times that of the etched surface in Figure 44 a) has been observed. The cause of this variation is not yet fully understood and warrants closer inspection in future fabrication runs.

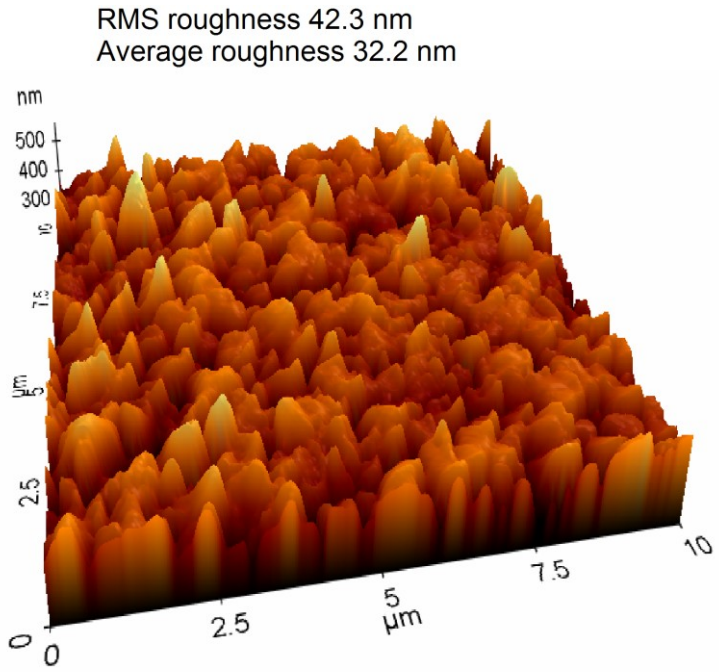

Figure 45: Etched CYTOP surface showing excessive surface roughness.

5.4. Device Characterization (Physical)

Once the flow channels are fully etched and the devices have been properly cleaned, the wafer is coated in a protective film and sent out for dicing. The protective film used in this case is a thick layer of SPR 220-7, applied in a similar manner to that explained in Table 12. The photoresist is spun initially at 1000 rpm for 20 seconds followed by 2300 rpm for 30 seconds. Baking of the protective layer is executed in a single step carried out at 105 °C for 3 minutes, because cracking of the photoresist is of little consequence to the devices; *i.e.,* there is no need for a multi-stage baking process as used in the definition of the fluidic channels to avoid thermal stress. Care must be taken, however, in ensuring that the film is cured hard enough such that the photoresist is diced cleanly and not smeared into the CYTOP at the optical facets (yet soft enough to not chip as the dicing saw cuts through the wafer). This can be seen in Figure 46 a), in which the diced facet shows signs of contamination from the photoresist. Conversely, Figure 46 b) shows a diced facet in which the photoresist was cured properly resulting in a contaminant free facet.

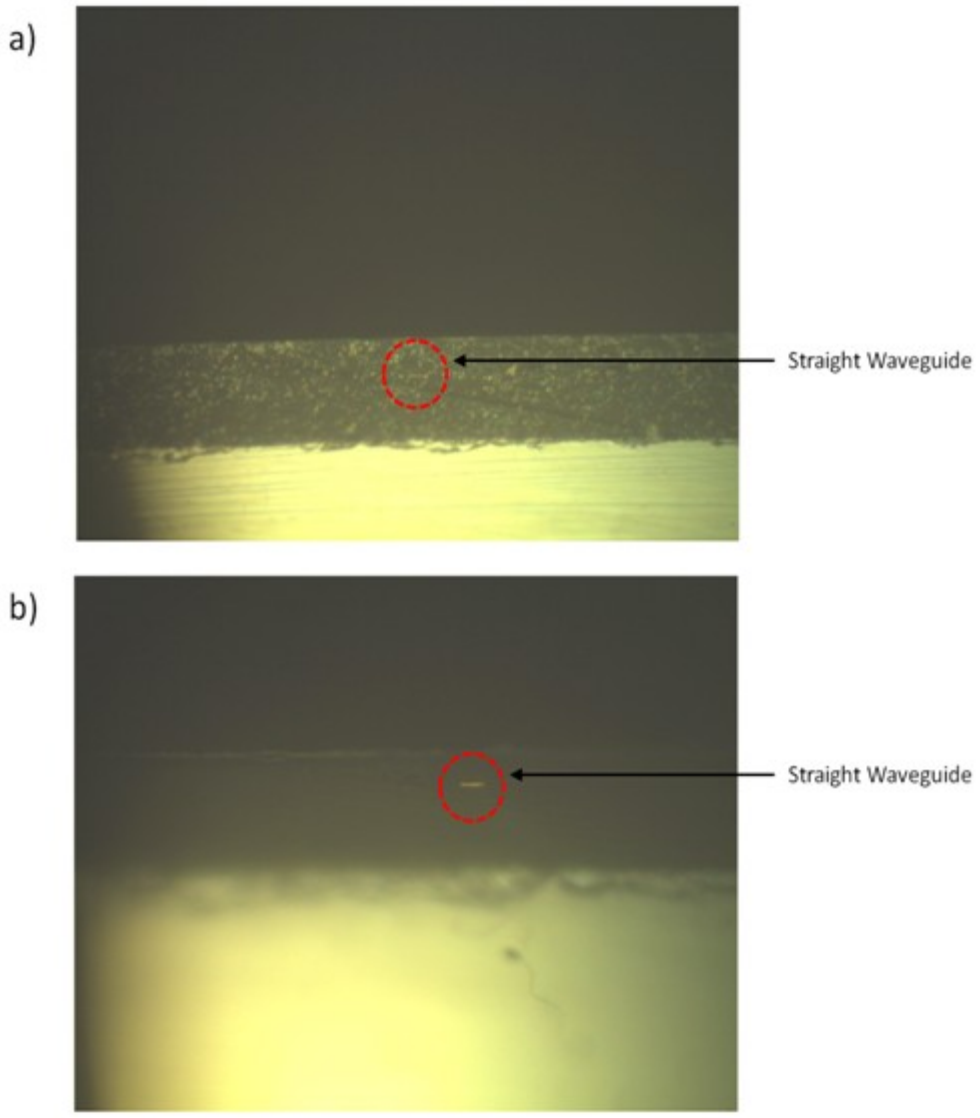

Figure 46: Diced facets showing: a) SPR 220-7 contamination on CYTOP, b) clean facet with no signs of contamination.

Once the dies are returned from dicing they are cleaned in a high temperature (80 °C) bath of Microposit 1165 remover, followed by rinsing in isopropanol, and finally dried under a high purity nitrogen jet. Samples are then selected for AFM scans to check

deformation of waveguides, over-etch depth, gold thickness and channel depth. The remainder of the dies are kept for optical characterization and biosensing experiments.

First discussed is the physical characterization of the devices and fluidic channels, beginning with the channel and device dimension verification, the most critical of these aspects being the waveguide width and thickness. The AFM scans, shown below in Figure 47 a) and b), illustrate both the width of the device and the degree of deformation based on the top cladding formation procedure used. As can be seen, both devices are close to the 5 µm target for width, the main difference being in the level of deformation. Using the new top cladding process reduces the "bowing" effect of the straight waveguides by a factor of 2.5 times from that seen when using the old top cladding application procedure outlined in [6]. Furthermore, a substantial reduction in the over etch is noted as a result of more frequent profilometry checks during the channel etching process. It should also be note that the extent of solvent ingress beneath the contact pads as a function of the upper cladding layer showed the process described in [6] was found to be approximately 2.7 times larger than the modified procedure described within this thesis.

The next dimension to be verified is the thickness of the gold film. In order to measure the film thickness, a portion of the waveguide was delaminated from the CYTOP by immersion in an ultrasonic bath. By measuring the difference in height between the top of the CYTOP pillar and the residual gold surface (schematic shown below in Figure 48), the gold thickness may be measured. Care must be taken such that the proximity of the

measured points is as close as possible to avoid any error which may result due to waveguide deformation seen above.

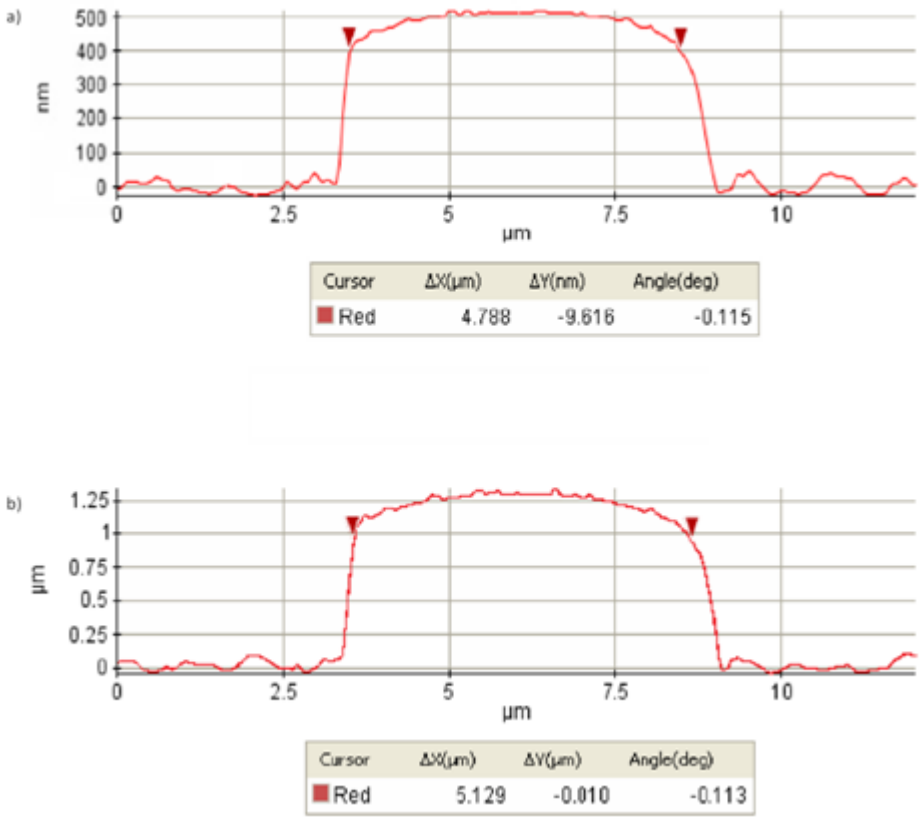

Figure 47: AFM scan showing straight waveguide width: a) using new top cladding process, b) using old top cladding process [6].

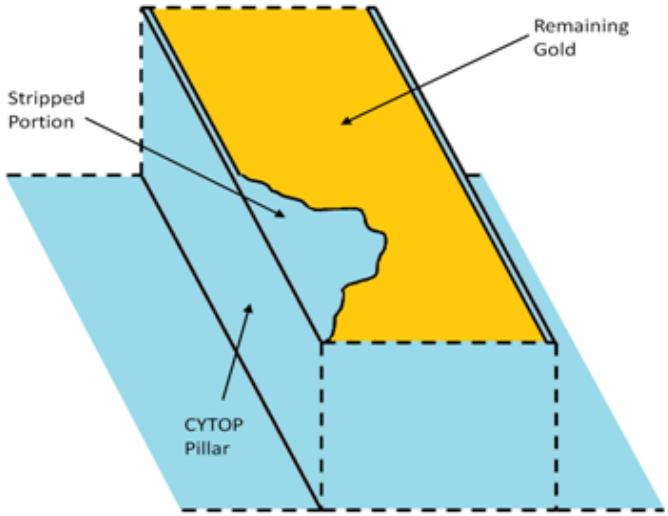

Figure 48: Schematic of gold thickness measurement technique.

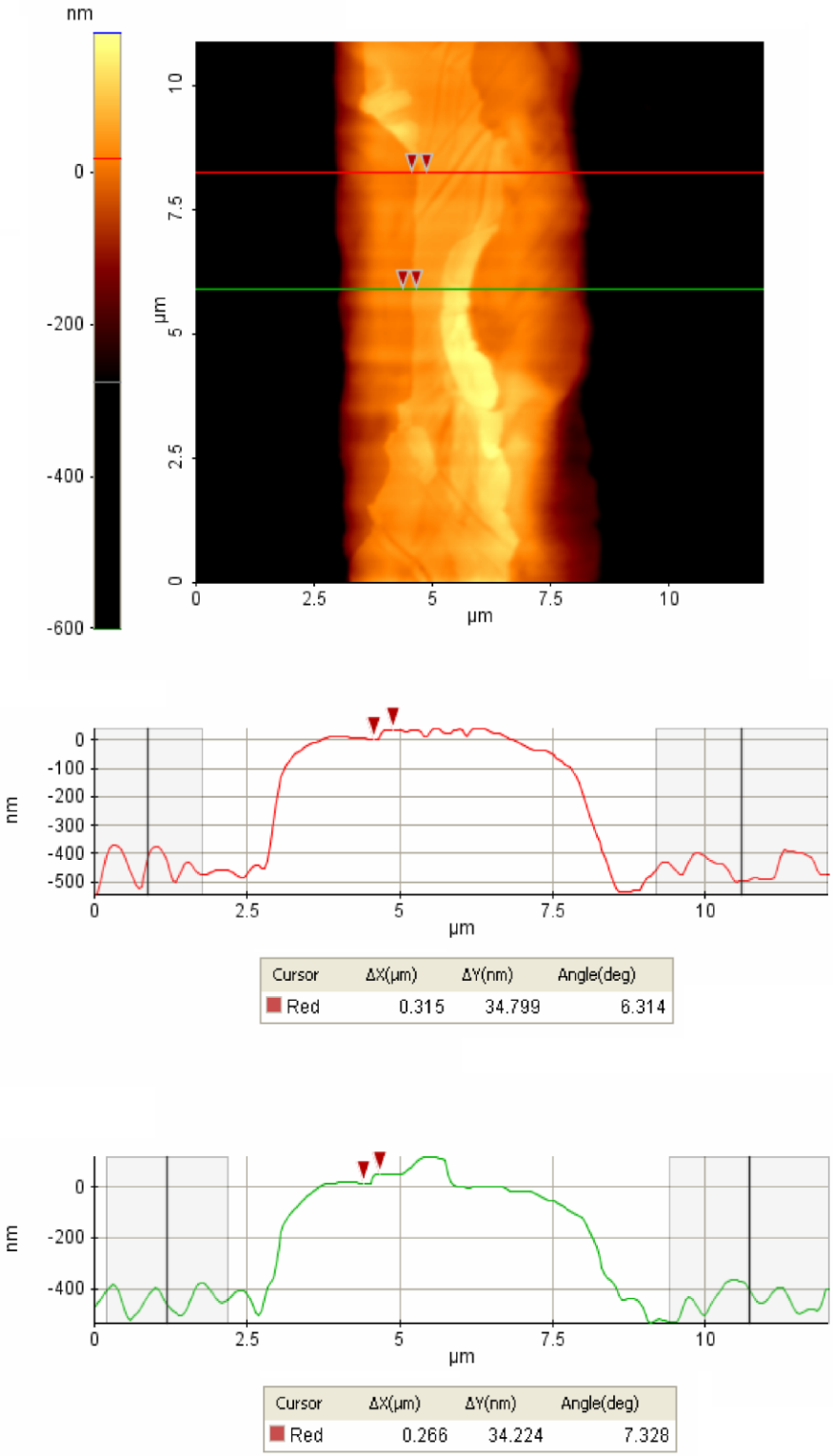

Figure 49: AFM line profiles for gold thickness verification.

Figure 49, above, shows the line profile of a partially delaminated device. The gold thickness is found to be between 34 and 35 nm, as is expected according to the gold deposition procedure outlined in Chapter 3.

The final physical dimension that must be measured is the depth of the etched channel. By subtracting the over-etch depth from this value, an estimate of the cladding thickness above the waveguides may be obtained. Since a minimum thickness of approximately 7 μm of dielectric (CYTOP or index matched sensing fluid) is needed both above and below the device structures, this is a vital measurement for proper device verification. This measurement may be taken by means of profilometry or AFM, of which AFM is by far the most accurate. Figure 50, below, shows a line profile taken by AFM, indicating both the depth of the channel and the shape of the side wall. While the channel depth is sufficient, there are issues with topographic variations and the shape of the etch profile, which will hinder the bonding process needed to encapsulate the waveguide and fluidic channels beneath a glass lid. This is due to the need for the glass wafer to come into intimate contact with the top of the upper cladding surface, and as such, any imperfections in the upper cladding surface reduce the overall contact area needed to achieve a sufficient bond (procedure outlined in Appendix B).

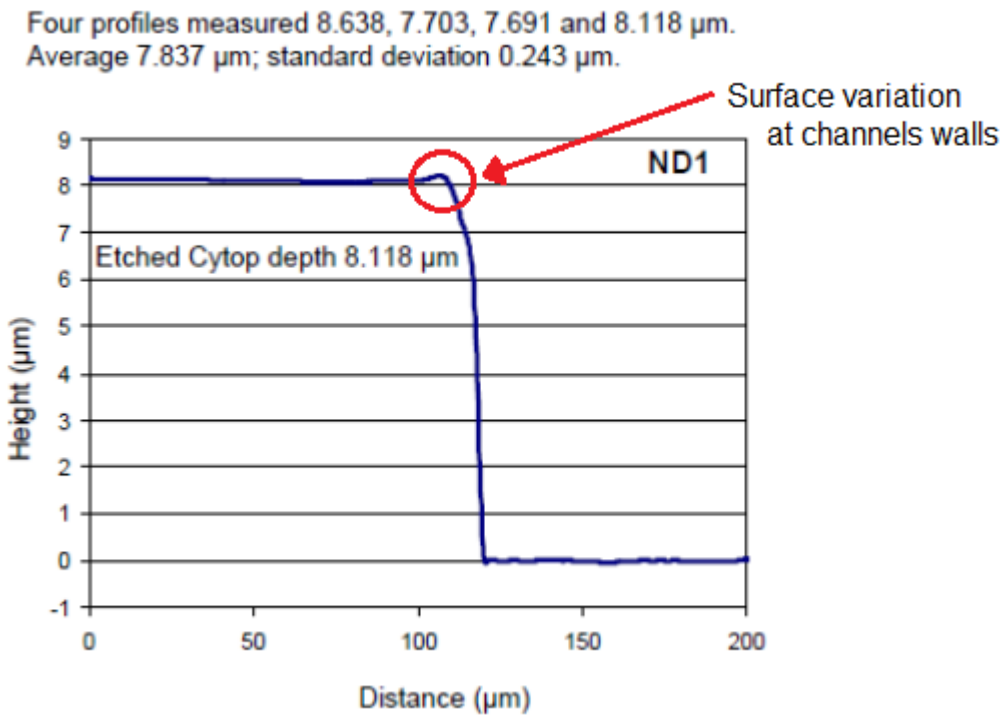

Figure 50: Fluidic channel depth showing standard deviation and side wall profile.

5.5. Device Characterization (Optical)

The devices described in this thesis are verified optically by measuring the power output of waveguides and comparing the experimental values to the expected values, determined theoretically. The attenuation, or power lost per unit length of the waveguide, is determined by measuring the total power output for various lengths of waveguides, in this case 3 mm, 3.8 mm and 4.8 mm long. A plot of power loss as a function of device length is generated from the results, the slope of which yields the attenuation value in dB/mm while the y-axis intercept yields the total coupling losses which is subsequently divided by 2 giving the coupling loss per facet (input and output) in dB.

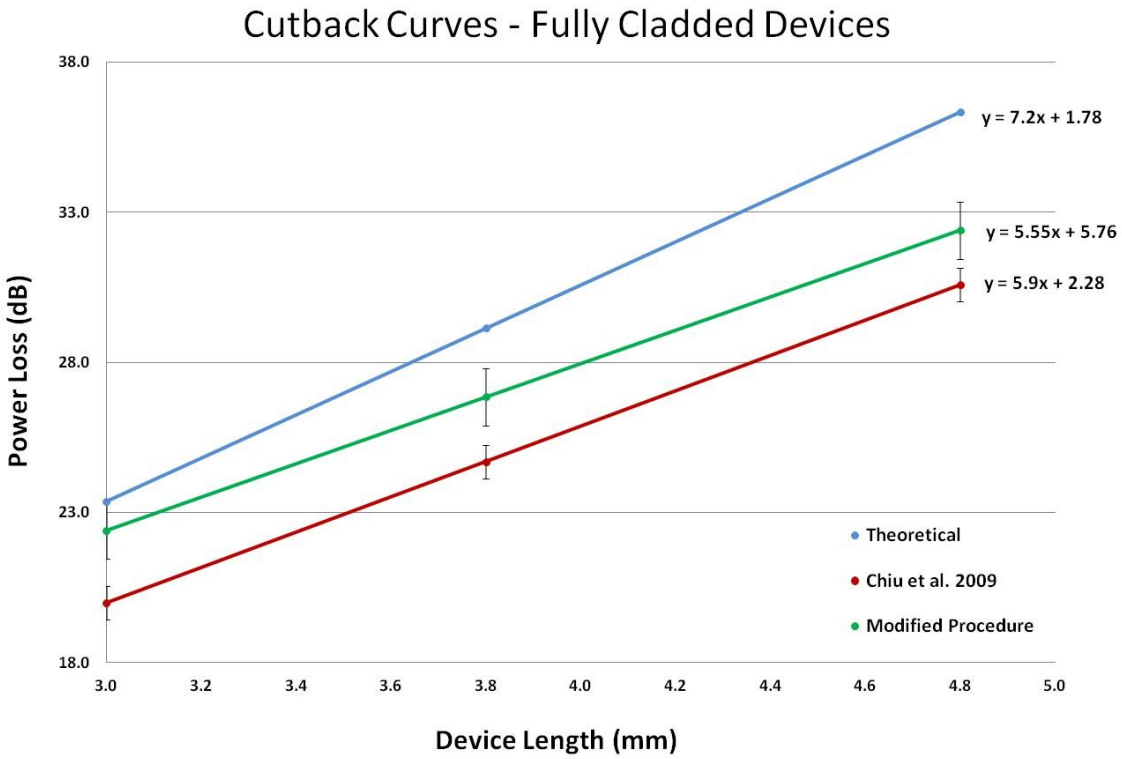

Figure 51: Cutback curve comparing devices fabricated with old process and new process to theoretical values. Error bars not accounting for variation in insertion losses

Table 15: Attenuation and coupling loss values of devices compared to theoretical values.

Variable	Fabrication Procedure		
	Theoretical Value	Old Fabrication Process	New Fabrication Process
Attenuation (dB/mm)	7.2	5.9 ± 0.56 (5.34 to 6.46)	5.6 ± 0.95 (4.59 to 6.51)
Coupling Loss per Facet (dB)	0.89	0.57 ± 0.73 (-0.16 to 1.30)	2.88 ± 0.96 (1.93 to 3.83)

* Deviation values based on 95% confidence interval

Figure 51 and Table 15, above, show the results of the optical characterization of devices fabricated using the new procedure outlined in this thesis versus devices fabricated using the old procedure outlined in [6] (measurements obtained by Asad Khan, M.A.Sc. candidate, University of Ottawa and Hui Fan, Ph.D. candidate, Univeristy of Ottawa). Both sets of data are then compared to theoretical values calculated using COMSOL software [6]. As the above data indicates, both fabrication procedures yield lower attenuation values than the theoretical model predicted, with the lowest value belonging to the new fabrication procedure. This is presumably due to the combination of eliminating "spits" on the gold surface and reducing the overall degree of deformation in the waveguides. Furthermore, it is believed that the lower than expected attenuation values are a result of thinning of the waveguides [24] due to the “bowing” effect previously described. Since the waveguides are of fixed volume and the straight line distance from one edge to the other remains fixed at 5 μm, the waveguide thickness must decrease in order to accommodate the change in shape.

The coupling loss per facet for devices fabricated using the new procedure was observed to be slightly higher than that of the theoretical value; however, this is believed to be a result of insufficient cleaning prior to testing. Coupling losses are also strongly dependant on the diced facet quality and alignment of the fiber-optic cable to the waveguide. These factors, in conjunction with the limited number of tested samples, make coupling loss measurement highly sensitive to human error and as such would require more careful testing in order to properly verify the value reported in Table 15. This would also

explain the large standard deviation observed in both attenuation and coupling loss measurements.

After optical characterization, the devices are tested in order to verify biosensing capability. Two different tests were executed in order to check sensor functionality: detection of Bovine Serum Albumin (BSA) and selective differentiation of red blood cells (RBC's) (measurements were obtained by Alex Krupin, Ph.D. candidate, University of Ottawa).

Figure 52 shows a binding curve of BSA on a 16-MHA self assembled monolayer vs that of BSA on poly-ethylene glycol (PEG). 16-MHA has a chemical formula of $HSCH_2(CH_2)_{13}CH_2COOH$, this enables the thiol end group to bind to the gold surface leaving the carboxylic acid end group for BSA immobilization, conversely, PEG has a chemical formula of $HOCH_2(CH_2OCH_2)_nCH_2OH$ and is a known agent for blocking of protein binding [23]. After functionalization of the sensor surface is completed, a buffer solution of phosphate buffered saline (PBS) and glycerol (Gly) is injected into the flow channels at a rate of 20 µL/min and a concentration of 7.25 wt% glycerol. The precise glycerol concentration is important in order to closely match the refractive index of CYTOP (PBS/Gly n=1.3302, CYTOP n = 1.3385). It has been determined experimentally that having the refractive index of the fluid in the channel slightly below that of CYTOP yields the best results [7]. This solution is passed through the fluidic channels for several minutes in order to get a baseline reading of the power output. Once the baseline is determined, a solution 100 µg/mL of BSA in the PBS/Gly buffer is then pumped through the channels at the same

flow rate (20 µL/min). As the BSA is immobilized on the waveguide surface (due to the 16-MHA SAM), a shift in the output power can be observed. As the curve levels off, the fluid passing through the channel is switched back to the original PBS/Gly buffer solution triggering a very small decrease in signal power due to a change in the refractive index of the fluid. Since the signal power does not change appreciably after removing BSA from the sensing medium, it is evident that successful immobilization of the targeted analyte has occurred. When compared to a similar binding curve generated with a PEG functionalized surface (figure 53), the change in power is substantially smaller. Some adsorption is observed due to the small size of PEG [22], however this is substantially less than that seen on a 16-MHA functionalized surface, indicating that protein adsorption was successfully inhibited with the use of PEG on the gold surface.

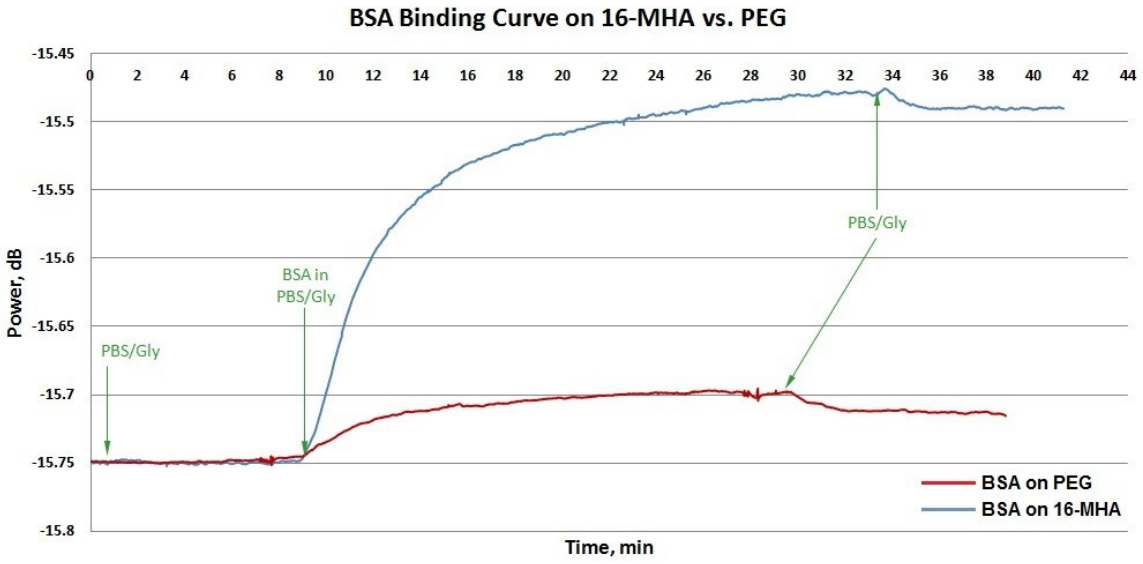

Figure 52: Binding curve for BSA on 16-MHA vs. PEG. Adapted from [22].

Figure 53 shows the application of the fabricated structures in the differentiation of type A red blood cells (a-RBC's) from type O red blood cells (o-RBC's). In this case, the purpose of the test was to show selective capture of a specific analyte, namely a-RBC's. The sensor surface is functionalized with Anti-A-IgG antibodies; this is done first by incubation in 16-MHA for 2 to 24 hours, followed by a 1 hour incubation in a PBS solution containing 1 mg/mL antibodies, a more detailed description of the functionalization procedure is explained in [7]. Initially the same PBS/Gly buffer solution used in BSA sensing is passed through the fluidic channels, this time at a rate of 65 µL/min to establish the baseline signal (*inset a*). At 7 minutes, the waveguide was exposed to a PBS/Gly buffer solution containing 5×10^7 cells/mL of o-RBC's under static conditions (no flow) for a period of 5 minutes. During this time, there is a substantial decrease in signal power (*inset b*) due to settling of cells on the waveguide surface. Once five minutes have passed, the PBS/Gly buffer solution is pumped through the channels once again to flush out the o-RBC's and return to the baseline signal (*inset c*). The rapid return of the signal power to the baseline indicates that no binding of the o-RBC's occurred on the Anti-A-IgG functionalized surface. The channels are flushed with the buffer solution for 9 minutes to ensure all o-RBC's are removed. At the 24 minute mark, a solution of PBS/Gly buffer containing 5×10^7 cells/mL of a-RBC's is allowed to contact the sensing surface under static conditions for a period of 5 minutes, again resulting in a substantial decrease of signal strength (*inset d*). At the end of the five minutes, the channel is again flushed with PBS/Gly buffer solution, this time the signal power does not return to the baseline (*inset e*) indicating successful, selective

immobilization of a-RBC's. Flushing of the channel lasts 8 minutes with no change in the signal power, after which, de-ionized water is pumped in at a rate of 65 µL/min. This restores the signal strength partially (*inset f*) as a result of cell rupture but is unable to return to the baseline power due to a mismatch in the refractive index between water and CYTOP. Finally, at the 44 minute mark, the channel is again flushed with the PBS/Gly buffer solution resulting in full restoration of the signal strength (*inset g*).

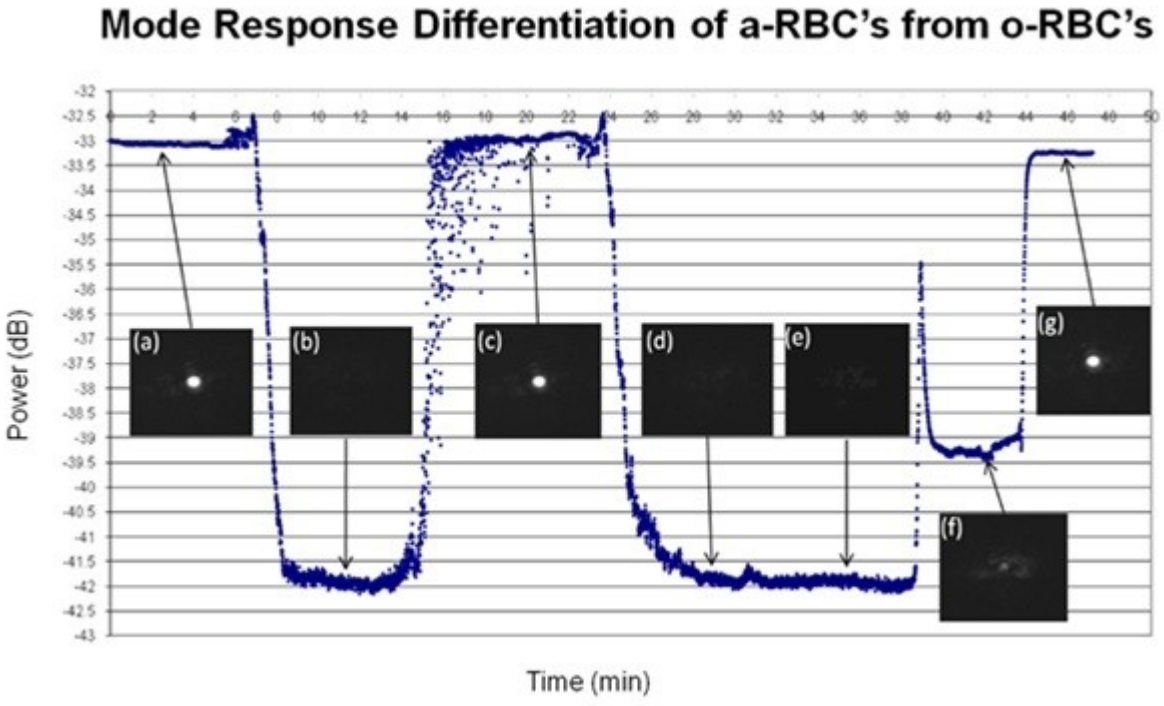

Figure 53: Power output graph for differentiation of type O and type A red blood cells. Adapted from [7].

6. Conclusions, Contributions and Future Work

The described works are an extension of the research carried out in ***Chiu et al. 2009*** [6]. The contributions made in this thesis include improvement of waveguide feature definition through material substitution in the bi-layer lithography procedure, elimination of aberrations and reduction of roughness on waveguide surface through modification of the gold deposition process and reduction in the degree of deformation of waveguides by reduction of solvent in the upper cladding through increased baking temperatures.

The combined effect of these three changes led to significantly improved devices whcih produced a lower background radiation and a reduction in the attenuation values of the propagating waves. Theoretical values obtained by simulations performed in ***Daviau et. al. 2010*** [24], yielded an average attenuation value of 7.2 dB/mm for a 5 μm wide, 35 nm thick gold waveguide embedded in CYTOP. Devices fabricated from the procedure outlined in ***Chiu et. al 2009*** [6] yielded an average attenuation value of 5.9 dB/mm, compared to an average attenuation value of 5.55 dB/mm for the devices fabricated using the process described in this thesis. 95 % confidence intervals were calculated for both sets of devices and were found to be in the ranges of (5.34 dB/mm to 6.46 dB/mm) and (4.59 dB/mm to 6.51 dB/mm) for the old and new processes respectively. While the average value of the devices fabricated using the new process is lower than that of those fabricated with the old process, the values were found to not be statistically different. This is due to the higher degree of variability of the devices made using the procedure outlined in this thesis. A more detailed characterization of the devices is required still to be able to indeed conclude that

the two procedures produce device of indiscernible quality. This will require testing of features other than just straight waveguides, such as MZI's and coupler waveguides.

Further testing is required in order to characterize the MZI's as well as a detailed comparison of the biosensing capability of wafers manufactured under both sets of processing conditions. It is expected that the new fabrication procedure will produce more evenly split power modes in the MZI structures and as such yield more consistent and reproducible results, as of yet, MZI's fabricated under the old procedure have not been able to be tested.

Further efforts to increase the depth of the fluidic channels as well as encapsulate the devices are also under way. This will allow for simpler setups when performing optical characterization and biosensing experiments, as well as allowing for detection of larger analytes and reduction of the pressure drop through the channels.

In addition to device testing and the bonding work, publications are also underway: the first being a proceedings paper for research presented during the Photonics North conference held in Montreal, QC, Canada in June of 2012 entitled "*Fabrication of surface plasmon waveguides in CYTOP*". This will focus on the modified fabrication procedure described in this thesis up to, but not including, the encapsulation process. A second publication is also underway, aimed at a more reputable fabrication based journal, the title of the article is still to be determined; however, the focus will be on the incorporation of a viable encapsulation process which will allow for successful sealing of the fluidic channels.

7. References

1. Rogers, K. R. "*Recent advances in biosensor techniques for environmental monitoring"*, Analytica Chimica Acta, Vol. 568, 222 - 231. (2006)
2. Ruan, C., Zeng, K., Verghese, O. K., Grimes, C. A. "*A magnetoelastic bioaffinity-based sensor for avidin*", Biosensors and Bioelectronics, Vol. 19, 1695 - 1701. (2004)
3. Zhang, X., Ju, H., Wang, J. "*Electrochemical sensors, biosensors and their biomedical applications*", Elsevier. (2008)
4. Anjanappa, M., Datta, K., Song, T. "*The mechatronics handbook*", CRC Press. (2002)
5. Kasten, F. H., "*Fluorescent and Luminescent prodes for biological activity 2nd Ed.*", Elsevier. (1999)
6. Chiu, C. "*Fabrication of surface plasmon waveguide devices in CYTOP with microfluidic channels*", M.A.Sc. Thesis, University of Ottawa. (2009)
7. Krupin, O. "*Biosensing using long-range-surface-plasmon-polariton (LRSPP) waveguides*", Ph.D. Thesis Proposal, University of Ottawa. (2011)
8. Love, J. C., Estroff, L. A., Kriebel, J. K., Nuzzo, R. G., Whitesides, G. M. "*Self-assembled monolayers of thiolates on metals as a form of nanotechnology*", Chemical Reviews, Vol. 4 (105), 1103 - 1169. (2005)
9. Maier, S. A. "*Plasmonics: fundamentals and applications*", Springer. (2007)
10. Chiu, C., Lisicka-Skrzek, E., Tait, R. N., Berini, P. "*Fabrication of surface plasmon waveguides and devices in CYTOP with integrated microfluidic channels*", Journal of Vacuum Science and Technology B, Vol. 28 (4), 729 - 735. (2010)

11. Haniff, R. "*Microfabrication of plasmonic biosensors in CYTOP integrating a thin SiO_2 diffusion and etch-barrier*", M.A.Sc. Thesis, University of Ottawa. (2011)
12. Geddes, C. D. "*Reviews in plasmonics*", Springer. (2010)
13. Herminjard, S., Sirigu, L., Herzig, H. P., Studemann, E. "*Surface plasmon resonance sensor showing enhanced sensitivity for CO_2 detection in the mid0infrared range*", Optics Express, Vol. 17, 293 - 303. (2009)
14. Berini, P., Charbonneau, R., Lahoud, N., Mattiussi, G. "*Characterization of long-range surface plasmon polariton waveguides*", Journal of Applied Physics, Vol. 98 (1), 043109, 1 - 12. (2005)
15. Berini, P. "*Bulk and surface sensitivities of surface plasmon waveguides*", New Journal of Physics, Vol. 10, 1 - 37. (2008)
16. "*Amorphous Fluoropolymer CYTOP: Tehcnical Data*", Asahi Glass Company, http://www.agc.cp.jp
17. "*PMGI SF series resists material safety data sheet*", Microchem Corporation, http://www.first.ethz.ch/infrastructure/Chemicals/Ebeam_lithography/MSDS_PMGI SF8.pdf
18. Jones, S. W. "*Photolithography*", IC Knowledge LLC. (2008)
19. "*Metallization*", Carleton University, http://www.doe.carleton.ca/facilities/fab/metal.php

20. "*Nano PMGI Resists*", Microchem Corporation, http://www.first.ethz.ch/infrastructure/Chemicals/Ebeam_lithography/Data_PMGI.pdf

21. "*PMGI and LOR Resists: FAQ's*", Microchem Corporation, http://www.microchem.com/pmgi-lor_faq.htm

22. Krupin, O., Asiri, H., Wang, C., Tait, R. N., Berinin, P. "*Biosensing using straight long-range surface plasmon waveguides"*, Optics Express, (Submitted)

23. Beringer, J., Napoli, A., Graf, M., Textor, M., Hubbel, J. "*PPS-PEG block copolymers render hydrophobic surfaces protein and cell resistant*", European Cells and Materials (Suppl. 1), Vol. 2, 45, (2001)

24. Daviau, R., Khan, A., Lisicka-Skrzek, E., Tait, R. N., Berini, P. "*Fabrication of surface plasmon waveguides and integrated components on CYTOP*", Microelectronics Engineering, Vol. 87, 1914 - 1921. (2010)

25. "*Surface plasmons*", Optrel GBR, http://www.optrel.de/pdfs/flyer/spr-prinzip.pdf

26. Albella, P., Saiz, J. M., Gonzalez, F., Moreno, F. "*Surface monitoring based on light scattering by metal nanosensors*", Journal of Quantitative Spectroscopy and Radiative Transfer, Vol. 112, 2046 - 2058. (2011)

27. Axelrod, D., Koppel, D. E., Schlessinger, J., Elson, E., Webb, W. W. "*Mobility measurement by analysis of flourescence photobleaching recovery kinetics*" Biophysical Journal, Vol. 16, 1055 – 1069. (1976)

28. "*LOR and PMGI resists*", Microchem Corporation, http://www.microchem.com/pdf/PMGI-Resists-data-sheetV-rhcedit-102206.pdf

29. "*How does surface plasmon resonance work?*", Bionavis Oy Ltd., www.bionavis.com/technology/spr/#kretschmann

30. "*Megaposit SPR 220 series photoresist for i-line applications*", Rohm and Haas Electronic Materials, http://ncnc.engineering.ucdavis.edu/pages/equipment/SPR220_Data_Sheet.pdf

31. Umbrecht, F., Muller, D., Gattiker, F., Boutry, C. M., Neuenshwander, J., Sennhauser, U., Hierold, C. "*Solvent assisted bonding of polymethylmethacrylate: characterization using response surface methodology"* Sensors and Actuators A: Physical, Vol. 156, 121 – 128, (2009)

32. Tsao, C. W., Hromada, L., Liu, J., Kumar, P., DeVoe, D. L. "*Low temperature bonding of PMMA and COC microfluidic substrates using UV/ozone surface treatment"* Lab on a Chip, Vol. 7, 499 – 505, (2007)

33. Kwei, T. K., Zupko, H. M. "*Diffusion in glassy polymers. I"* Journal of Polymer Science: Part A-2, Vol. 7, 867 – 877, (1969)

34. Vesely, D. "*Diffusion of liquids in polymers"* International Materials Reviews, Vol. 53, 299 – 315, (2008)

35. Frisch, H. L., Wang, T. T., Kwei, T. K. "*Diffusion in glassy polymers: II"* Journal of Polymer Science: Part A-2, Vol. 7, 879 – 887, (1969)

36. Collins, R. "*Mathematical modelling of controlled release from implanted drug-impregnated monoliths"* Pharmaceutical Science and Technology Today, Vol. 1, 269 – 276, (1998)

37. "Nano SU-8 Negative Tone Photoresist Formulations 2 -25", Microchem Corporation, http://www.microchem.com/pdf/SU8_2-25.pdf

38. Tuomikoski, S., Fransilla, S., "*Free-standing SU-8 microfluidic chips by adhesive bonding and release etching*", Sensors and Actuators A, Vol. 120, 408 - 415. (2005)

Appendix A - Table of Wafers Processed

Wafer ID	Lower Cladding Thickness	Device Lithography	Gold Thickness	Gold Recipe	Upper Cladding Thickness	Channel Lithography	Etch Time	Over-etch Depth	Attenuation	Figure Reference
CT-Au-1	9 µm	HMDS + LOR-1A + S1805	34 nm	Spits	8 µm	SPR 220-7 + 2 hrs rehydration	8.5 min	230 nm	6.8 dB/mm	Figure 24 a), Figure 26 a), Figure 39 a), c) & e)
CT-Au-2	9 µm	HMDS + LOR-1A + S1805	34 nm	Spits	8 µm	SPR 220-7 + 24 hrs rehydration	9 min	400 nm	6.4 dB/mm	Figure 33, Figure 35 a), Figure 55
ND-I	9 µm	HMDS + PMGI SF 2G + S1805	34 nm	No Spits	8 µm	SPR 220-7 + 24 hrs rehydration	8.5 min	330 nm	5.4 dB/mm	Figure 21, Figure 26 b), Figure 46 a) & b), Figure 49 a), Figure 52, Figure 54
ND-II	9 µm	HMDS + PMGI SF 2G + S1805	34 nm	No Spits	8 µm	SPR 220-7 + 24 hrs rehydration	8.5 min	370 nm	--	Figure 25 b)
F1	9 µm	HMDS + PMGI SF 2G + S1805	20 nm	No Spits	6.7 µm	SPR 220-7 + 24 hrs rehydration	7 min	180 nm	7.7 dB/mm	Figure 30 a) & b)
F2	9 µm	HMDS + PMGI SF 2G + S1805	20 nm	No Spits	6.7 µm	SPR 220-7 + 2hrs rehydration	7.5 min	260 nm	--	--
F3	9 µm	HMDS + LOR-1A + S1805	34 nm	Spits	8 µm	SPR 220-7 + 2hrs rehydration	9.5 min	600 nm	6.8 dB/mm	--
F4	9 µm	HMDS + LOR-1A + S1805	34 nm	Spits	20 µm	SPR 220-7 + 2hrs rehydration	--	--	--	--
F3-B	9 µm	HMDS + PMGI SF 2G + S1805	34 nm	No Spits	8 µm	SPR 220-7 + 24 hrs rehydration	8.5 min	150 nm	--	Figure 24 b), Figure 40, Figure 42 a) & b), Figure 47, Figure 51
F4-B	9 µm	HMDS + PMGI SF 2G + S1805	34 nm	No Spits	20 µm	SPR 220-7 + 24 hrs rehydration	--	--	--	Figure 35 b), Figure 39 b), d) & f)

Appendix B - Wafer Bonding Processes

SU-8 Bonding by Thermal Fusion

Two variations of this process were attempted, both resulting in insufficient contact between the device wafer and the glass lid wafer as well as plugging of the fluidic channels. The first method involved the use of SU-8 as an adhesive layer to bond between the etched device wafer and the glass wafer. A 5 µm thick film of SU-8 was spun onto a clean glass wafer and baked at 70 °C for 30 minutes. The etched device wafer is simultaneously heated to the same temperature and pressed onto the SU-8 surface, applying pressure from one edge of the wafer and working across to the other. The wafers are allowed to rest on the hotplate at 70 °C, without pressure, for 2 hours after the bond is initiated to allow the SU-8 film to conform to the CYTOP surface. After bonding is complete, the SU-8 film is exposed to UV light through the glass wafer to initiate cross-linking within the layer.

This method is an adaptation of one described in [38], in which SU-8 is bonded to SU-8 to form large fluidic channels. The authors had reported that channel plugging was an issue for channels with depths below 100 µm due to high capillary action. Their solution was to include sacrificial channels to help with overflow of SU-8 during the bonding process and reduce filling of device channels. With the incorporation of sacrificial channels, there was still substantial filling of channels less than 100 µm in depth. The depth of the channels etched into the devices described in this thesis are limited to only 8 µm and as such were completely filled with SU-8 when attempting to bond. Furthermore, there were large areas of the wafer where no bond was initiated at all, forming voids, due to the limited thickness

of the adhesion layer as well as surface variations present on both the SU-8 and CYTOP. It is possible to increase the thickness of the adhesion layer; however, this would only result in further plugging of the fluidic channels and was not investigated further.

The second method involves spin coating SU-8 over the device wafer before channel definition and performing a flood exposure to fully cross-link the layer. Following the SU-8 application, a thin layer of aluminum is deposited on top of the SU-8 to act as a hard mask during etching of the fluidic channels. Aluminum is chosen because it is cheap, abundant and can be selectively removed by MF 321 developer solution. Aluminum deposition is performed in a similar manner to the gold deposition procedure described in section 0, except the thickness is set to 100 nm and the maximum e-beam power is set to 35% giving a deposition rate of ~5 Å/s. A 100 nm thick aluminum film is opaque making channel alignment to the devices impossible. For this reason two thin strips of tape are placed at the top and bottom of the wafer prior to aluminum deposition. Once the wafer is removed from the evaporator chamber, the tape is removed, exposing alignment marks for channel definition. S1805 photoresist is then spun onto the aluminum in the same manner explained in the same manner described in Table 5 and exposed using the fluidic channel mask for 7 seconds in the Karl Suss MA6 mask aligner. Following exposure, the wafer is immersed in MF 321 for 4 minutes with medium agitation; this selectively removes the exposed portions of the S1805 and, with it, the aluminum underneath. The wafer is then etched in O_2 plasma; the portions still covered in aluminum remain unaffected while the developed regions are opened up, eventually making their way down to the device level,

exposing the gold surface. The remaining aluminum is then stripped away by immersion in MF 321 leaving the upper SU-8 surface in its original condition. The SU-8 layer increases the channel depth by as much as 20 μm. However, when bonding with a glass wafer coated with a thin film of SU-8 is attempted, similar issues occured as with the previously described method: large void areas were plainly visible and plugging of channels was still observed in areas where a bond was initiated. Furthermore, SU-8 has a very high surface roughness after being etched in O_2 plasma (as much as 300 nm) and it was found that this etch profile transferred through to the CYTOP due to the anisotropic nature of the March Systems Jupiter II etcher.

Appendix C: CYTOP/CTSOLV 180 Diffusion Characterization

Due to the large impact of diffusion of CTSOLV 180 into CYTOP on the quality of the waveguides during spin coating of the upper cladding, diffusion characterization was performed in an attempt to better understand the phenomena and manipulate the processing conditions to improve device quality. The testing consisted of pouring a small amount of CYTOP (CTX-809SP2) onto a glass wafer and measuring the change in weight as a function of time at various baking temperatures (50 °C, 75 °C and 100 °C).

The data was plotted as M_i/M_∞ versus time, where M_i is the mass of the sample at some time ***i*** and M_∞ is the mass of the sample if the test were to run for an infinite period of time (effectively the mass of solids in the sample after all the solvent has diffused out) [33]. The data was then analysed to determine the type of diffusion (Fickian, Case II or anomalous) [34]. In Fickian diffusion M_i/M_∞ is directly proportional to the square root of time ($\boldsymbol{t^{0.5}}$), in Case II diffusion M_i/M_∞ is directly proportional to time ($\boldsymbol{t}$) and anomalous diffusion is considered to be a combination of the two ($\boldsymbol{t^{0.5>x>1}}$). In order to determine the type of diffusion occurring for CTSOLV 180 in CYTOP, M_i/M_∞ was plotted against time using various exponents ranging from 0.5 to 1 in increments of 0.1 (following Equation (1)). Figure A1 shows linear trend lines fitted to mass data obtained from diffusion testing at 50 °C, it can be clearly seen that the linear plot is best suited to $\mathbf{M_i/M_\infty = k\, t^{0.5}}$, where k was found to be 0.0035.

$$\textbf{(1)}\ \frac{\mathbf{M_i}}{\mathbf{M_\infty}} = \mathbf{k \cdot\ t^n}\ ,\ \ \mathbf{0.5 \leq n\ \leq\ 1}\ \text{[35]}$$

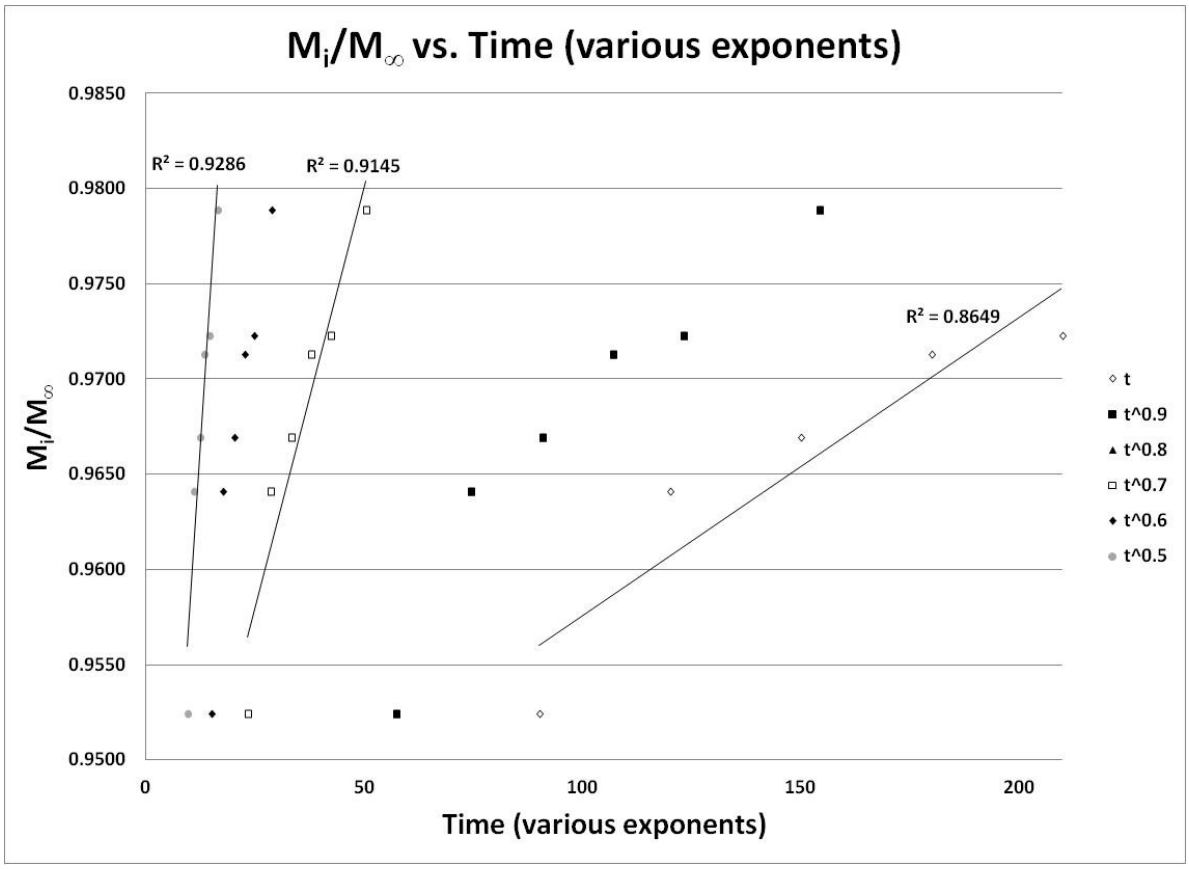

Figure A 1: Linear trend lines fitted to mass data versus time to various exponents indicating best fit for M_i/M_∞ vs. $t^{0.5}$ or Fickian diffusion.

It should be noted that Fickian diffusion was only observed for samples tested at 50 °C and 75 °C. For the sample tested at 100 °C, a large deviation from linear behaviour in the plot was observed, shown in Figure A2 below.

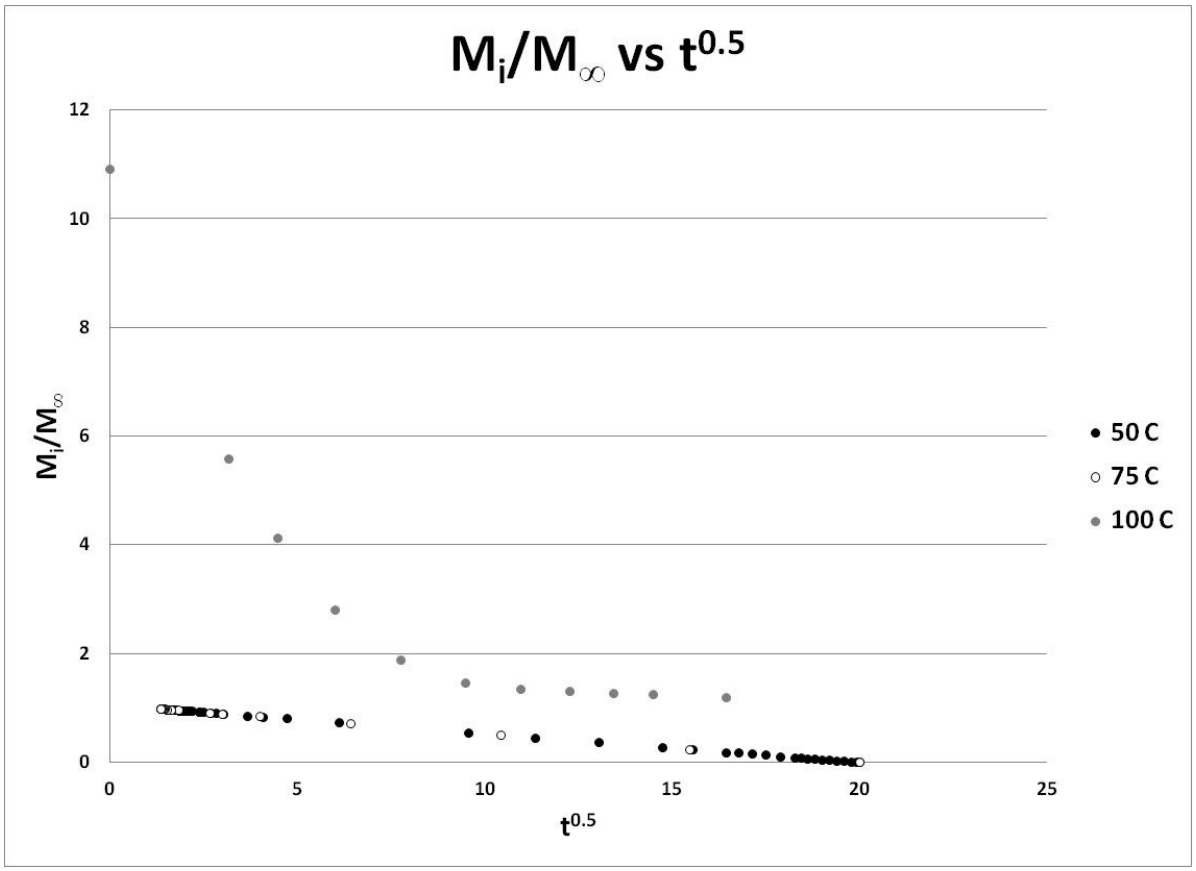

Figure A 2: M_i/M_∞ vs. $t^{0.5}$ at various temperatures, showing deviation from Fickian behaviour at 100 °C.

When attempting to fit the mass data for the test performed at 100 °C to an exponent that would be indicative of either anomalous or Case II diffusion, the deviation from linearity was only amplified. This would indicate that some other, unexplained phenomena is occurring to obscure the diffusion profile, complicating the determination of the exact mechanism of diffusion. Further testing and more detailed analysis of this phenomenon would be required in order to verify the above findings. The diffusion coefficients listed below for the sample tested at 100 °C assume the validity of Fickian

diffusion although they are subject to uncertainty due to the deviation from the expected mass profile behaviour.

For Fickian diffusion, the primary equation of interest is:

$$(2)\ \mathbf{D} = \left[\frac{\mathbf{k} \cdot \mathbf{L}}{\mathbf{2}}\right]^{\mathbf{2}} \cdot \boldsymbol{\pi} \quad [34]$$

Where,
D = Diffusion coefficient (cm^2/s)
k = Slope of the curve following (M_i/M_∞ vs. $t^{0.5}$)
L = Characteristic length of diffusion (thickness of CYTOP film in this case)

Table A1 below indicates diffusion coefficients of CTSOLV – 180 through CYTOP as a rubbery solid as well as those determined for CYTOP as a glassy solid. This was done by separating the diffusion curve into three sections: (1) the viscous liquid stage, typically lasted less than a few minutes at 50 °C, decreasing in duration with increasing temperature. (2) the rubbery solid stage, lasting anywhere from 30 minutes at 100 °C to as much as 3 hours at 50 °C. (3) glassy solid, final stage of diffusion, beyond this region change in mass was very small over large periods of time due to minimal void volume between polymer chains. Solvent mobility is greatly hindered and for all practical purposes, solvent removal rate is effectively zero.

Table A 1: Diffusion coefficient summary table for rubbery and glassy solids at various temperatures.

Temperature (°C)	50	75	100
	Diffusion Coefficient (cm^2/s)		
Rubbery Solid	2.45×10^{-16}	4.40×10^{-16}	6.11×10^{-13}
Glassy Solid	8.32×10^{-18}	6.06×10^{-17}	3.69×10^{-15}

It should be noted that the diffusion rates for the viscous liquid stage were not reported due to the inability for accurate measurement and determination of convective diffusion rates as well as the very short time that CYTOP spends as a viscous liquid, even at low temperatures. Figure A3, shown below, illustrates the mass of a sample as a function of time throughout the baking procedure for temperatures of 50 °C and 100 °C. As can be seen, there is a substantially rapid decrease in mass very early in the baking process (more pronounced in 100 °C sample), indicating the short period of time the sample spends in the liquid phase. The curve in the profile indicates the rubbery solid region, which for practical application is the phase that will be of most interest when applying the upper CYTOP cladding. As the profile levels off, the sample becomes glassy and any change in mass is minimal, requiring long baking periods to achieve minimal amounts of solvent removal.

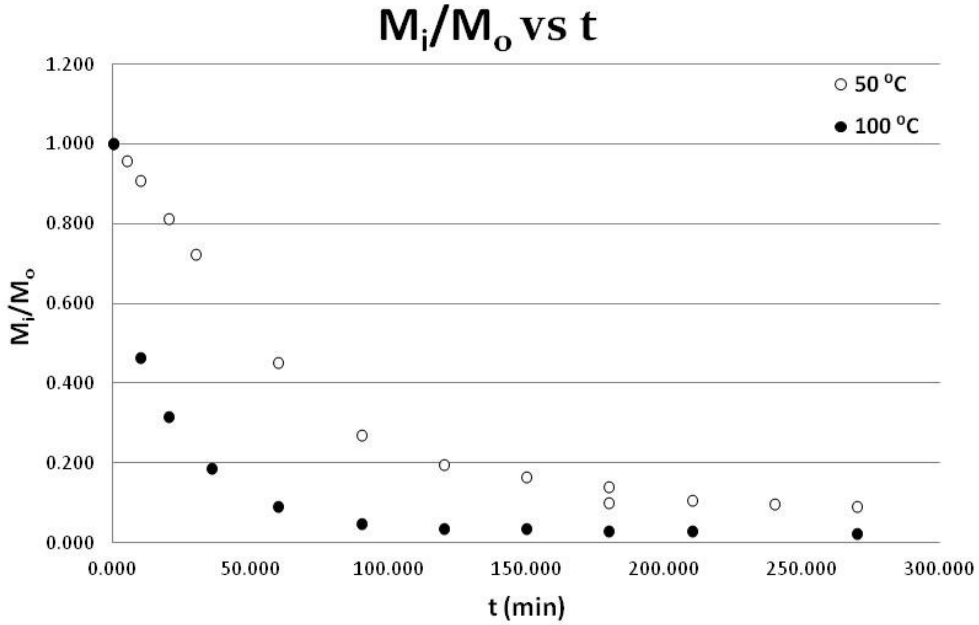

Figure A 3: Mass profiles of baked samples as a function of time. M_i is mass of sample at time *i*, M_o is mass of sample at time *t=0*.

Finally it should be noted that a majority of solvent ingression will occur when the sample is in the liquid phase. Since CYTOP must be baked at a relatively low temperature initially to avoid bubbling and surface damage due to rapid solvent escape, it will likely be impossible to completely eliminate device deformation during the upper cladding deposition process, however, by minimizing the amount of solvent in the upper cladding layer closest to the devices, and subsequent layers thereafter, the CYTOP can be maintained as a glassy solid thus minimizing the amount of deformation occurring.

As of yet, the optimal conditions appear to be those described in Chapter 4, in which each upper cladding layer is baked at 100 °C to drive off a maximum amount of solvent and shift the CYTOP into the glassy state. Then by depositing the subsequent layer and baking at

50 °C, it is possible to exploit the best of both tested properties; the reduced diffusion coefficient due to its dependence on temperature, as well as the reduced diffusion coefficient due to its dependence on the state of the material it is diffusing through.